2007

Optimal recovery of regional CO2 surface fluxes by data assimilation of anthropogenic and biogenic tracers

Elliott Campbell
University of Iowa

OPTIMAL RECOVERY OF REGIONAL CO_2 SURFACE FLUXES BY DATA ASSIMILATION OF ANTHROPOGENIC AND BIOGENIC TRACERS

by

Elliott Campbell

An Abstract

Of a thesis submitted in partial fulfillment of the
requirements for the Doctor of Philosophy degree
in Civil and Environmental Engineering in
the Graduate College of
The University of Iowa

May 2007

Thesis Supervisors: Professor Jerald Schnoor
Assistant Professor Charles Stanier

ABSTRACT

Measurements of atmospheric carbon dioxide (CO_2) have led to an understanding of the past and present CO_2 trends at global scales. However, many of the processes that underlie the CO_2 fluxes are highly uncertain, especially at smaller spatial scales in the terrestrial biosphere. Our abilities to forecast climate change and manage the carbon cycle are reliant on an understanding of these underlying processes. In this dissertation, new steps were taken to understand the biogenic and anthropogenic processes based on analysis with an atmospheric transport model and simultaneous measurements of CO_2 and other trace gases.

The biogenic processes were addressed by developing an approach for quantifying photosynthesis and respiration surface fluxes using observations of CO_2 and carbonyl sulfide (COS). There is currently no reliable method for separating the influence of these gross biosphere fluxes on atmospheric CO_2 concentrations. First, the plant sink for COS was quantified as a function of the CO_2 photosynthesis uptake using the STEM transport model and measurements of COS and CO_2 from the INTEX-NA campaign. Next, the STEM inversion model was modified for the simultaneous optimization of fluxes using COS and CO_2 measurements and using only CO_2 measurements. The CO_2-only inversion was found to be process blind, while the simultaneous COS/CO_2 inversion was found to provide a unique estimate of the respiration and photosynthesis component fluxes. Further validation should be pursued with independent observations. The approach presented here is the first application of COS measurements for inferring information about the carbon cycle.

Anthropogenic emissions were addressed by improving the estimate of the fossil fuel component of observed CO_2 by using observed carbon monoxide (CO). Recent applications of the CO approach were based on simple approximations of non-fossil fuel influences on the measured CO such as sources from oxidation of volatile organic carbon

species, sinks from oxidation of CO, and sources from forest fires. A revised CO method was developed using STEM simulations of atmospheric reactions and tracers of different combustion sources. Applications of the revised method to the NASA INTEX-NA measurements showed large differences with conventional methods. Application to the INTEX-B measurements resulted in partitioning of continental and offshore oil rig sources around Mexico.

Abstract Approved:

_____

Thesis Supervisor

_____

Title and Department

_____

Date

_____

Thesis Supervisor

_____

Title and Department

_____

Date

OPTIMAL RECOVERY OF REGIONAL CO_2 SURFACE FLUXES BY DATA ASSIMILATION OF ANTHROPOGENIC AND BIOGENIC TRACERS

by

Elliott Campbell

A thesis submitted in partial fulfillment of the
requirements for the Doctor of Philosophy degree
in Civil and Environmental Engineering in
the Graduate College of
The University of Iowa

May 2007

Thesis Supervisors: Professor Jerald Schnoor
Assistant Professor Charles Stanier

Graduate College
The University of Iowa
Iowa City, Iowa

CERTIFICATE OF APPROVAL

PH.D. THESIS

This is to certify that the PH. D. thesis of

Elliott Campbell

has been approved by the Examining Committee for the thesis requirement for the Doctor of Philosophy degree in Civil and Environmental Engineering at the May 2007 graduation.

Thesis Committee: _____

Jerald Schnoor, Thesis Supervisor

_____

Charles Stanier, Thesis Supervisor

_____

Gregory Carmichael

_____

Gene Parkin

_____

Stephanie Vay

ACKNOWLEDGMENTS

I am grateful for the abundance of ideas and perspective that I received from my co-advisors Dr. Jerry Schnoor and Dr. Charles Stanier. Their enthusiasm for my results and probing insight turned my studies into an exciting adventure through carbon cycle science. I could not have asked for better advisors.

I am very thankful to Dr. Gregory Carmichael for the many contributions that he provided throughout my studies, for bringing me into his atmospheric sciences community, and for serving on my committee. He was very generous with his expertise on atmospheric transport and data assimilation in many a fruitful discussion.

There were many people who shared modeling and measurement results that were essential to my studies. I thank Stephanie Vay for sharing her excellent CO_2 measurements and for serving on my committee. I thank Dr. Nicola Blake for the thoughtful discussions and for sharing the COS measurements from the University of California, Irvine. I am grateful for the observations of atmospheric trace gases from all the scientists who participated in the NASA INTEX campaigns and the NOAA/GMD observational network. I am thankful to Ian Baker (CSU) and Jim Collatz (NASA) for their land surface model results and Wouter Peters (NOAA/GMD) for his global transport model results.

I was very lucky to work with such an insightful group of faculty and students at the Department of Civil and Environmental Engineering and the Center for Global and Regional Environmental Research. I am thankful to Dr. Keri Hornbuckle and Dr. Gene Parkin for serving on my committee. I am very thankful to Dr. Youhua Tang for helping me set up my first transport model runs and the many hints he provided along the way. I am grateful to Dr. Tianfeng Chai for sharing his data assimilation models and answering my many questions about model modifications and data assimilation theory. I am very thankful for the great feedback and wonderful friendship from Marcelo Mena and Forrest

Meggers. It was fortune that brought the three of us together to work on environmental science and sustainability. I also am grateful for the interactions with all the other students and faculty at Iowa. I thank Judy Holland and Jane Frank for making sure everything ran smoothly.

I am in great debt to my family and friends for their inspiration and positive contributions throughout my studies. My parents have always been a source of wisdom and unconditional love and support. They are the cornerstone of my academic training. My sister was always there to ask the questions that really mattered and provide her unending support. My deepest thanks go to my wife, Liz. Her daily (sometimes hourly) encouragement made this dissertation possible.

This work was supported by grants from the Wisconsin Energy Center, the Center for Global and Regional Environmental Research, the National Science Foundation CLEANER program, NOAA Carbon Cycle Program, and the NASA Earth Science Graduate Fellowship program.

TABLE OF CONTENTS

LIST OF TABLES

LIST OF FIGURES

CHAPTER 1 INTRODUCTION

1.1 Background

Measurements of atmospheric carbon dioxide (CO_2) have led to an understanding of the past and present CO_2 trends at global scales. The current annual inputs from fossil fuel emissions are 7.3 PgC/yr [*Andres, et al.*, 1996; *Brenkert*, 1998] while the anthropogenic land use change contribution is 1.6 PgC/yr [*Houghton*, 1995]. The annual growth of atmospheric CO_2 varies from 0.5 to 3.5 ppm/yr indicating that the oceans and terrestrial biosphere remove approximately half of the anthropogenic CO_2 sources [*Conway, et al.*, 1994].

While the global carbon cycle trends are well known, many of the processes that underlie the CO_2 fluxes are highly uncertain, especially at smaller spatial scales in the terrestrial biosphere. Independent approaches for analyzing the terrestrial biosphere sinks in the northern hemisphere have not been able to converge on the same flux estimate [*Janssens, et al.*, 2003b; *Pacala, et al.*, 2001]. Estimates of the response of terrestrial vegetation and soil carbon pools to climate change remain poorly constrained by observations and models [*Friedlingstein, et al.*, 2003; *Fung, et al.*, 2005].

Uncertainty in the carbon cycle processes is an important problem because it limits our abilities to forecast climate change and manage the carbon cycle. The climate forecasting uncertainty due to carbon cycle forecasting uncertainty remains a large impediment to improved accuracy in climate projections [*Intergovernmental Panel on Climate Change*, 2001; *National Academy of Sciences*, 2001]. In particular, the rate at which the oceans and terrestrial biosphere will absorb anthropogenic CO_2 is not well constrained for a changing climate system.

The carbon cycle uncertainty at the regional scale is also important because it limits our abilities to design efficient and effective carbon management technologies and policies. The well known global trends are less applicable to designing solutions that can be applied at regional scales by governments and businesses. For example, conversion of agriculture to forest land is thought to increase carbon sequestration in the soils, but the limited understanding of soil processes at the regional scale results in a large uncertainty in estimates of soil carbon initiatives sequestration [*Heath, et al.*, 2002].

An ambitious research program called the North American Carbon Program (NACP) is designed to resolve these uncertainties through studies of the carbon cycle at a regional scale [*Denning, et al.*, 2005; *Sarmiento and Wofsy*, 1999; *Wofsy and Harris*, 2002]. North America provides an excellent domain for carbon studies because of the controversy over the spatial extent of the northern hemisphere terrestrial sink [*Fan, et al.*, 1998; *Gurney, et al.*, 2002; *Tans, et al.*, 1990], the large U.S. source of anthropogenic emissions [*Blasing, et al.*, 2005], and the expanding U.S. observation network [*Denning, et al.*, 2005]. The implementation strategy involves the synthesis of observations and models to refine the current knowledge of carbon cycle mechanisms and develop predictive capabilities that can be used to design efficient policy.

1.1.1 Top Down and Bottom Up Approaches

At the heart of the NACP implementation strategy is a feedback between observations, model-data synthesis, and prognostic models. A variety of observations are made from surface, aircraft, and satellite platforms. The observations are synthesized with diagnostic models in order to validate and refine the understanding of the processes controlling the carbon cycle. The process information is then used in prognostic models to forecast the carbon cycle under different climate change and carbon management scenarios.

One approach to the model-data synthesis step is to apply atmospheric assimilation models that take atmospheric CO_2 concentrations as input and output surface fluxes (top down approach or inversion). Independent estimates of surface fluxes are estimated with the surface flux models that are based on mechanisms such as photosynthesis and respiration (bottom up approach). The differences in the independently derived surface fluxes are analyzed in order to refine our understanding of the surface flux mechanisms and improve the diagnostic models. An improved understanding of the mechanisms is essential to developing the forecast model because carbon-climate feedback mechanisms make simple extrapolation inaccurate.

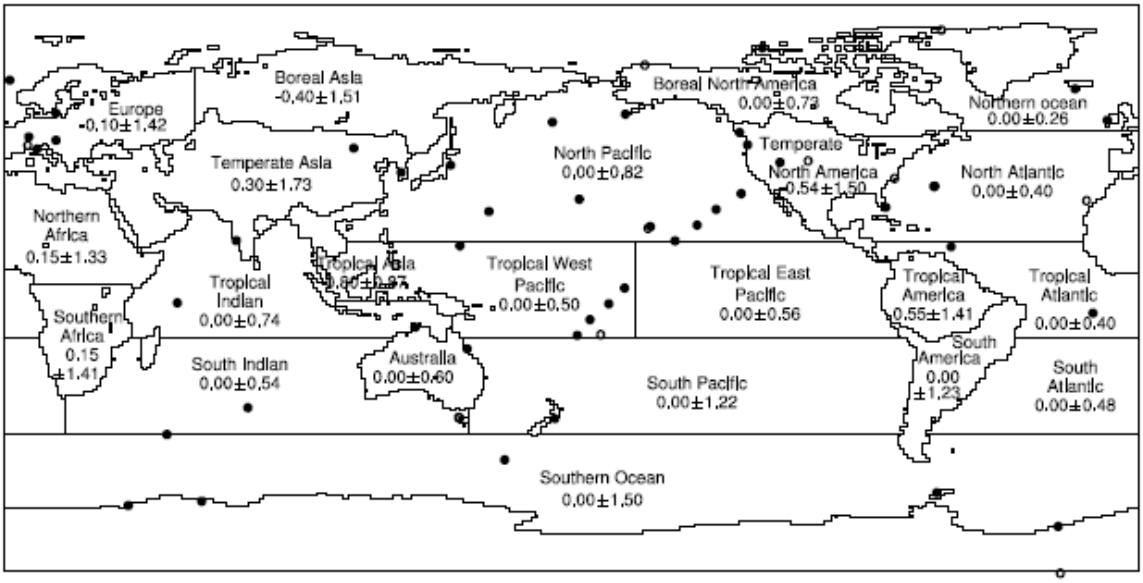

Source: Gurney, K. R., et al. (2002), Towards robust regional estimates of CO_2 sources and sinks using atmospheric transport models, Nature, 415, 626-630.

Figure 1. Top down CO_2 flux regions with first guess (prior) of flux mean and uncertainty (Gt C/yr) and dots indicating the 76 surface observation locations.

The top down/bottom up strategy has been used at global and continental scales to determine mechanisms of the carbon cycle, in particular, a northern hemisphere terrestrial

carbon sink [*Janssens, et al.*, 2003a; *Pacala, et al.*, 2001]. The top down fluxes from atmospheric assimilation typically use observations from a global network of CO_2 observatories [*GLOBALVIEW-CO2*, 2005]. Top down flux regions are often aggregates of the forward model flux grid cells as shown in Figure 1. The bottom up fluxes are obtained by analyzing inventories of carbon in forests, croplands, grasslands, reservoirs, rivers, wood products, anthropogenic carbon emissions, and commerce.

These two independent fluxes are contrasted in order to develop hypotheses of missing mechanisms and errors in each approach. The top down studies have consistently indicates a larger northern hemisphere sink than the bottom up method. For example, an iterative approach between bottom up and top down methods was used to investigate this "missing sink" for Europe resulting in top-down sink estimates of 205 TgC/yr and bottom-up estimates of 135 TgC/yr. Given this strong evidence at the continental level for a net terrestrial sink, the goal of the North American Carbon Plan is to focus on determining the regional mechanisms that drive surface fluxes responsible for this sink.

1.1.2 Top Down Approach

Formulations of atmospheric assimilation models have been well documented [*Enting*, 2002; *Rodgers*, 2000] but rapid theoretical expansion has led to an abundance of approaches. Most techniques are based on the simple notion that the optimal surface flux minimizes the square of the differences between model concentrations and observed concentrations, where these squared differences are weighted by the error covariances at the different observation points. This cost function for retrieving optimal surface fluxes is,

$$J = (o - M(f))^T A^{-1} (o - M(f)) \qquad 1$$

where o is the vector of concentration observations, f is the state variable vector of surface fluxes, M is the forward atmospheric transport model, and A is the error

covariance matrix that accounts for the relative precisions of the different errors in space and time. By weighting the model-observation differences by the inverse of the uncertainties, A^{-1}, observation points with lower error are given more consideration than observation points with higher error.

The optimal solution of J (equation 1) is complicated by the fact that the forward atmospheric model M is computationally expensive and the state vector f is related to the data by implicit functions. The computational costs of the atmospheric model M makes a Monte Carlo solution method time prohibitive. An alternative approach is the gradient method in which optimization would involve first deriving the partial derivatives of the cost function with respect to the state variables. The optimal solution of the state vector is solved for by setting the partial derivatives equal to zero. The fact that the transport model (optimization constraints) is an implicit function of the fluxes (state variables) makes the partial derivatives difficult to calculate. The partial derivatives could only be determined after repeated applications of the chain rule.

Two families of methods have been developed to solve the optimization problem: sequential and variational. Sequential approaches apply the Kalman filter technique to determine the optimal flux and variance of the optimal flux at a given time. Variational approaches (e.g. 4D-Var) use Lagrange multipliers to simplify the process of solving for the partial derivatives of the cost function. The variational methods can determine optimal fluxes and sensitivities of model outputs with respect to inputs. While sequential and variational methods obtain the same flux given the same input they differ in computational cost, code development complexity, and ancillary outputs.

The sequential approach has been applied extensively in CO_2 assimilation [*Enting*, 2002]. The variational method has been successfully applied in CO_2 atmospheric tracer-transport [*Chevallier, et al.*, 2005; *Engelen and McNally*, 2005; *Kaminski, et al.*, 1999] and has recently been developed for reactive chemistry with the STEM atmospheric transport model [*Carmichael, et al.*, 2003a].

The optimization problem (equation 1) is typically ill conditioned because the atmospheric observations are sparse relative to the number of flux state variables. For example, a regional assimilation over North America with a 60 km flux grid resolution would have thousands of state variables but only a few surface observations. Ill conditioning is also a problem when the observations are at points that are not well connected by atmospheric transport to the surface fluxes. For example, most of the CO_2 observations in the U.S. are in the upper Midwest and northeast. These concentrations are not sensitive to the surface fluxes in other regions of North America.

To address the ill conditioned problem, past studies have added pseudo data to the cost function or reduced the number of state variables by aggregating the flux grid cells. In the future this problem may be addressed by increased availability of CO_2 observations from high resolution satellite data [*Houweling, et al.*, 2004]. Past studies have typically addressed this issue by adding terms to the cost function (pseudo data) that require that the optimal fluxes be similar to the prior fluxes (initial estimate of fluxes) [*Gurney, et al.*, 2002]. Limitations to this approach are that it adds a bias in the optimized flux estimate and that prior uncertainties are difficult to determine [*Bousquet, et al.*, 1999]. An alternative cost term is a geostatistical penalty that forces neighboring grid cells to be more similar than grid cells that are more distant from each other [*Michalak, et al.*, 2004]. Another approach to the underdetermined problem is to reduce the number of state variables by aggregating the flux grid cells into several large regions. Aggregating grid cells would not be appropriate for regional applications over North America due to the large spatial variability of terrestrial surface fluxes [*Gerbig, et al.*, 2006].

1.2 Overview and Objectives

The purpose of this research proposal is to increase scientific understanding of patterns and mechanisms of CO_2 surface fluxes. The main approach is by developing methods for obtaining information about biogenic and anthropogenic processes using observations of trace gas species that are influenced by these processes. A novel approach for quantifying photosynthesis and respiration is developed using measurements of carbonyl sulfide (COS), CO_2, and the STEM transport and inversion models. The COS method development is addressed in Chapters 2 and 3. The approach for quantifying fossil fuel CO_2 sources with CO measurements is revised using the STEM reactive transport model and additional tracers of combustion processes. The CO method development is addressed in Chapters 4 and 5. The results presented in Chapter 4 have been accepted for publication [*Campbell, et al.*, 2007]. Manuscripts are under preparation for the results from Chapters 2, 3, and 5. Preliminary results from Chapter 3 are in a manuscript under review [*Blake, et al.*, Submitted].

The STEM atmospheric transport model and the STEM inversion model are applied for both the COS and CO tracer developments. The STEM forward model has been validated for regional applications in the INTEX-NA (Intercontinental Chemical Transport Experiment –North America) TRACE-P (Transport and Chemical Evolution over the Pacific (TRACE-P) experiment [*Carmichael, et al.*, 2003b; *Carmichael, et al.*, 2003c; *Tang, et al.*, In Press]. The model employs the SAPRC99 chemical mechanism [*Carter*, 2000], the SCAPE II aerosol thermodynamics module, and an on-line photolysis solver [*Tang, et al.*, 2003].

The STEM inversion model has been developed using the four dimensional variational (4D-Var) approach for optimal estimates of model input and model parameters [*Carmichael, et al.*, 2003a; *Daescu and Carmichael*, 2003; *Sandu, et al.*,

2005]. This model has been for sensitivity studies and optimal estimation of model parameters such as emissions and initial conditions [*Chai, et al.*, 2006b; *Hakami, et al.*, 2005; *Hakami, et al.*, 2006; *Sandu*, 2006].

Atmospheric trace gas measurements made from the NASA DC8 aircraft were used in both tracer applications. The INTEX-NA experiment was over the eastern U.S. and Canada during the summer of 2004 while the INTEX-B experiment was over Mexico and the Gulf of Mexico during the spring of 2006. These experiments provide unprecedented atmospheric chemistry information for simultaneous measurements of many atmospheric species over a wide spatial extent. Observations included CO_2 (± 0.25 ppmv), CO (± 2 %), COS (± 10 pptv) and many other gases and aerosols.

1.2.1 Background Tracer Application 1: COS Biosphere Tracer

A promising approach for adding constraints to the optimization problem is to introduce information about atmospheric species that are related to CO_2. These species may be tracers of surface fluxes that influence CO_2 such as carbon monoxide (CO) from anthropogenic combustion and ratios of stable isotopes for ocean and biosphere fluxes. Recent work has applied this approach for CO_2 assimilation by extracting information from observation-model error covariances between CO_2 and CO [*Palmer, et al.*, In review]. The data from the TRACE-P campaign over the NW Pacific in March, 2001 is sensitive to surface fluxes in East Asia [*Carmichael, et al.*, 2003c]. The model-observation correlation of CO_2 and CO was strong because the growing season had not started and anthropogenic sources that co-emit CO and CO_2 were the dominant influence on the variation of the mixing ratios. This study found that the CO:CO_2 correlations applied in the assimilation led to improved optimal fluxes for CO_2 and helped to distinguish the biogenic from anthropogenic CO_2 signals. There was less benefit to retrieving optimal CO fluxes, except in regions associated with large transport errors.

For assimilation studies focused on determining the optimal biosphere sink, the simultaneous assimilation approach will require a biogenic tracer rather than the CO anthropogenic tracer. During the growing season, the CO:CO_2 correlation will be low because the variability of CO_2 mixing ratios is driven by the variability of the biosphere flux instead of the anthropogenic flux. An appropriate approach for the growing season would be to exploit the information contained in mixing ratio observations of a biogenic tracer. A novel tracer of the biosphere is carbonyl sulfide (COS or OCS) which is taken up by plants along with CO_2 because of its chemical and structural similarity. Recently, high correlations between CO_2 and COS were observed over North America during the growing season [*Blake, et al.*, Submitted; *Montzka, et al.*, In Press], indicating that simultaneous assimilation of COS and CO_2 could be advantageous.

The COS observations can also be used to partition the influences of respiration and photosynthesis. The current inversion studies are under-constrained for optimizing the net surface flux. Thus, they are even more under-constrained for optimizing the separate photosynthesis and respiration surface fluxes (twice as many control variables as with the net flux inversion). The COS observation is a constraint that is specific to the photosynthesis surface flux and should be an ideal tracer for deconvolving the photosynthesis and respiration influences.

Surface fluxes of COS include the anthropogenic combustion sources, oxidation sinks, oxidation of reduced sulfur species (DMS, CS_2) sources, ocean source/sinks, photolysis sinks, and terrestrial biosphere sinks [*Watts*, 2000]. The average tropospheric concentration is 0.5 pptv and the tropospheric lifetime is 2 to 7 years. Because of this long lifetime, COS oxidation contributes to SO_2 and can contribute to stratospheric particles which effect the global radiative balance [*Crutzen*, 1976; *Engel and Schmidt*, 1994]. Laboratory and field studies of the correlations between COS and CO_2 have been used to develop global COS budgets [*Kettle, et al.*, 2002a; *Kettle, et al.*, 2002b; *Watts*,

2000]. However, observed correlations between COS and CO_2 have yet to be applied to constraining CO_2 surface fluxes.

1.2.2 Background Tracer Application 2: CO Combustion Tracer

A second emerging need for tracers in regional carbon data assimilation is to filter CO_2 observations. An important step in previous CO_2 assimilation studies is to filter anthropogenic combustion influences from the observed CO_2 signal. In most studies, this is done by using model estimates of the anthropogenic signal rather than tracer-based estimates. The model approach has the following steps: 1) drive the forward atmospheric model with bottom up anthropogenic CO_2 fluxes, 2) interpolate the model concentration results to the observation location, and 3) subtract this modeled anthropogenic concentration from the observed value. The filtered observation is then run through the data assimilation model to retrieve optimal fluxes.

This filtering of the observed data can also be achieved with regional tracers. Anthropogenic combustion tracers that are emitted at the same time and location as CO_2 can be used to estimate the anthropogenic component to the observed CO_2. For example, the concentration of CO can be multiplied by a ratio to estimate the component of anthropogenic CO_2.

The tracer approach to filtering has been proposed because the model inventory approach to filtering suffers from temporal and spatial resolution limitations. Model estimates of the fossil fuel component of CO_2 are obtained by simulating the transport of fossil fuel emission inventories with the transport model and interpolating to the observation location and time. The widely used fossil fuel emission inventories have an annual, 1° resolution [*Andres, et al.*, 1996; *Brenkert*, 1998]. Errors due to the coarse resolution can be expected for applications with a model domain resolution of 10^2 to 10^6 km^2 and sub-annual temporal resolution. Finer estimates of the fossil fuel contribution must be developed.

The North American Carbon Plan proposes use of observed anthropogenic tracers where observations of CO_2 and anthropogenic tracers such as CO are made simultaneously [*GLOBALVIEW-CO2*, 2005]. CO, which is widely measured at high time resolution and has been shown to yield better estimates of ${}^{ff}CO_2$ than the inventory method (simulating the transport of fossil fuel emission inventories) and the SF_6 tracer method [*Karstens, et al.*, 2005; *Turnbull, et al.*, 2006]. The CO approach has been applied as,

$$ {}^{ff}CO_2 = ({}^{obs}CO - {}^{obs\ bg}CO) / R \qquad (2) $$

Here ${}^{obs}CO$ is the observed CO concentration, ${}^{obs\ bg}CO$ is the concentration contribution from the background CO, and R is a ratio relating the adjusted CO value to ${}^{ff}CO_2$.

All CO tracer method studies have warned that sources of CO other than fossil fuel could lead to significant error in results but none of these studies have been able to quantify these potential errors. Recent work indicates the CO tracer technique overestimates fossil fuel CO_2 by 0.5 to 11 ppm due to unaccounted sources of CO such as biomass burning and in situ photochemical production [*Campbell, et al.*, In Preparation]. A revised CO method is needed to address these errors while still providing a workable framework for filtering CO_2 data.

1.2.3 Summary

In summary, tracers of CO_2 sources and sinks have the potential to address the emerging needs of regional scale carbon assimilation as described in the North American Carbon Plan. Observations of COS provide a novel biogenic tracer that has the potential to increase the level of determinism in the CO_2 assimilation problem. Observations of CO provide a tracer of anthropogenic combustion that can be used to filter CO_2 observations but such an approach needs error quantification and further development. The STEM regional chemical transport model and observations from field campaign provide ideal tools to develop these methods and evaluate tracer applications.

1.3 Specific Objectives

The specific objectives of this work are listed below, followed by a discussion of the details of each objective.

1. Quantify COS surface fluxes over North America.
2. Demonstrate simultaneous assimilation of CO_2 and COS.
3. Determine whether simultaneous assimilation leads to improved results over CO_2 only assimilation.
4. Determine errors in using CO as tracer of regional anthropogenic CO_2 related to non-anthropogenic sources/sinks of CO.
5. Develop revised CO tracer method.

The first objective marks the beginning of the development of COS as a novel tracer of biogenic CO_2 (Chapter 2). The best available bottom up fluxes of COS will be used in the regional scale STEM atmospheric model for comparison with aircraft observations. New estimates of the dominant COS surface fluxes from plant uptake will be developed. This will be the first such evaluation of these fluxes and of the regional atmospheric modeling framework for COS.

The second objective is to develop a simultaneous assimilation of CO_2 and COS observations for determining optimal surface fluxes (Chapter 3). Such a simultaneous approach to constraining the assimilation problem has only recently been attempted for CO_2 and CO and has yet to be applied directly for the benefit of determining the northern hemisphere terrestrial sink. This is because the multi-species approach is very new and also because no appropriate biogenic tracer for this approach has been successfully applied by the carbon cycle community. The observations of CO_2 and COS in the

INTEX-A data set have the potential to allow this biogenic tracer approach to constrain the biosphere fluxes over North America. The STEM adjoint is an ideal model for implementing variational assimilation with this data.

The third objective is to determine whether simultaneous assimilation leads to improved results over CO_2 only assimilation (Chapter 3). Both the CO_2-only and CO_2-COS assimilation approaches will be implemented with the STEM adjoint and INTEX-A data.

The fourth and fifth objective addresses the need to improve our understanding of anthropogenic influences on atmospheric CO_2 (Chapter 4). The fourth objective is to determine errors in the filtering approach in which CO is a tracer of regional anthropogenic CO_2. The full chemistry STEM model will be employed to account for the errors caused by non-anthropogenic sources of CO including forest fires and in situ photochemical production. The quantification of this error will be an important contribution to the carbon cycle community that plans on expanded use of the CO method for the emerging field of regional carbon modeling. The fifth objective is to apply the revised CO method that accounts for non-anthropogenic sources of CO to the measurements made during the NASA INTEX-A (Chapter 4) and INTEX-B field experiments (Chapter 5).

Although these dissertation chapters are focused on the top-down method, they are developments that would improve the interface for the top-down and bottom-up approaches. I have participated in bottom-up research to help in my understanding of the application. This research includes Wisconsin biomass and soil carbon calculation [*Campbell, et al.*, 2004], modeling approaches to soil carbon change [*Campbell, et al.*, In review], and the Red River Gorge field study. The soil modeling manuscript is included as Appendix A [*Campbell, et al.*, In review].

1.4 Summary of Contributions

The main contributions of this research are:

1. A top-down quantification of the COS plant uptake flux over North America.
2. A new approach for partitioning photosynthesis and respiration fluxes using an inversion model and measurements of CO_2 and COS.
3. The first application of COS measurements to infer information about the carbon cycle.
4. Estimate of the uncertainty in the CO method for estimating anthropogenic CO_2.
5. A revised CO method that accounts for mixed influences of fossil fuel combustion, forest fires, and reactive chemical processes.
6. Application of the revised CO method to emissions over the U.S. and Mexico.

CHAPTER 2 BIOSPHERE CARBON DIOXIDE TRACER MODEL WITH CARBONYL SULFIDE

2.1 Introduction

The dominant processes that govern the terrestrial biosphere flux at the Earth's surface are a gross sink from plant photosynthesis and a gross source from autotrophic (plants and algae) and heterotrophic (soil microorganisms) respiration. The photosynthesis sink, respiration source, and net flux can be referred to as gross primary productivity (GPP), total respiration (RES), and net ecosystem exchange (NEE) respectively. Because GPP and RES are the dominant terms for NEE, the fluxes can be related as,

$$NEE = GPP - RES \quad (1)$$

where NEE is negative for net sinks of atmospheric CO_2, GPP is positive, and RES is negative. The net flux from plants can be referred to as net primary productivity (NPP),

$$NPP = GPP - RES\_A \quad (2)$$

where RES_A is the autotrophic respiration.

Evidence from atmospheric CO_2 observations [*Ciais, et al.*, 1995; *Denning and Fung*, 1995; *Fan, et al.*, 1998] and land resources data [*Pacala, et al.*, 2001] indicates that the northern hemisphere NEE is an important sink for global atmospheric CO_2. However the dynamics of the processes that control this net sink and its spatial distribution remain controversial [*Gurney, et al.*, 2002]. Factors including climate [*Goulden, et al.*, 1998; *Lindroth, et al.*, 1998] and ecological disturbances [*Ciais, et al.*, 2005] can control the fine balance between GPP and RES that results in a sink or source for the NEE flux. The relationship between these factors and NEE is under debate [*Davidson and Janssens*, 2006]. An improved understanding of these gross fluxes is needed in order to forecast carbon fluxes that may result from and contribute to global change.

The relative contributions to NEE from RES and GPP are difficult to determine using current measurement techniques. The only relatively direct measurements of GPP and RES fluxes are at small scales using enclosures around leaves and soil chambers [*Sandoval-Soto, et al.*, 2005; *Vose and Ryan*, 2002]. These observations provide the basis for RES and GPP algorithms that are used in land surface flux models. The up-scaling of these measurements for regional and global applications remains highly uncertain. A measurement technique for determining RES and GPP fluxes at canopy, regional, and global scales is needed.

Measurements of atmospheric CO_2 and stable isotopes have been used to estimate the component fluxes with significant limitations. This approach uses data assimilation models to infer the NEE flux based on the difference between transport model CO_2 mixing ratios and observed mixing ratios [*Daley*, 1991; *Enting*, 2002]. Measurements of the stable carbon isotopes (^{12}C, ^{13}C) in atmospheric CO_2 samples are applied to partition the NEE fluxes into the GPP and RES components [*Bowling, et al.*, 2001]. This approach is based on the differences in the ratio of isotope mixing ratios in air that is taken up by photosynthesis and air that is emitted during respiration. A similar approach has been applied with oxygen isotopes (^{18}O, ^{16}O) in atmospheric CO_2 [*Farquhar, et al.*, 1993; *Francey and Tans*, 1987]. The limitation of the stable isotope approach is that one of the gross fluxes must dominate. However, the air masses sampled from surface stations and aircraft platforms are often influenced by a mixture of both GPP and RES.

Similarly, eddy flux techniques provide direct measurements of NEE and additional assumptions are used to deconvolve the component fluxes. With the eddy flux technique, NEE fluxes are calculated from simultaneous observations of CO_2 mixing ratios and wind speeds [*Baldocchi, et al.*, 1988]. The RES component can be estimated from the sum of the observed night-time fluxes, observed whole-day fluxes for periods when the plants have no leaves (deciduous forests), and estimates of day-time respiration [*Valentini, et al.*, 2000]. Daytime respiration is modeled as a function of observed night-

time fluxes, soil temperature, and air temperature. The GPP component is estimated as the difference between the NEE and RES fluxes. The daytime respiration function is based on the direct observations of RES and GPP from plant-scale experiments (branch enclosures and soil chambers). However, these small-scale observations may be highly uncertain for up-scaling to field, regional, and global applications.

Measurements from land resources inventories provide observations of soil and biomass carbon stocks which provide estimates of NEE and NPP [*Pacala, et al.*, 2001]. Direct measurements of GPP and RES fluxes are not available using this approach either.

It was recently proposed that simultaneous observations of atmospheric CO_2 and carbonyl sulfide (COS) could contain information relevant to partitioning the GPP and RES fluxes of CO_2 [*Montzka, et al.*, In Press]. Montzka et al. [In Press] presented a new data set from the NOAA Global Monitoring Division (GMD) of simultaneous observations of COS and CO_2 from a global air monitoring network. The analysis of this data in comparison with plant-scale [*Sandoval-Soto, et al.*, 2005], field-scale observations [*Falge, et al.*, 2002; *Xu, et al.*, 2002], and global observations [*Farquhar, et al.*, 1993; *Francey and Tans*, 1987] suggests that the surface flux of COS is closely connected to the GPP CO_2 flux but not to the RES CO_2 flux. If COS could be used as a tracer of GPP, then simultaneous observations of COS and CO_2 would allow for the partitioning of NEE fluxes into GPP and RES.

2.2 Background on COS Plant Uptake

Global and regional trends in COS have recently been described based on measurements from a global network of air monitoring sites and model results [*Montzka, et al.*, In Press; *Sandoval-Soto, et al.*, 2005; *Watts*, 2000]. The global mean mixing ratio is 484 ppt with no consistent annual increase or decrease. The major sources are from the

oceans, anthropogenic emissions, biomass burning, wetlands, and the oxidation of anthropogenic and ocean sources of DMS and CS_2. The primary sinks are plant uptake, soils uptake, OH oxidation, photolysis (stratosphere), and oxygen atom oxidation. The lifetime calculated as the global COS mass divided by the total global sinks is 1.5 to 3 years [*Montzka, et al.*, In Press]. Strong correlations between plant uptake of COS and CO_2 species have led many COS studies to calculate COS plant uptake as a function of published CO_2 plant uptake data [*Kesselmeier and Merk*, 1993; *Kjellström*, 1998; *Watts*, 2000].

Montzka et al. [In Press] reported the seasonal fluctuations of atmospheric COS mixing ([Spring – Fall]/mean) ratios to be highly correlated with the CO_2 fluctuations (r^2 = 0.9) with a regression slope of 6 ± 1. This correlation of COS with CO_2 is much stronger than with other measured species. The slope of 6 indicates a stronger seasonal fluctuation of COS than CO_2.

The preferential uptake of COS over CO_2 was also presented by Montzka et al. [In Press] as an altitudinal gradient. Both COS and CO_2 mixing ratios are reduced near the surface due to the plant sink, but the normalized gradient is more pronounced for COS. The ecosystem relative drawdown is calculated as,

$$U_{COS/CO2} = \frac{\left(\frac{{}^{6-8km}C_{COS} - {}^{<2km}C_{COS}}{{}^{6-8km}C_{COS}} \right)}{\left(\frac{{}^{6-8km}C_{CO2} - {}^{<2km}C_{CO2}}{{}^{6-8km}C_{CO2}} \right)} \quad (3)$$

where $U_{COS/CO2}$ is the ecosystem relative drawdown, and ${}^{6\text{-}8km}C_{COS,}$ ${}^{<2km}C_{COS}$, ${}^{6\text{-}8km}C_{CO2}$, and ${}^{<2km}C_{CO2}$ are the COS and CO_2 mixing ratios observed between 6 km and 8 km altitude and under 2 km altitude respectively (altitudes are above sea level). The average relative uptake value varied from 4 to 8 for observations at North American surface sites during the summer of 2007 [*Montzka, et al.*, In Press]. Although the normalized gradient

is larger for COS than CO_2, the total mass flux of CO_2 is larger than COS because the mean mixing ratio of CO_2 (370 ppm) is 10^6 greater than COS (450 ppt).

The high correlation of COS and CO_2 uptake was also observed in enclosures over plant branches [*Sandoval-Soto, et al.*, 2005]. The primary relative uptake was calculated as,

$$V_{COS/CO2} = \frac{{}^{in}C_{COS} - {}^{out}C_{COS}}{{}^{in}C_{CO2} - {}^{out}C_{CO2}} \quad (4)$$

where ${}^{in}C_{COS}$ and ${}^{in}C_{CO2}$ were the enclosure influent mixing ratios for COS and CO_2 while ${}^{out}C_{COS}$ and ${}^{out}C_{CO2}$ are the effluent mixing ratios of COS and CO_2. The primary relative uptake of COS from these experiments is 1.5 to 3.8. The primary relative uptake for the plant enclosure observations (equation 4) is smaller than the ecosystem relative uptake (equation 3) from the ambient observations. This is due to the fact that large sources of CO_2 respiration influence the ambient CO_2 measurement but do not influence the plant enclosure CO_2 measurement. Sandoval-Soto et al. [2005] indicated that the influences on COS outside of the enclosure were insignificant so that the ambient drawdown of COS was similar to the drawdown observed within the branch enclosure. However, the ambient drawdown of CO_2 was different than the branch enclosure drawdown due to the influences of autotrophic respiration beyond the branch and heterotrophic respiration. These CO_2 sources result in less drawdown of CO_2 in the ambient air than in the branch enclosure air. Less drawdown in the ambient CO_2 sample than the branch enclosure sample would results in a smaller denominator for relative drawdown (equation 3) than for relative uptake (equation 4), explaining the difference in results between Sandoval-Soto et al. [2005] and Montzka et al. [In Press].

The preferential uptake of COS over CO_2 for the branch-scale experiments is consistent with biochemical studies of COS and CO_2 in plant stomata. Both ambient gas species are expected to diffuse into plant stomata and dissolve into stomata water at similar rates because they have similar free-air diffusivities and aqueous solubilities.

During the initial stage of photosynthesis, most of the dissolved CO_2 will undergo hydrolysis by the enzyme carbonic anhydrase [*Gillon and Yakir*, 2001]. The COS is also rapidly consumed during hydrolysis by carbonic anhydrase [*Protoschill-Krebs and Kesselmeier*, 1992; *Protoschill-Krebs, et al.*, 1996]. The COS hydrolysis is non-reversible, and the COS becomes incorporated into amino acids and proteins [*Brown, et al.*, 1986; *Elliot, et al.*, 1989; *Kluczewski, et al.*, 1985]. The CO_2 hydrolysis is reversible so that approximately 2/3 is assimilated into carbohydrates and the remaining third is released back to the atmosphere [*Farquhar, et al.*, 1993; *Francey and Tans*, 1987]. This is roughly consistent with the preferential uptake of COS vs. CO_2 observed in the branch enclosure experiments.

This evidence for a GPP based surface sink of COS has led to a revised parameterization of the global COS plant uptake [*Sandoval-Soto, et al.*, 2005]. The GPP-based parameterization is,

$$ {}^{\text{Plant}}F_{COS} = {}^{GPP}F_{CO2} * \frac{[COS]}{[CO_2]} * V_{COS/CO2} \qquad (5) $$

where ${}^{\text{Plant}}F_{COS}$ is the surface sink for plant uptake of COS, ${}^{GPP}F_{CO2}$ is the surface sink of CO_2 due to photosynthesis, $[COS]/[CO_2]$ is the ambient mixing ratio of these two gases, and $V_{COS/CO2}$ (equation 4) is the plant primary relative uptake. The ratios discussed so far are summarized in Table 1.

Table 1. Summary of terms and significance for comparing COS and CO_2 influences during the growing season over North America.

Name	Formula	Typical Value	Physical Significance	Source
Ecosystem relative uptake ratio ($U_{COS/CO2}$)	Equation 3	2 to 8	Net ecosystem flux of COS to CO_2	[*Montzka, et al.*, In Press]
Primary relative uptake ratio ($V_{COS/CO2}$)	Equation 4	0.5 to 4.0	Plant uptake of COS to CO_2	[*Sandoval-Soto, et al.*, 2005]
Ratio of ambient mixing ratios	$[COS]/[CO_2]$	$1x10^{-6}$ to $1.3x10^{-6}$ ppt COS/ppm CO_2	-	This work

Past studies of global COS distributions using atmospheric transport models and mixing ratio observations have applied an NPP-based parameterization for the COS plant uptake [*Kettle, et al.*, 2002a; *Kjellström*, 1998; *Watts*, 2000],

$$^{Plant}F_{COS} = {}^{NPP}F_{CO2} * \frac{[COS]}{[CO_2]} \quad (6)$$

where $^{NPP}F_{CO2}$ is the surface NPP flux of CO_2. The GPP-based estimates using equation 5 are approximately 4 to 6 times the NPP-based estimates using equation 6. This is because GPP is approximately double NPP and typical relative uptake estimates are between 2 to 3 [2*(2 to 3) = 4 to 6]. The larger global sink estimates by the GPP parameterization indicate that the plant uptake is the dominant global COS sink and that the global COS sources have been largely underestimated in past global balances of COS sources and sinks [*Montzka, et al.*, In Press; *Sandoval-Soto, et al.*, 2005].

The Montzka et al. [In Press] analysis provided a qualitative validation of the GPP-based parameterization and the Sandoval-Soto et al. [2005] provided a plant scale validation. However, a quantitative validation at regional or global scales is needed to validate this flux scheme. Validation studies of surface fluxes at these larger spatial scales are performed by comparing observations of atmospheric mixing ratios with modeled mixing ratios. The modeled mixing ratios are a result of driving an atmospheric transport model with the best available estimate of the surface flux. This approach is suitable for regional applications because the spatial and temporal variations of the atmospheric mixing ratios are a result of the integrated influence of surface fluxes over regional spatial scales [*Gloor, et al.*, 2001; *Lin, et al.*, 2003].

The quantitative validation of the COS plant uptake parameterization is prerequisite to developing a COS-CO_2 method for partitioning the NEE flux into GPP and RES components. In addition, the validation of the COS plant uptake is useful for improving the understanding of the global sulfur cycle and stratospheric chemistry. COS

is the largest non-volcanic source for stratospheric sulfate aerosol and plays an important role in climate forcing and stratospheric ozone chemistry [*Andreae and Crutzen*, 1997; *Crutzen*, 1976]. COS is implicated in the radiative forcing of climate because it contributes to sulfur in the stratospheric aerosol layer. The GPP-based estimates of the COS plant sink are approximately 4 to 6 times the NPP-based estimates which indicates that past studies of the global cycle have largely underestimated COS sources. The validation of the GPP-based fluxes would motivate a new analysis of the global COS sources.

In order to provide a quantitative analysis of the COS plant uptake, this chapter presents a top-down analysis of alternative flux parameterizations. The alternative COS plant uptake surface fluxes were evaluated by driving the STEM model with the fluxes and comparing with observed mixing ratios. Three STEM simulations of the COS concentrations were completed using the three different COS plant uptake parameterizations summarized in Table 2. Two GPP-based COS fluxes (equation 5) are developed using CO_2 fluxes from the SiB and CASA land surface models. The NPP-based fluxes published in Kettle et al. [2002] are also used.

Table 2. Summary of alternative COS plant uptake fluxes used in the STEM runs for evaluation with INTEX-NA observations.

COS Flux Name	Parameterization	[COS]/[CO_2]	$V_{COS/CO2}$	Temporal Reference
SiB	GPP (equation 5)	1.1×10^{-6}	Gridded	Hourly, 2004
CASA	GPP (equation 5)	1.1×10^{-6}	Gridded	3-Hourly, 2004
Kettle	NPP (equation 6)	1.4×10^{-6}	None	Monthly, Climatological

Observations of COS and CO_2 are used from the NASA INTEX-NA experiment during July and August of 2004 over North America [*Blake, et al.*, Submitted]. Continental observations during the growing season are utilized because the variance of the CO_2 and COS mixing ratios is dominated by the plant uptake. The INTEX-NA

observations are the most extensive regional data of COS and CO_2 during the growing season. The NOAA GMD record of measurements of COS and CO_2 from surface sites and aircraft is another excellent data source that should be used in future studies [*Montzka, et al.*, In Press]. Validating the surface flux over North America is also of great interest because there is evidence that the northern hemisphere NEE sink may be largely concentrated in North America [*Fan, et al.*, 1998].

The objective of this chapter is to refine and validate the GPP-based COS flux parameterization using a regional atmospheric transport model and atmospheric observations. The objective of the following chapter is to apply the validated COS flux scheme for partitioning the NEE CO_2 flux into GPP and RES components.

In section 2.3 the methods for developing the COS plant uptake estimates and the subsequent model runs are presented. In section 2.4 the observation methods are described. In section 2.5 the observations are analyzed to confirm the dominant biosphere influence and provide a rough approximation of the primary relative uptake (equation 4). In section 2.6 the modeled fluxes and modeled mixing ratio results are presented and compared with observations. In section 2.7 the top-down results are interpreted to suggest revisions to the COS GPP plant sink parameterization.

2.3 Model COS Experimental

2.3.1 Transport Model

The STEM regional chemistry model was used to simulate mixing ratios of COS and other species during the July/August simulation period. The horizontal domain has a 60 km grid resolution covering the continental U.S. and parts of Canada, Mexico, and adjacent oceans (Figure 5). The vertical domain includes 21 sigma layers that extend from the surface up to 100 hPa. The STEM model outputs mixing ratios at hourly time

steps for every grid cell in the model domain. The STEM model is based on inputs of meteorology, boundary/initial conditions, and surface fluxes as summarized in Figure 2.

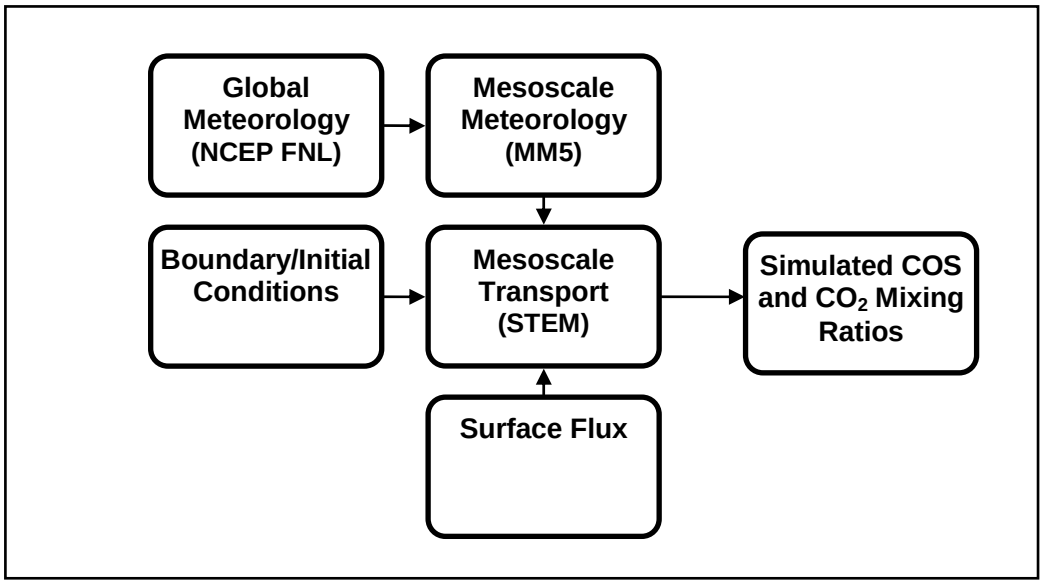

Figure 2. Process diagram for atmospheric transport model.

2.3.2 Boundary/Initial Conditions

The COS model runs were driven by fixed boundary conditions estimated from observations from INTEX-NA. The vertical profiles for observed COS are shown in Figure 3 for all flights (black) and for flight 3 which was over the Pacific Ocean (red). The mean mixing ratio during flight 3 of 480±20 ppt is consistent with observations from marine boundary layer sites in the NOAA GMD air monitoring network. The mean INTEX-NA observations to the north and east of the domain are 450±20 ppt. The western boundary conditions are set to 480 ppt and the other top and lateral boundary conditions are set to 450 ppt. A discussion of the sensitivity of model results to boundary conditions is included in the following section.

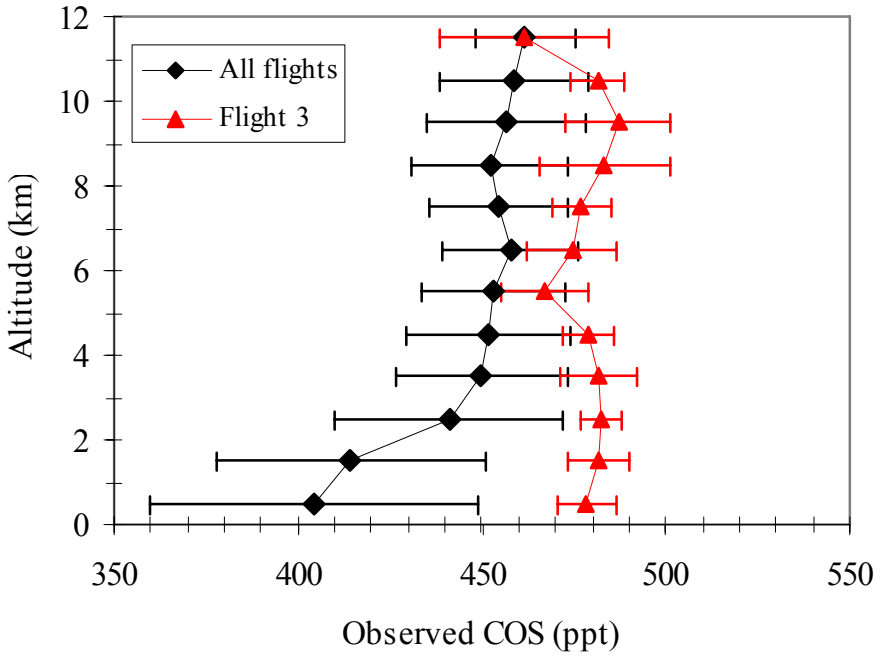

Figure 3. Vertical profiles of observed COS mixing ratios for all DC8 INTEX-NA flights (black) and for only flight 3 over the Pacific Ocean (red).

2.3.3 COS Surface Flux Estimates Other Than Plant Uptake

The COS surface flux inputs for the COS model, other than plant uptake, were interpolated from climatological gridded fluxes for July and August with a one degree spatial resolution and monthly temporal resolution including the soil sink, industrial sources, and the ocean sink [*Kettle, et al.*, 2002a]. The reactive chemical sources from oxidation of dimethyl sulfide and carbon disulfide were included as surface sources in the climatological gridded fluxes.

The loss of COS by oxidation with the atmospheric hydroxyl radical was neglected because the boundary layer July lifetime of more than a years for this process [*Kettle, et al.*, 2002a] is much larger than the transport lifetime in the boundary layer of the model domain of several days. It is important to note that these fluxes were estimated

in a global balance based on the NPP-based approach for estimating plant uptake of COS. The GPP-based approach yields plant uptake flux estimates that are 4 to 6 times the NPP-based fluxes. If the GPP-based approach had been used in the global balance then the COS source flux estimates would have been larger. The uncertainty on many of the COS surface flux sources is very high [*Watts*, 2000].

2.3.4 COS Plant Uptake Flux Estimates

Three alternative estimates of COS plant uptake are used to drive the three STEM model runs as summarized in Table 2. The SiB and CASA fluxes follow the GPP-based approach and are the product of the CO_2 flux, the ratio of ambient mixing ratios, and the primary relative plant uptake. The Kettle fluxes are interpolated from the global, gridded NPP-based COS fluxes presented in Kettle et al. [2004].

The primary relative uptake term is calculated for each surface grid cell in the STEM model domain using a land cover map [*WWF*, 1999] and a table of relative uptake terms for different land cover [*Sandoval-Soto, et al.*, 2005]. The biome types for the land cover map were matched to the land cover types reported in the Sandoval-Soto et al. [2005] as shown in Table 3. The land cover map does not include a category for agriculture which may be acceptable because the agriculture relative uptake in Sandoval-Soto et al. [2005] is close in value to relative uptakes for the adjacent biome types of savannas and mixed forests. A GIS was used to calculate the area weighted average value of the relative uptake for each STEM surface grid cell. The mean relative uptake for the entire domain is 2.2 with the spatial variability mapped in Figure 4. The relative uptake values reported in Sandoval-Soto et al. [2005] vary over an order of magnitude for crops and a factor of 3 for forests. The influence of this uncertainty is analyzed in the results section.

Table 3. Primary relative uptake (V_{COSCO2}) observed from field experiments for different biome types.

Biome	Percent Area of Domain	Primary relative Uptake
Tropical & Subtropical Moist Broadleaf Forests	2.7%	2.65
Tropical & Subtropical Dry Broadleaf Forests	3.8%	2.65
Tropical & Subtropical Coniferous Forests	3.8%	2.65
Temperate Broadleaf & Mixed Forests	11.8%	2.35
Temperate Conifer Forests	8.3%	2.2
Boreal Forests/Taiga	14.5%	1.35
Tropical & Subtropical Grasslands, Savannas & Shrublands	4.2%	2.2
Temperate Grasslands, Savannas & Shrublands	14.7%	2.5
Flooded Grasslands & Savannas	5.1%	2
Tundra	0.7%	2.5
Mediterranean Forests, Woodlands & Scrub	6.0%	2.2
Deserts & Xeric Shrublands	12.6%	2.2
Mangroves	0.5%	2
Snow, ice, glaciers, and rock	2.8%	2

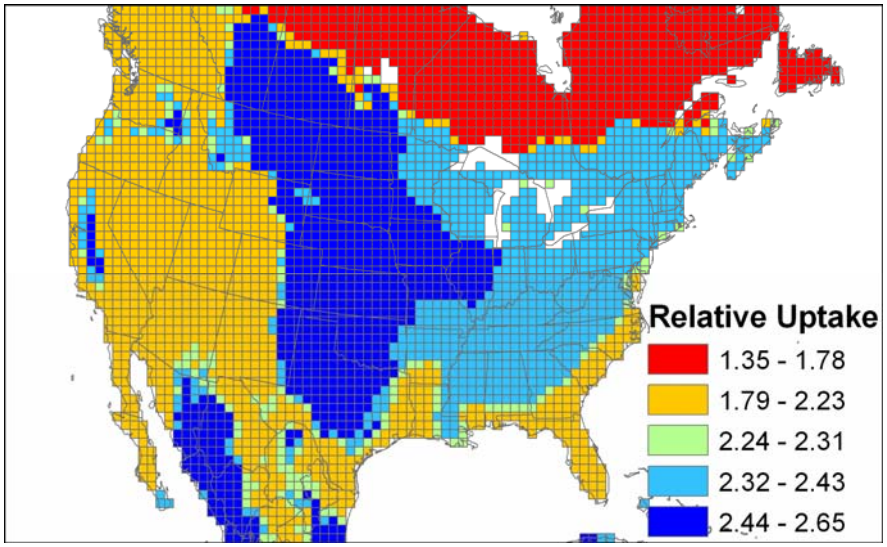

Figure 4. Relative uptake of COS to CO_2 as an area weighted average for each grid cell.

The ratio of mixing ratios ([COS]/[CO_2]) is the next term (equation 5) used in calculating the GPP-based COS plant fluxes. The mean for the INTEX-NA observations is $1.1x10^{-6} \pm 8.9x10^{-8}$ ppm COS/ppm CO_2. The ratio of mixing ratios used in the COS plant uptake calculations is fixed at $1.1x10^{-6}$ ppm COS/ppm CO_2 given the small variation of this term relative to the variation in the relative uptake term.

The final term in the COS plant flux calculation is the GPP CO_2 flux. The CO_2 fluxes were obtained from the Simple Biosphere Model Version 3 (SiB) [*Denning, et al.*, 1996; *Sellers, et al.*, 1996a; *Sellers, et al.*, 1996b] and the Carnegie-Ames-Stanford approach (CASA) Biosphere model [*Potter, et al.*, 1993; *Randerson, et al.*, 1996]. The SiB and CASA land surface models are driven by landcover data, meteorological data from climate models and plant density data from satellite observations according to the Normalized Difference Vegetation Index (NDVI). The SiB runs were completed by Ian Baker at the University of Colorado at a 1 degree by degree spatial resolution and hourly temporal resolution. The landcover data for the SiB runs is 1 degree by 1 degree time invariant landcover derived from 1-km AVHRR data. The NDVI data for the SiB runs is from GiMMSg with a spatial resolution of 1 degree and temporal resolution of 15-days. The meteorology input is from the NCEP-2 reanalysis at a 1 degree by 1 degree spatial resolution and 6-hourly temporal resolution.

The CASA model runs were completed by Jim Collatz and Randy Kawa at NASA Goodard Space Flight Center (GSFC) with a 3 hourly temporal resolution and 1 by 1.25 degree spatial resolution. The meteorology input is Goddard Modeling and Assimilation Office GEOS4 reanalysis at the same resolution. The CASA runs use the same landcover and NDVI data that are used in the SiB runs. However, the NDVI for the SiB runs was interpolated to daily values while the CASA uses the same monthly value throughout the month. The primary differences between the SiB and CASA results should be attributed to the different meteorological drivers and different water stress parameterizations.

In addition to the GPP-based estimates of COS plant uptake, an NPP-based estimate was used by interpolating from the published gridded COS plant uptake fluxes in Kettle et al. [2005]. The Kettle fluxes are climatological, and have a 1 degree by 1 degree, monthly resolution [*Kettle et al., 2002*]. These are the only published values for gridded COS fluxes. The Kettle NPP fluxes were calculated using equation 6 with input from climatological NPP data [*Fung, et al.*, 1987] and a fixed [COS]/[CO_2] ratio of $1.4x10^{-6}$. The INTEX-NA average ratio of [COS]/[CO_2] is $1.1x10^{-6}$ which is smaller than the Kettle ratio because the Kettle ratio is a global average while the INTEX-NA average is based on samples close to the plant uptake which have a preferential drawdown for COS over CO_2.

2.3.5 STEM Inputs for CO_2 Simulations

Simulations of CO_2 mixing ratios are also completed using the STEM transport model to access the accuracy of the CO_2 fluxes that are used in the COS plant uptake parameterization. The flux estimates are RES and GPP fluxes from CASA and SiB. The ocean fluxes were 1 degree by 1 degree, monthly, climatological ocean fluxes for 2000 [*Takahashi, et al.*, 1999]. The fossil fuel emissions were scaled to 2004 based on 1 degree by 1 degree, time invariant, fossil fuel emissions for 1995 [*Brenkert*, 1998]. The annual 2004 fossil fuel emissions were scaled to summer emissions based on the U.S. annual cycle with an amplitude of 30% [*Blasing, et al.*, 2003]. The interannual factor (1.15) and seasonal factor (0.86) approximately offset each other. The time varying boundary conditions for CO_2 tracers of the biosphere, ocean, and fossil fuel fluxes are provided by the TM5 global chemical transport model [*Peters, et al.*, 2004].

2.4 Observation Methodology

Observations of COS, CO_2 and other trace gases were made from the DC8 aircraft during July and August of 2004 as a part of the NASA INTEX-NA field experiment [*Blake, et al.*, Submitted]. The flights of the DC8 aircraft were typically during daylight hour and spanned the dates of July 1 to August 14, 2004. Most flights were over the eastern United States and Canada as shown in Figure 5.

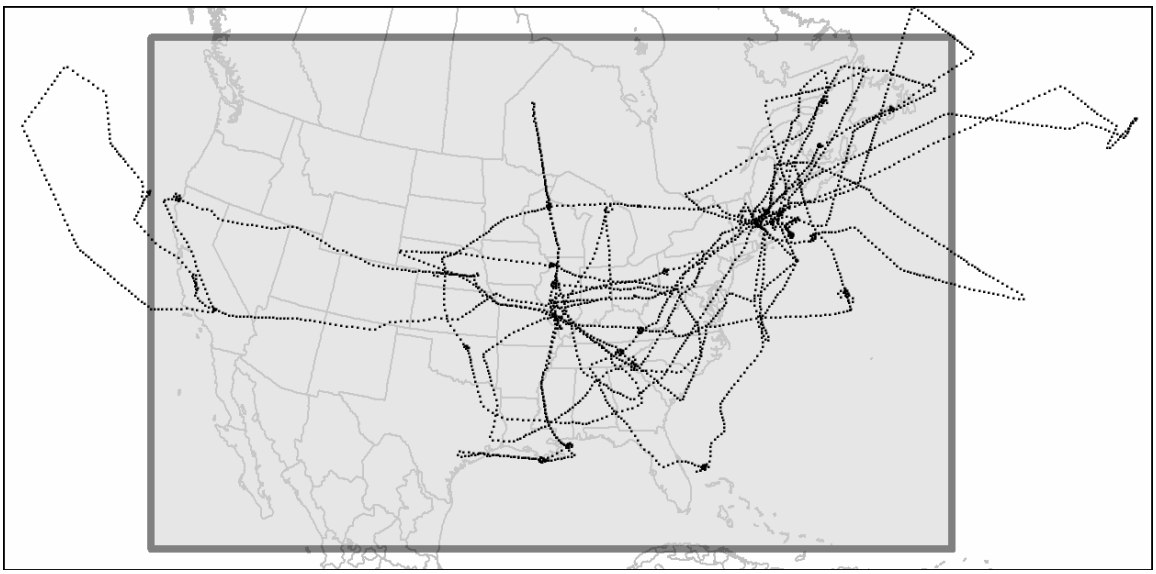

Figure 5. DC8 flight paths during the July/August 2004 INTEX-NA campaign (dotted lines) and STEM regional model domain (shaded box).

COS observations were made by Donald Blake's group from UC Irvine. Whole air samples were collected in evacuated two-liter stainless steel canisters every 1 to 5 minutes. The samples were analyzed for COS and other species in the Blake-Rowland laboratory at the University of California, Riverside. The measurement precision was 5% with a detection limit less than 20 pptv. The gas was always present above the detection limit.

In situ observations of atmospheric CO_2 (±0.25 ppm-molar uncertainty) were made by Stephanie Vay's group from NASA Langley. The measurements were made

with a modified Li-Cor model 6252 nondispersive infrared analyzer at a frequency of 1Hz. In-flight calibrations were performed every 15 minutes using standards traceable to the WMO Central Laboratory at NOAA/GMD [*Vay, et al.*, 2003]. The COS and CO_2 observation data used in this study is the 1-mintue averaged data set that is publicly available from the INTEX-NA ftp server (http://www-air.larc.nasa.gov/cgi-bin/arcstat).

Observations from eddy flux measurements are also used for comparison with the modeled CO_2 fluxes. Eddy flux results are analyzed from the Bondville site, a crop field (corn and soybeans) in central Illinois [*Hollinger, et al.*, 2005]. The Bondville data includes fluxes of NEE, RES, and GPP developed from simultaneous measurements of CO_2 concentrations and wind velocities from a 10 meter tower. The eddy flux data was downloaded from the FLUXNET CDIAC ftp server (http://www-eosdis.ornl.gov/FLUXNET/).

2.5 Relation of COS to CO_2 in INTEX-NA Observations

The relation of the COS to CO_2 observations is examined to ensure that the mixing ratio variation is dominated by the biosphere influence and to provide an approximation for the primary relative uptake term (equation 4). The COS observations are plotted against the CO_2 observations in Figure 6. The strong correlation of COS with CO_2 ($r^2 = 0.7$, n = 2872) is much higher than between CO_2 and other observed tracers that are strongly influenced by a surface flux (e.g. CO).

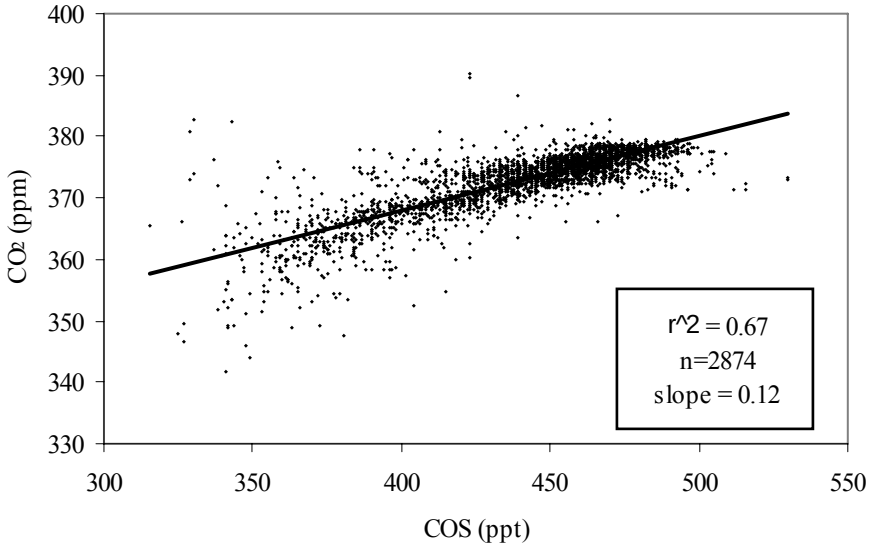

Figure 6. Mixing ratios of COS vs. CO_2 observed during the INTEX-NA DC8 flights.

In Figure 7, the COS to CO_2 plot is shown for all flights in black and the Midwest flights in red (Illinois, Indiana, and Ohio). The steeper slope for the Midwest flights may be due to the influence of C4 plants (e.g. corn, grass) which should have a more efficient CO_2 metabolism than C3 plants but the same COS uptake mechanism [*Montzka, et al.*, In Press]. The outliers that have low concentrations of COS but high concentrations of CO_2 are shown in blue. These outliers intersected large fossil fuel combustion plumes offshore of New England which had enhancements of CO_2 by up to 20 ppm but no observed enhancement of COS. The outliers indicated in green intercepted an air mass heavily influenced by respiration. While most sampling is done during the GPP influenced hours, this respiration influenced air mass was sampled at the early part of flight 7 (July 18th) at its furthest western reach where the influence of the previous night's respiration was still strong. The model also predicts larger RES concentrations than GPP concentrations at this point.

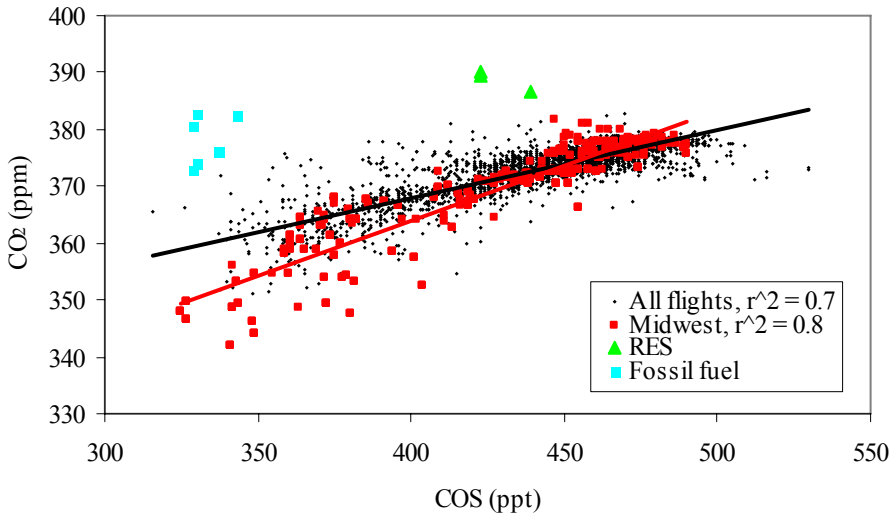

Figure 7. Mixing ratios of COS vs. CO_2 observed during the INTEX-NA DC8 flights for all flights (black) and flights over Illinois, Ohio, and Indiana (red). Outlier points are influenced by respiration (green) and fossil fuel emissions (blue).

The ecosystem relative uptake (equation 3) from the INTEX-NA flights was calculated with a mean value of 5.8±1.8. This uptake is similar to the average reported by Montzka et al. [2005] which ranged from 4 to 8 for the NOAA GMD aircraft sampling during the summer of 2005. The spatial variability of these ecosystem relative uptake results is shown in Figure 8 with decreased values over the Midwest agriculture region. Reduced ecosystem relative uptake over the Midwest may be due to the influence of C4 plants in this region which have a more efficient metabolism for CO_2 assimilation than the predominant C3 plants but a similar process for COS uptake as the C3 plants. This suggests that the primary relative uptake should also be lower over the agriculture region. However the primary relative uptake values for agriculture reported in Sandoval-Soto et al. [2005] are not significantly lower than for other land cover types.

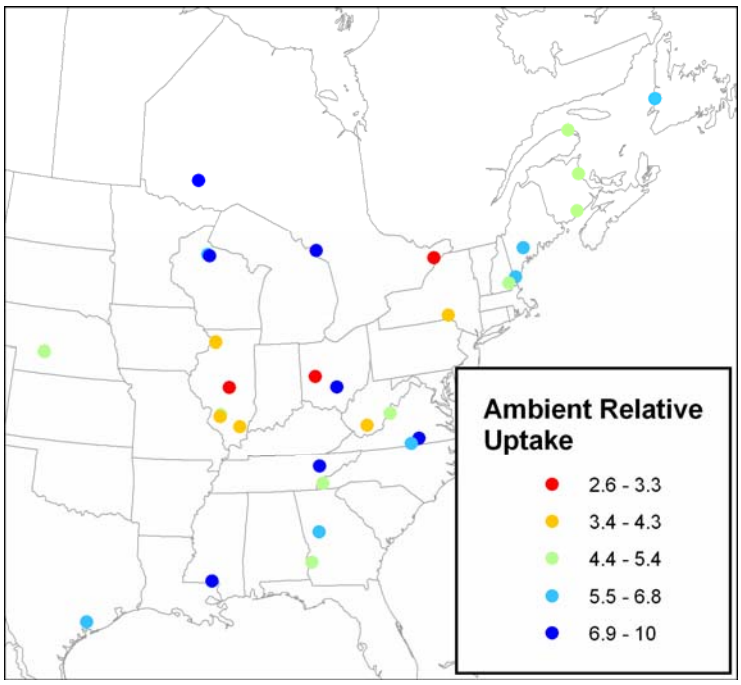

Figure 8. Ecosystem relative uptake of COS to CO_2 calculated from INTEX-NA observations using equation 3.

The low ecosystem relative uptake values over the Midwest could also be influenced by factors other than C3/C4 vegetation such as fossil fuel CO_2 sources, time variation of the biosphere fluxes, and long range transport. For example, the time of day of the measurement could result in larger values in the morning due to the influence of RES. For the INTEX-NA data, the correlation between time of sampling and ecosystem relative uptake is weak.

The ecosystem relative uptake provides a rough constraint on the primary relative uptake. As presented in Montzka et al. [2005], the ecosystem relative uptake can be approximated by the product of the primary relative uptake and the ratio of GPP to NEE CO_2 fluxes. The ratio of GPP to NEE CO_2 fluxes for July is on average 5.7 for SiB and 4.4 for CASA model fluxes. Similarly, from eddy flux measurements over North America, the ratio of GPP to NEE ranges from 3.7 to 7.1 (Table 4) as calculated from

data presented in Falge et al. [2002]. For a mean ecosystem relative uptake of 5.8 and a GPP/NEE ratio of 3.7 to 7.1, the resulting primary relative uptake should vary between 0.8 and 1.6. This range of 0.8 to 1.6 falls on the lower end of the range of uptake values that were summarized in Sandoval-Soto et al. [2005].

Table 4. Ratio of annual sum of GPP to NEE fluxes for the growing season calculated from eddy flux data.

Bioregion	GPP/NEE
Temperate coniferous forest	4.4
Temperate deciduous forest	7.1
Grasslands	3.7
Crops	5.1

The frequency distribution and vertical profile is shown for the ratio of [COS]/[CO_2] observations in Figure 9. The frequency distributions are shown in for all INTEX-NA flight path observations, observations below 2 km altitude, and observations above 2 km altitude. The high density region near 1.3 ppt/ppm is more typical of the well mixed observations at higher altitudes and is similar to ratios applied in global analyses [*Kettle, et al.*, 2002a; *Montzka, et al.*, In Press]. The high density region near 1.1 ppt/ppm is influenced by the observations near the surface which are more sensitive to the preferential plant uptake of COS over CO_2. The vertical profile of the observed ratios decreases with decreasing altitude due to proximity to the relative uptake. Extending this trend to the surface results in a [COS]/[CO_2] ratio of close to 1.1×10^{-6}.

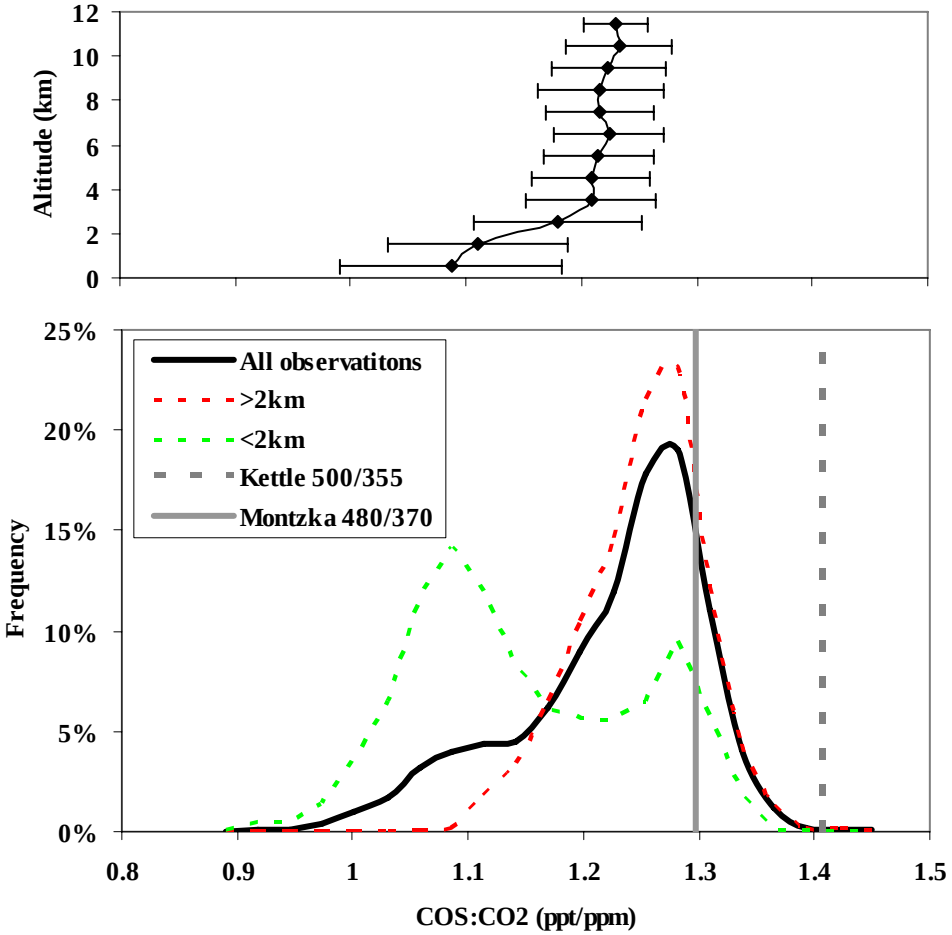

Figure 9. Observed ratio of COS to CO_2 mixing ratios (ppt COS / ppm CO_2) on INTEX-NA DC8 flight paths is shown as a vertical profile (top) and frequency distribution (bottom). The distributions are for all observations (thick black line), observations above 2 km altitude above surface level (thin black line), and observations below 2 altitude (dashed green line). Ratios used in past studies are shown for a global study (dashed red line) and a ratio applied to the Northern Hemisphere (solid grey line).

2.6 Flux and Mixing Ratio Results

2.6.1 CO_2 Fluxes and Mixing Ratios

The CO_2 surface fluxes are used to drive STEM and compare with INTEX-NA CO_2 observations to examine the accuracy of the fluxes before use in the COS plant uptake parameterizations. However, this validation provides information about the net CO_2 flux and does not necessarily provide support for the GPP CO_2 component which is used in the COS flux parameterization. The vertical profile of the GPP, RES, and total CO_2 mixing ratios are shown in Figure 10. The magnitude of the SiB components is larger than the magnitude of the CASA components, however the net CO_2 flux is relatively similar. The total modeled mixing ratios decrease with altitude at a slower rate than the observations, indicating that the GPP flux may be too small or the RES flux may be too big. Although the flights are during the daytime, the GPP and RES influences are mixed with the average ratio of modeled RES to GPP mixing ratio components of 0.8 along the flight paths. The largest model overestimates occur over the mid-continent which is due to the large biosphere fluxes in this region.

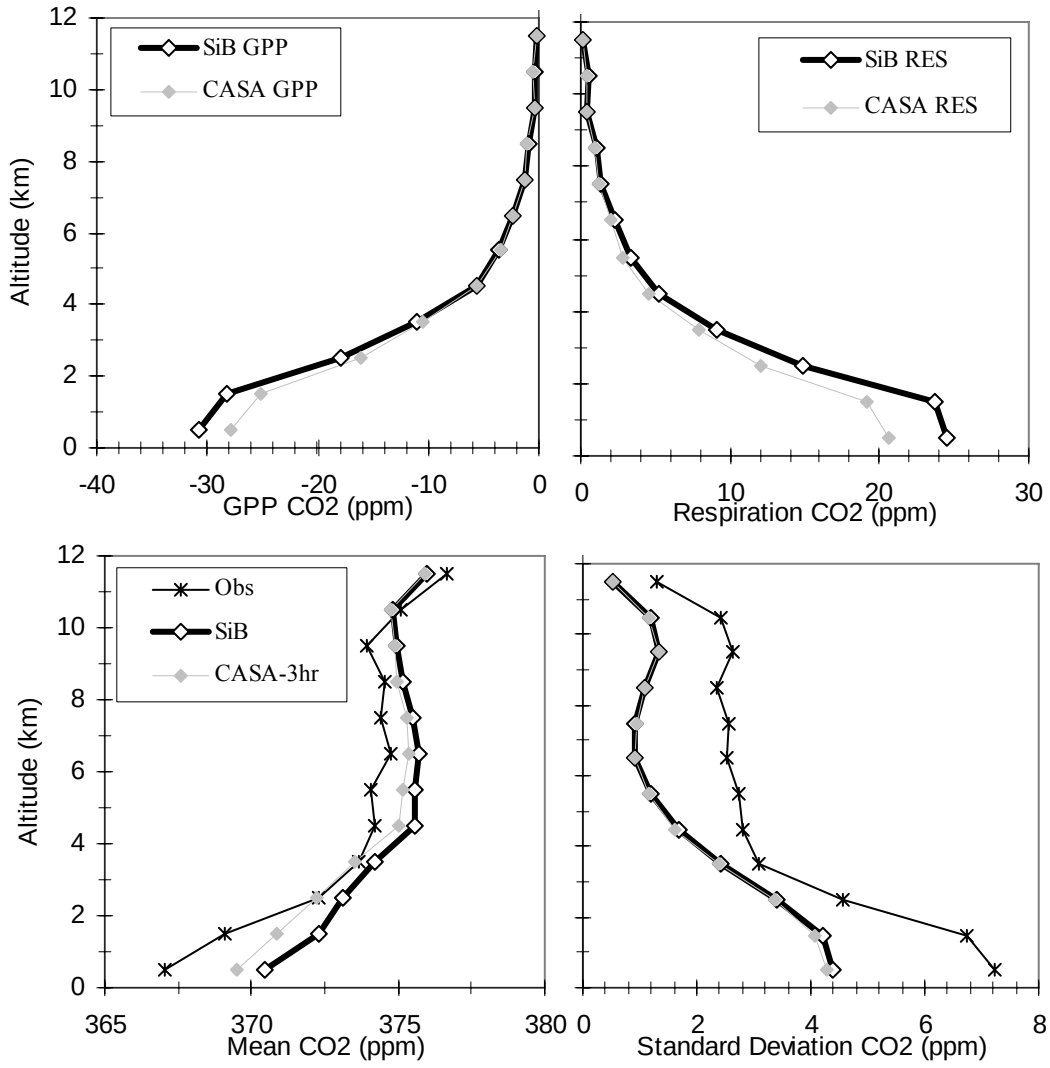

Figure 10. Vertical profiles of mean CO_2 mixing ratios for GPP (top left) and RES (top right) along the INTEX-NA DC8 flight paths. The bottom plots show the vertical profile of mean and standard deviations for the observed and total modeled CO_2 mixing ratios.

The CO_2 mixing ratio errors are largest and most consistent from flight to flight over Illinois where the model overestimates the near surface mixing ratios. This region is dominated by agriculture which is an ecoregion that is less well resolved by SiB and CASA than other ecoregions. Analyzing the fluxes in this area may be on the order of the largest errors in the SiB and CASA fluxes. Although there is no published error

analysis of the GPP CO_2 fluxes for these SiB and CASA fluxes, the error can be approximated from a preliminary comparison with eddy flux data. Data for NEE, GPP, and RES surface fluxes from the Bondville eddy flux site in central Illinois are compared with SiB and CASA fluxes to approximate the GPP flux error. This validation approach is limited by the fact that the Bondville measurements are made at 1 meter above the ground which has a very small influence region compared to the SiB 1 degree by 1 degree surface flux resolution.

A time series of GPP fluxes for early 7/2/2004 through 7/3/2004 is shown for CASA, SiB, and Bondville in Figure 11. The CASA and SiB fluxes underestimate the magnitude of the Bondville GPP flux which is one reason that the mixing ratios were consistently overestimated in the Illinois region. The daytime Bondville fluxes for July and August 2004 are on average 1.5 times the SiB fluxes and 1.6 times the CASA fluxes.

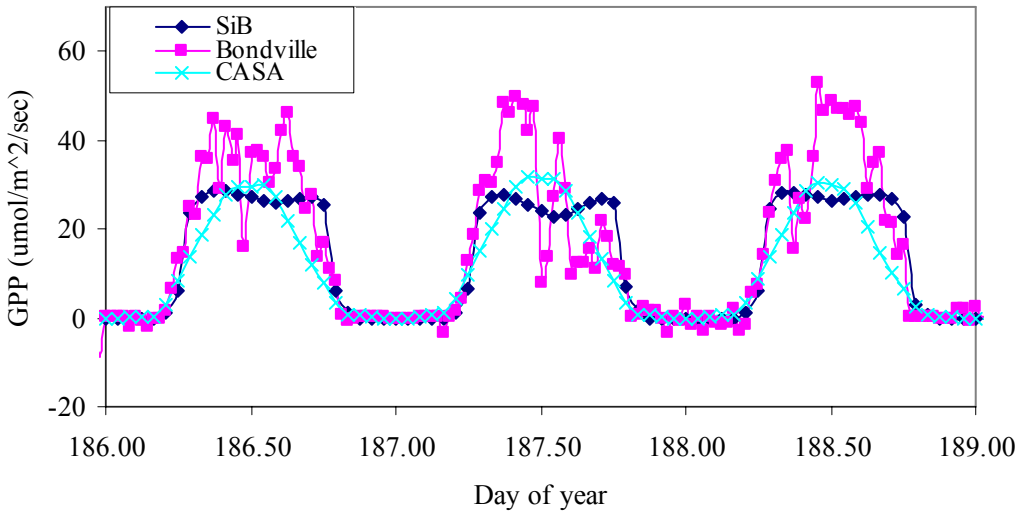

Figure 11. GPP CO_2 flux from SiB, CASA, and Bondville eddy flux site for 7/2/2004 through 7/4/2004.

2.6.2 COS Fluxes

The average July COS plant uptake fluxes from the CASA, SiB, and Kettle approaches are mapped in Figure 12. The GPP-based CASA and SiB fluxes (equation 5) are approximately 4 times the NPP-based Kettle fluxes (equation 6) which is consistent with the approximation that GPP is double NPP and the mean primary relative uptake value of 2 used in the CASA and SiB COS flux calculations. The Kettle fluxes are largest in the northeast while the CASA and SiB fluxes are largest over the mid-continent region. This spatial difference is driven by the large mid-continent CO_2 GPP fluxes from the CASA and SiB models as well as the larger relative uptake over the mid-continent.

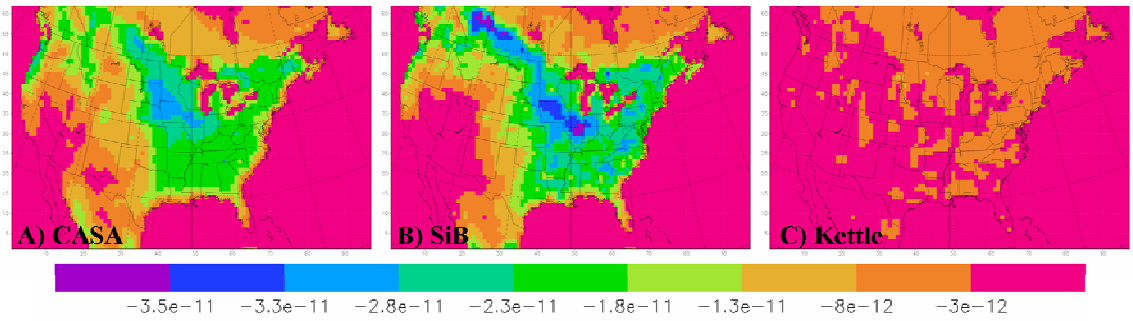

Figure 12. Average July COS plant uptake surface fluxes (moles COS/m^2/s) for a) CASA, b) SiB, and c) Kettle approaches.

2.6.3 COS Mixing Ratios

The COS fluxes for plant uptake and other components were used to drive the STEM model for simulating mixing ratios over North America. The modeled mixing ratios were interpolated to the INTEX-NA DC8 flight paths. The mean modeled mixing ratios along the INTEX-NA flight paths over land and below 2 km altitude above ground level, are shown in Figure 13. The mean CASA and SiB plant uptake mixing ratios are

approximately 4 times the Kettle mixing ratio as was the case with the fluxes. The anthropogenic and ocean mixing ratios have relatively small mixing ratios compared to the plant uptake. The CASA and SiB plant uptake mixing ratios are approximately 10 times the soil sink component while the Kettle mixing ratios are approximately 2.5 times the soil component.

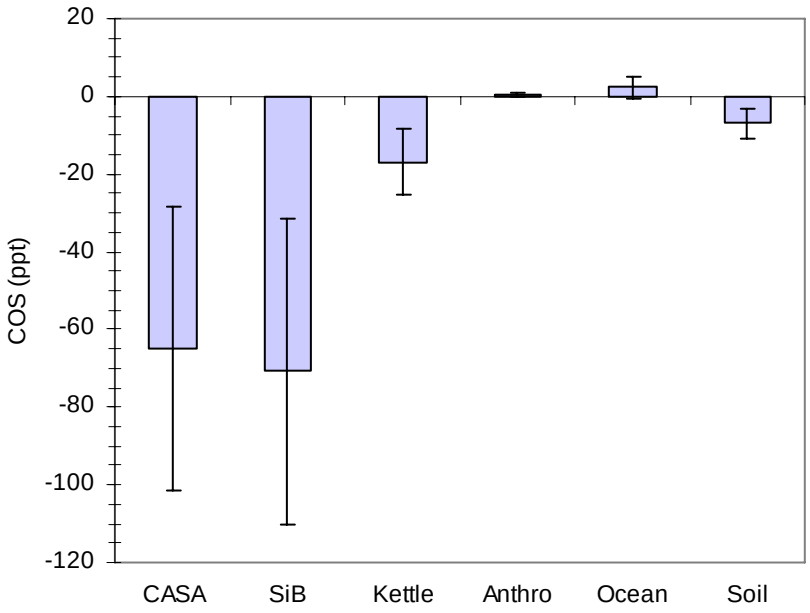

Figure 13. Comparison of mean modeled COS component mixing ratios along the INTEX-NA DC8 flight paths, below 2 km altitude above surface level for CASA plant uptake, SiB plant uptake, Kettle plant uptake, anthropogenic emissions, ocean sources, and soil sinks. Error bars are standard deviations.

Three alternatives of the total modeled COS mixing ratios were calculated by adding the three plant uptake component to the mixing ratios from the STEM runs driven by the other flux components and the boundary conditions. The vertical profiles of the total COS mixing ratios for the different schemes is compared with the observed mixing

ratios in Figure 14. More drawdown is needed for the Kettle NPP-based scheme as expected from plant and enzyme experiments that show that COS plant uptake is related to GPP and not NPP [*Montzka, et al.*, In Press; *Sandoval-Soto, et al.*, 2005]. The GPP-based schemes using the SiB and CASA fluxes overestimate the magnitude of the sink. The GPP-based error is predicted by the analysis of the observations in the previous section which indicated that the primary relative uptake should range from 0.8 to 1.6 while the published values used in the CASA and SiB COS plant uptake estimates had a mean of 2.2. Further consideration of the source of error in the GPP-based results and a revised GPP-based estimate is provided in the following section.

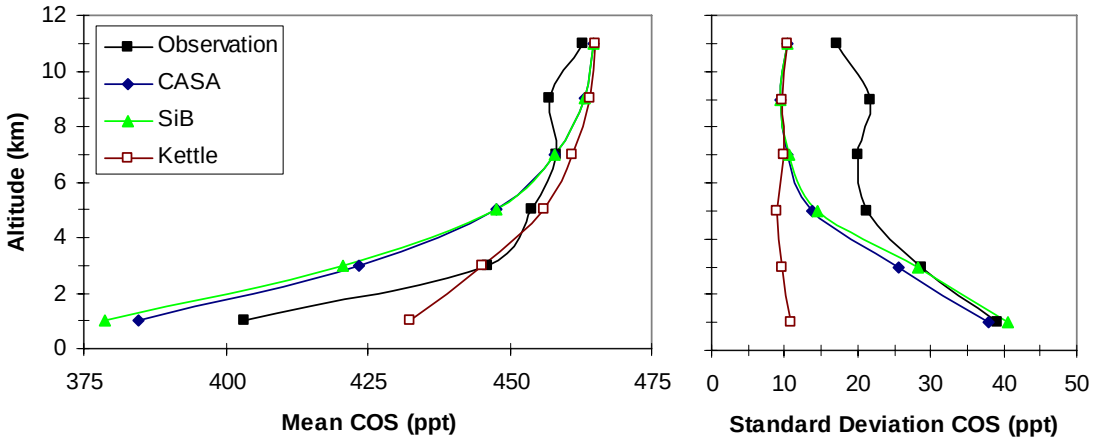

Figure 14. Mean (left) and standard deviation (right) mixing ratio profile for observed and modeled COS along the INTEX-NA DC8 flight paths over land.

2.7 Error Analysis and Revised Relative Uptake Values

The near-surface underestimate of mixing ratios by the GPP-based approaches (CASA and SiB) is most likely due to error in the primary relative uptake term in the flux calculations (equation 5). Other potential sources of error are discussed below. The primary relative uptake values used in the GPP-based flux calculations were developed from published data that have large uncertainty with values ranging over an order of magnitude for agriculture land cover and by a factor of 3 for forest land cover. The approximation of the primary relative uptake based on observations presented in section 2.5 suggests an average value of 1.1, approximately half of the mean relative uptake value used in the COS flux calculation. This suggests that a scaling factor of 0.5 multiplied by the relative uptake would minimize the mixing ratio error.

The mixing ratio error is found to be minimized by applying a scaling factor of approximately 0.5 to the COS plant uptake surface fluxes. The surface flux scaling factor, alpha, and the sum of the square mixing ratio errors is reported in Table 5. A scaling factor of 0.6 is required to minimize the error for the CASA model runs and a factor of 0.5 is required for the SiB model runs.

Table 5. Sum of mean square error for modeled COS mixing ratios using different surface flux scaling factors (Alpha).

	Sum Mean Square Error	
Alpha	CASA	SiB
0.4	-	1.219E+06
0.5	1.173E+06	1.157E+06
0.6	1.151E+06	1.165E+06
0.7	1.188E+06	1.241E+06
0.8	1.283E+06	1.387E+06
1.0	1.648E+06	1.887E+06

Other sources of error are unlikely to account for the large near-surface mixing ratio error. Other sources of error could be due to uncertainty in the two other terms in the COS flux calculation (equation 5), boundary conditions, initial conditions, modeled transport, missing COS sources and measurements. The ratio of [COS]/[CO_2] term in the flux calculation has a standard deviation of 8% which cannot account for the 0.5 scaling factor required to minimize the error. The GPP CO_2 flux term in the COS flux calculation may have errors that are on the order of 0.5. However, the preliminary analysis of GPP error by comparison with eddy flux data suggests that CO_2 GPP fluxes may be underestimated by the CASA and SiB models. If the modeled GPP were increased, that would only increase the near-surface COS mixing ratio error.

The boundary conditions and initial conditions are also unlikely to account for the near-surface COS mixing ratio error. The boundary condition error is indicated by the COS mixing ratio error at higher altitudes in Figure 14. At altitudes above 6 km the model mixing ratios overestimate the observations, indicating that the boundary conditions may be too large. Decreasing the boundary conditions would tend to decrease the modeled mixing ratios at all altitudes, leading to increased error at the surface. The initial conditions error is not significant because the model run is for two months but advection causes the influence of the initial conditions to diminish after several days.

Transport errors are also unlikely to contribute to this level of error in the near surface results. If transport error were large there would be similar errors for simulations of many other species but this is not the case [*Tang, et al.*, In Press].

Underestimated COS sources such as anoxic soils could also account for some of the error, but not to the extent required by the near surface errors. The 0.5 correction is equivalent to a source of the magnitude of the NPP-based COS plant uptake. It is unlikely that such a large source would have gone unnoticed during field measurements of COS. However, the source terms are likely to be larger than currently estimated because current source terms were calculated to balance the NPP-based plant uptake

instead of the larger GPP-based plant uptake [*Montzka, et al.*, In Press]. In other parts of the world where anoxic soils and wetlands are more prevalent, the revised source estimates will be more significant. Biomass burning is a possible missing source given that the forest fires in Alaska and Canada during the summer of 2004 were the largest on record. However, there are no observed enhancements of COS that coincide with the observed enhancements of the acetonitrile, a biomass burning tracer.

2.8 Conclusions

The top-down analysis of the GPP- and NPP-based parameterizations of COS plant uptake was completed using INTEX-NA observations and the STEM transport model. Comparison of the modeled NPP-based COS mixing ratios with observations indicates that the NPP-based plant uptake underestimates the magnitude of this sink. An analysis of the observations suggests that the primary relative uptake summarized in Sandoval-Soto et al. [2005] overestimates the relative uptake over North America by a factor of approximately 0.5, with potentially larger overestimates in the Midwest region. Comparison of the modeled GPP-based COS mixing ratios with observations also suggests that the Sandoval-Soto et al. [2005] relative uptake is overestimated by a factor of 0.5 to 0.6. Further, plant enclosure experiments and top-down analysis would help to improve the accuracy of the relative uptake estimates.

CHAPTER 3 PARTITIONING RESPIRATION AND GROSS PRIMARY PRODUCTION WITH CARBONYL SULFIDE OBSERVATIONS

3.1 Introduction

A primary objective of carbon cycle science is to understand the processes controlling surface fluxes of CO_2 so that prognostic carbon models can be coupled with climate models for predicting global change [*Denning, et al.*, 2005; *Wofsy and Harris*, 2002]. Biochemical processes controlling surface CO_2 fluxes can be studied in detail with observations at spatial scales of a single plant or field [e.g. Sandoval-Soto et al., 2005]. However, due to the heterogeneity of the land surface, larger scale observations are needed to provide information about the regional and global carbon fluxes. Atmospheric CO_2 observations from aircraft and tall towers are an ideal large scale observation because the CO_2 mixing ratios are influenced by the integral of regional surface fluxes across large temporal and spatial scales [*Bakwin, et al.*, 1998a; *Gerbig, et al.*, 2003a; 2003b; *Gloor, et al.*, 2001]. The CO_2 observations provide an integrated view because the air masses originating from the air near the heterogeneous landscape is mixed by atmospheric turbulence before it reaches the observation point.

Observations of atmospheric CO_2 from aircraft and tall towers provide an indirect measurement of the surface flux variability. For example, an increase in the observed mixing ratio should correspond to an increase in the surface flux that is upwind of the observation point. Because the transport mixing processes vary in space and time, a quantitative connection between the observation and the various upwind regions of influence can be complicated. The quantitative inference of the surface flux distribution based on the variations of the CO_2 mixing ratio observations can be obtained using inverse atmospheric transport approaches [*Enting*, 2002]. The inverse transport model

uses advection and turbulent diffusion data from meteorological models in order to convert the down-wind mixing ratios into up-wind surface fluxes.

While the atmospheric inversion approach integrates information in time and space, it also integrates information across different processes. The large variations in observed INTEX-NA CO_2 mixing ratios are primarily influenced by respiration and photosynthesis. During the INTEX-NA flights, the observations were made during the day when the photosynthesis flux is dominant. However, the observations were sensitive to surface fluxes over broad spatial and time scales so that both respiration (RES) and photosynthesis (GPP) influences were significant. Along the INTEX-NA flight paths, the mean ratio of modeled RES mixing ratios to modeled GPP mixing ratios was 0.8, indicating similar contributions from both processes.

The task of partitioning the component fluxes is an important science question given that the goal of carbon science is to gain an understanding of the processes and not only the net surface flux. One approach to this partitioning problem has been to add further constraints from a land surface model [*Gerbig, et al.*, 2006]. Atmospheric inversions have typically been formulated to recover optimal surface fluxes. However, in Gerbig et al. [2006], the atmospheric inversion model is coupled to a land surface model so that the optimization recovers parameters within the land surface model that are specific to GPP and RES. This optimization problem is reliant on sufficient observations and quantitative uncertainty estimates of the surface fluxes and transport processes. Although much work has been done to quantify the uncertainty, the optimization problem is under-constrained due to the limited availability of observations [*Matross, et al.*, 2006].

Another approach for the partitioning problem is to add additional observation constraints to the inversion approach that are tracers of either GPP or RES. Measurements of the stable carbon isotopes (^{12}C, ^{13}C) in atmospheric CO_2 samples provide information about the relative RES and GPP contributions because these processes will take-up and emit air with characteristic ratios of the isotopes [*Bowling, et*

al., 2001]. A similar approach is possible with oxygen isotopes (^{18}O, ^{16}O) in atmospheric CO_2 [*Farquhar, et al.*, 1993; *Francey and Tans*, 1987]. The stable isotope approach requires that one of the gross fluxes must dominate. However, atmospheric CO_2 observations from surface stations and aircraft platforms are often influenced by a mixture of both GPP and RES, limiting the applicability of these isotope methods.

An ideal observational constraint for the partitioning problem would involve a measurement that is sensitive to only GPP or only RES. In the previous chapter, the dominant flux for carbonyl sulfide (COS) was validated as a function of the GPP CO_2 fluxes. An atmospheric inversion for COS could then be formulated in order to optimize the GPP flux. An atmospheric inversion that simultaneously assimilates CO_2 and COS could provide optimal estimates of GPP and RES fluxes.

Limitations to this inversion approach are sources of error other than the GPP and RES CO_2 fluxes. Errors in modeled transport, boundary conditions and surface fluxes other than GPP and RES will also contribute to the CO_2 error. These other sources of error are also important to the COS model. In addition, the errors in the relative uptake term discussed in the previous chapter will also be a source of error for the COS model. In the previous chapter a revised estimate of the relative uptake was estimated in order to minimize the influence of this relative uptake error. In this chapter, the COS and CO_2 inversion will be developed for data along INTEX-NA flight segment in which the errors are very large and are unlikely to be due to boundary conditions or flux errors other than GPP and RES CO_2 fluxes.

The development of CO_2-only, COS-only, and CO_2-COS inversion models is presented in this chapter for the purpose of partitioning the CO_2 flux estimate into GPP and RES components. Background for the inverse modeling approach is presented in section 3.2. The methodology for optimizing GPP and RES fluxes with COS and CO_2 observations is presented in section 3.3. The results for the CO2-only, COS-only, and CO2-COS inversion are presented in sections 3.4, 3.5, and 3.6 respectively.

3.2 Background on STEM Inversion Model and Data Assimilation

A STEM inverse model has been developed using the STEM regional transport model and the four dimensional variational (4D-Var) assimilation technique for sensitivity studies and optimal recover of surface fluxes, initial conditions, and boundary conditions [*Carmichael, et al.*, 2003a; *Chai, et al.*, 2006a; *Sandu, et al.*, 2005]. For surface flux applications, the inversion model outputs a time-invariant scaling factor, $e_{x,y}$, for each surface grid cell. The scaling factor is a multiplicative correction factor for the initial estimates of the fluxes (F). The optimal estimates of the fluxes will be $e_{x,y}*F_{x,y}$. The initial and optimal estimates of the surface fluxes are also referred to as the prior and posterior fluxes, respectively.

The inversion could also be formulated with a time varying scaling factor. However, increasing the number of control variable will make the problem further under-constrained. A time-invariant scaling factor will extract information from the observations related to longer time scales which may be more useful than information at hourly scales from a high time resolution emission scaling factor.

The scaling factor values of *e* are chosen so that the model to observed mixing ratio error is minimized. The minimization function is as follows,

$$J = \sum_{i}^{n} u_i \left[M_i (e * F) - O_i \right]^2 \qquad 1$$

where J is the sum of the squares of the modeled to observed mixing ratio error, M_i is the modeled mixing ratio interpolated to the i^{th} observation time and location, O_i is the i^{th} observed mixing ratio, u_i is the uncertainty for the i^{th} mixing ratio (model and observed), and n is the total number of observations. This inversion problem can be thought of as an

optimization problem in which the scalar J is the cost to be minimized and *e* is the control variable and the transport model as the constraints. The uncertainty term, u_i, should incorporate uncertainty due to measurement error, representation error (difference between model grid cell and point observation), transport error due to simulated advection and turbulent diffusion, and error due to components in the observed mixing ratios that are not directly related to the surface fluxes that are being optimized (e.g. optimize GPP surface fluxes but the observations have fossil fuel source components).

The atmospheric inversion problem is under-constrained because there a few observations relative to the number of control variables or degrees of freedom. When the problem is under-constrained, there are many possible values of the scaling factors that could achieve the same minimization of the cost function. In order to reduce the number of possible solutions, additional observations or additional factors can be added to the cost function. The availability of observations is not sufficient to fully constrain the problem. For the flux inversion cost function it is typical to add factors that will minimize the difference between the scaling factors and 1. This is equivalent to minimizing the difference between the prior fluxes and the optimized fluxes and is based on a Bayesian justification. The cost function with this addition term is,

$$J = \sum_{i}^{n} u_i \left[M_i (e * F) - O_i \right]^2 + \sum_{x}^{X} \sum_{y}^{Y} p_{x,y} \left[e_{x,y} - 1 \right]^2 \qquad 2$$

where $p_{x,y}$ is the uncertainty for the prior flux estimates.

Another approach for reducing the number of possible solutions is by adding error covariance terms to the cost function so that errors are related between different species, times, and locations [*Gerbig, et al.*, 2003a; 2003b; *Lin and Gerbig*, 2005; *Michalak, et al.*, 2004; *Michalak, et al.*, 2005; *Palmer, et al.*, 2006]. The error covariance technique has also been applied in recent studies with the STEM 4D-Var model using multiple meteorology input to estimate the uncertainty due to transport error.

The typical approach for determining the values of the control variables that will minimize the cost function is to calculate the partial derivatives of the cost function with respect to the control variables and then use an iterative gradient search algorithm to converge on the optimal estimate. For the atmospheric inversion cost function in equations 1 and 2, the partial derivatives are difficult to calculate because the modeled mixing ratios in the cost function (M) are complicated implicit functions of the control variable (e). Calculating these partial derivatives would require repeated use of the chain rule.

The STEM inverse model implements a practical approach for calculating the partial derivatives through the use of the adjoint technique. The adjoint technique introduces Lagrange multiplier variables to the cost function and the constraints [*Thacker*, 1987]. The partial derivatives are calculated with the adjoint technique from computations that are very similar to running the STEM forward model twice.

The STEM inverse model follows the iterative technique described above. During each iteration, the adjoint model calculates the partial derivatives of the cost function and then a minimization algorithm estimates the optimal scaling factors as a function of the gradients. At the beginning of each algorithm, the adjoint model uses the scaling factors from the previous iteration to calculate the partial derivatives. The Quasi-Newton limited memory L-BFGS optimization routine is applied to search for the optimal scaling factors [*Zhu, et al.*, 1997].

3.3 Inversion Experimental

In this study, optimal scaling factors for the GPP and RES surface fluxes are estimated using the STEM inversion model and observed mixing ratios of CO_2 and COS from the INTEX-NA field campaign. The SiB estimates of GPP and RES surface fluxes

discussed in Chapter 2 are the prior CO_2 surface fluxes. The prior COS surface flux is estimated using the GPP parameterization as the product of the SiB GPP CO_2 flux, a fixed $[COS]/[CO_2]$ ratio of $1.1x10^{-6}$, and a fixed relative uptake of 1.5. The uncertainty in the fixed relative uptake term is discussed in the following sections.

Alternative formulations of the STEM 4D-Var model were applied to recover optimal surface flux scaling factors for the GPP and RES CO_2 fluxes. The six formulations are summarized in Table 6. A formal analysis of the mixing ratio uncertainties and the flux uncertainties are not yet available for estimating the uncertainty terms in the cost function (equation 2). For the inversion experiments presented here, the mixing ratio error (u_i) is assumed to be 1% and the flux error ($p_{x,y}$) is assumed to be 50%. These values are chosen simply to weight the observations much higher than the prior fluxes. The assumption of a 1% mixing ratio error is likely to underestimate the transport errors. The sensitivity of the inversion results to these uncertainty parameter values will be examined with multiple runs using modified uncertainty assumptions.

Table 6. Control variables and observations used in six alternative formulations of the STEM inverse model.

Inversion Formulation	Observations	Scaling Factor Control Variables
1	CO_2	GPP
2	CO_2	RES
3	COS	GPP
4	CO_2	GPP, RES
5	CO_2, COS	GPP
6	CO_2, COS	GPP, RES

The observation input for each of the inversion formulations depend on the control variable. The observation input data is the difference between the observation and all components other than the control variable components. For example, for the

GPP-only formulation 1 in Table 6, the input CO_2 data is a residual observation calculated as,

$$^{GPP}O = O - (^{RES}M + ^{FF}M + ^{OC}M + ^{BG}M) \quad (3)$$

where ^{GPP}O is the residual observation, O is the CO_2 observation, ^{RES}M is the modeled RES component, ^{FF}M is the modeled fossil fuel component, ^{OC}M is the ocean component, and ^{BG}M is the background (boundary condition) component.

These inversion experiments assimilate observations from the section of INTEX-NA flight 12 (July 25th) that passes over land. The July 25th flight was chosen because the influence of the surface sink is very strong. The CO_2 mixing ratio errors are very large and are likely to be due to errors in the GPP and RES surface fluxes because unrealistic adjustments in the fossil fuel and ocean fluxes would be required to correct the errors. This flight is also chosen because it does not have large errors due to the influence from large point sources of fossil fuel combustion as indicated by observations of CO, SO_2 and other combustion tracers. The three low altitude passes during flight 12 are shown in Figure 15. The flight proceeds from south to north, starting at 18 hr. GMT and finishing at 22 hr. GMT (12 EST to 16 EST). The three low altitude passes will be referred to in order of time with the first low altitude pass over Alabama, the second low altitude pass over West Virginia, and the third low altitude pass over New York.

The observed mixing ratio is the 1-minute averaged data set that merges the observation data for all measured species on the INTEX-NA DC8 flights (Figure 15). This merged data set allows for the comparison of CO_2 and COS observations. This averaging period also reduces the representation error. Based on the average speed of the DC8, the 1-minute averaging period provides 1 to 2 observations per model grid cell. The observation methodologies are discussed in section 2.4 (previous chapter) of this work.

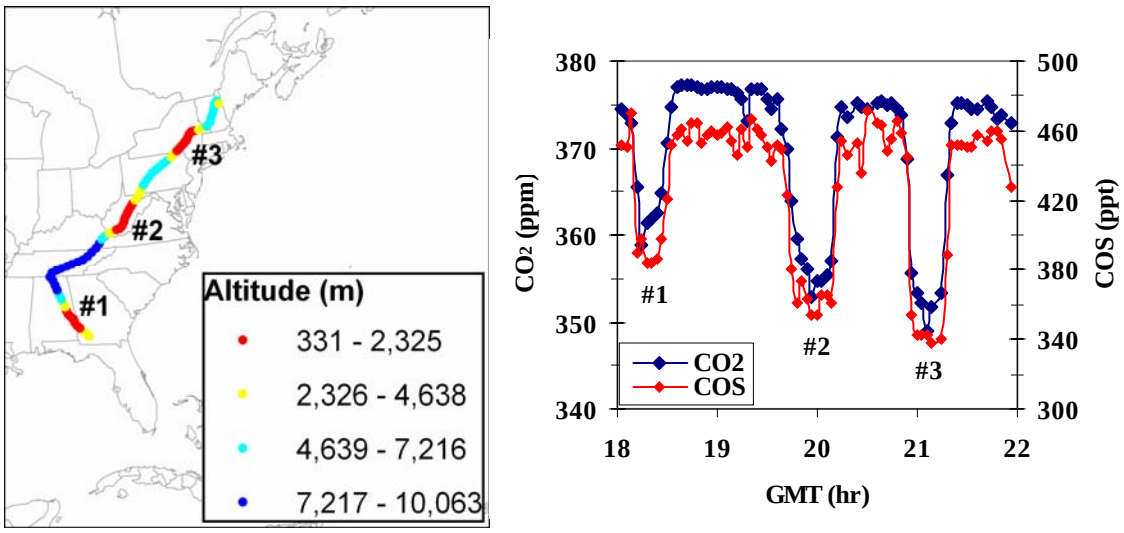

Figure 15. Altitude above surface level on flight path map (left) and time series of observed mixing ratios of CO_2 and COS (right) for the July 25th INTEX-NA DC8 flight. The successive low altitudes passes in time are marked #1, #2, and #3.

3.4 Single Species Inversions with CO_2 Observations

The model and observed mixing ratios are plotted as a time series along the flight 12 path in Figure 16. The contributions from GPP, RES, and fossil fuel surface fluxes are shown in the top plot. All three component mixing ratios increase with decreasing altitude as expected. The GPP and RES components have similar mixing ratio magnitudes (but opposite in sign) on the first two low altitude passes (over Alabama and West Virginia) with magnitudes of approximately 80 ppm on the first low altitude pass and 40 ppm on the second low altitude pass. On the third low altitude pass (over New York) the GPP component is approximately -20 ppm while the RES component is less than 5 ppm. For all three low altitude passes, the fossil fuel and NEE (GPP + RES) components are an order of magnitude lower than GPP. The fossil fuel component is 3

ppm, 2 ppm, and 1 ppm for the first, second, and third low altitude passes respectively. The NEE component is approximately 1 ppm, -10 ppm, and -7 ppm for the first, second, and third low altitude passes respectively. The contribution from the ocean component is less than 1 ppm (not shown). There is very little variability in the contribution from the boundary conditions with a mean of 374±0.4 ppm (not shown). Small changes in the RES and GPP fluxes will have a large influence on the modeled CO_2 mixing ratio while small changes in the fossil fuel and ocean fluxes will have very little effect on the modeled CO_2 mixing ratios.

The observed CO_2 mixing ratios along the flight path shown in Figure 16 (middle plot) indicate large uptake near the surface at each of the low altitude passes. The observed CO_2 decreases from the background mixing ratio by 15 ppm, 20 ppm, and 25 ppm during the first, second, and third low altitude passes respectively. While the observed drawdown gets larger with each consecutive low altitude pass, the absolute magnitudes of the modeled GPP and RES components got smaller with each consecutive pass. However the balance of these components (NEE) is larger for the second two low altitude passes. The total modeled mixing ratios show an increase in mixing ratio relative to the background value during the first low altitude pass due to the slightly positive NEE and small fossil fuel source. The modeled CO_2 mixing ratio decreases below the background mixing ratios during the second and third low altitude passes due to a negative NEE. For all cases, the error is positive during the low altitude passes (Figure 16 bottom plot) indicating that the GPP sinks are too small or the RES sources are too large. Unrealistic corrections to the fossil fuel and ocean components would be required to correct for the model to observed error. The error is most likely due to GPP or RES fluxes.

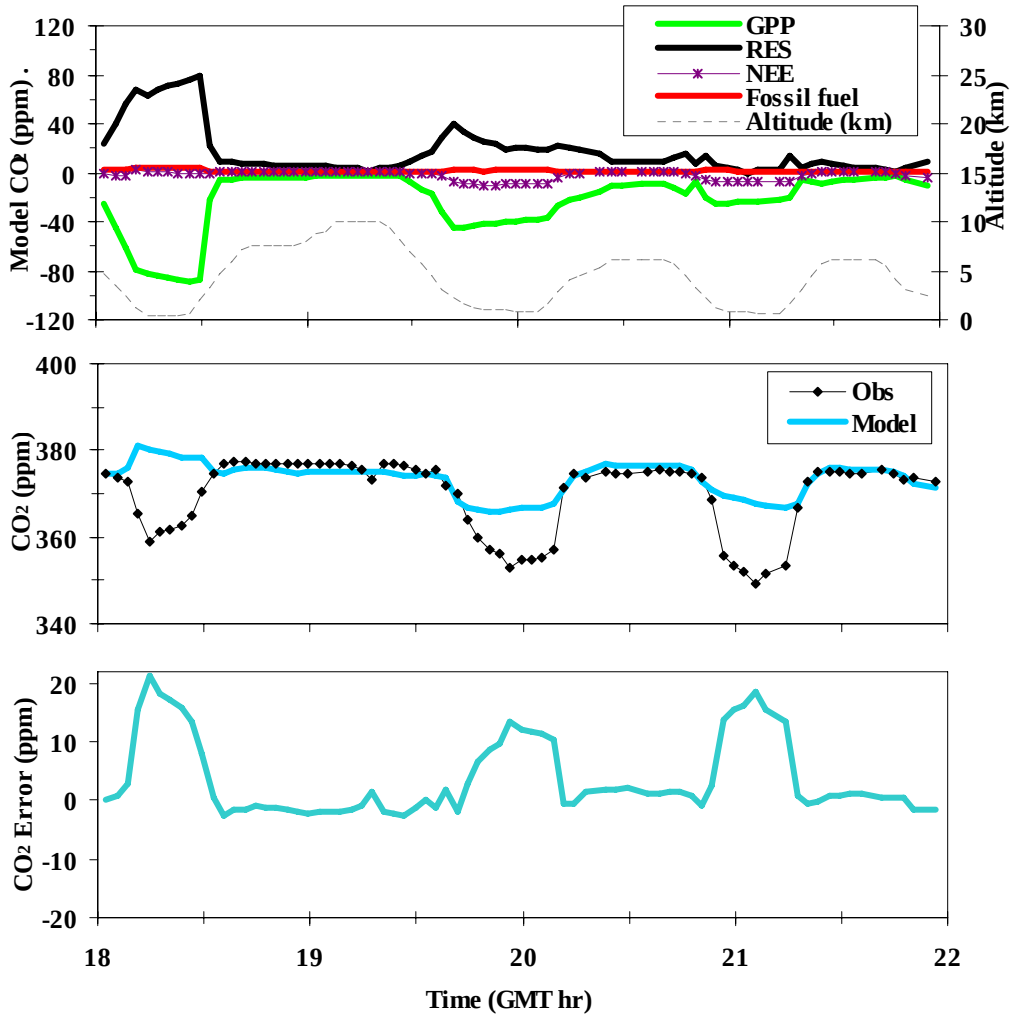

Figure 16. Time series of modeled CO_2 components mixing ratios (top), model and observed total mixing ratios (middle), and error (model – observed) (bottom) along the INTEX-NA DC8 flight 12 over the eastern U.S.

The first inversion formulation uses only CO_2 observations and only scaling factors for the GPP flux (no COS observations and no scaling factors for RES). In this case, the inversion model estimates scaling factors that minimize the mixing ratio error and minimize the difference between the scaling factors and 1. The GPP scaling factor output from the inversion run is shown in Figure 17. This map also shows the prior error as points along the flight path (mixing ratio error before inversion scaling factors are

applied). The scaling factors with the largest values are located at surface grid cells directly beneath and upwind of the three low altitude passes where the mixing ratio errors are largest. The first low altitude pass (southern portion of flight) is influenced by surface fluxes to the east of the observation locations, the second low altitude pass is influenced by surface fluxes to the northeast and the third low altitude pass is influence by fluxes to the north and northeast.

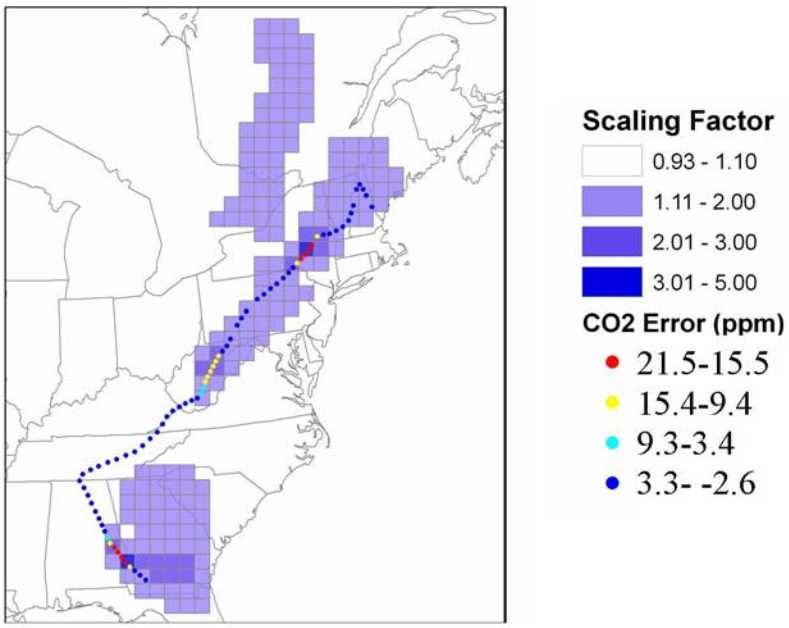

Figure 17. Scaling factors (shaded grid cells) for GPP fluxes based on assimilated CO_2 mixing ratios and along the INTEX-NA DC8 flight 12. The CO_2 mixing ratio errors resulting from the prior fluxes (scaling factor = 1) are shown by the colored dots.

The spatial extent and magnitude of the scaling factors for this inversion run depends heavily on the length of the simulation period (assimilation window). For short simulation periods (results not shown) the extent is very small and the scaling factors are very large. The opposite is true of longer assimilation windows. For example, for a 5

day assimilation period the maximum scaling factor is 3.5 and the spatial extent of the large factors extends beyond the 3 day assimilation shown in Figure 17. For the short periods, the extent is small because over a shorter time the influence of surface fluxes propagates a shorter distance. For this case, only the surface flux grids closest to the location of the errors will have any influence on the model mixing ratios. The scaling factors are large because with a smaller extent, larger fluxes are required to correct the same amount error. The dependence on the simulation window length could be removed by adding observations at different times but in similar locations. Another approach is to simultaneously optimize for initial conditions and surface flux scaling factors. However, for the purpose of providing a simple demonstration of the inversion formulations in Table 6 the short window length will be used.

The mixing ratios from observations, prior model (no scaling factor), and posterior model (optimized scaling factor) are shown in Figure 18. The posterior eliminates about 90% of the error associated with the mixing ratios (equation 1) and 50% of the combined mixing ratio and flux error (equation 2). The extent of the remaining error is largely a function of the uncertainty parameter inputs in equation 3. For example, increasing the flux uncertainty to 100% results in a posterior mixing ratio that removes 98% of the mixing ratio error (equation 1). This also results in an unrealistic spatial distribution of scaling factors.

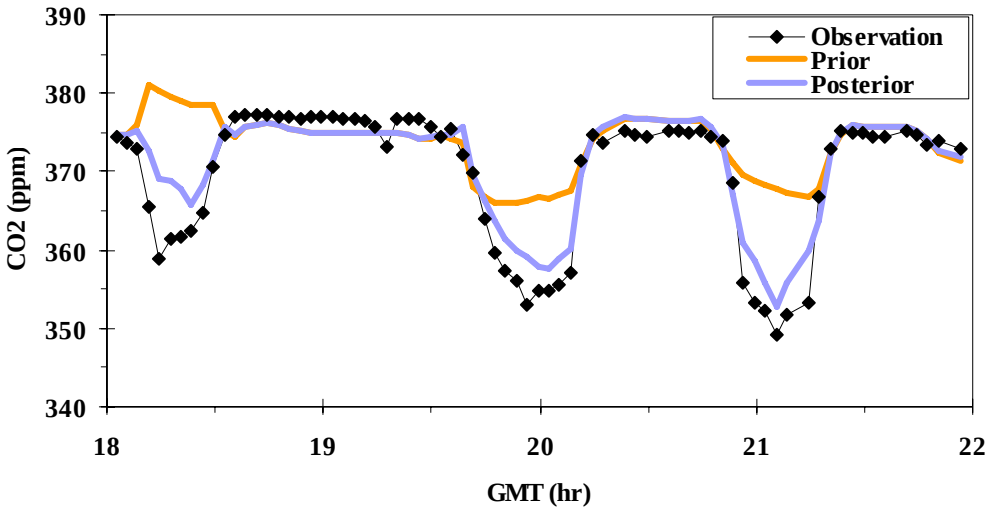

Figure 18. Time series of the observed, prior modeled, and posterior modeled CO_2 mixing ratios along the INTEX-NA DC8 flight 12 for assimilated CO_2 mixing ratios and optimized GPP fluxes.

For the next formulation of the inverse model, scaling factors are retrieved for RES instead of GPP. The same simulation window of 72 hour and observations from flight 12 are used. The scaling factors tend to be less than one because the RES component must be reduced to eliminate the positive mixing ratio error. The spatial distribution of the scaling factors is shown in Figure 19. The spatial variability of the RES scaling factors is similar to the distribution of GPP scaling factors from the GPP inversion experiment. This similarity occurs despite the differences between the diurnal variation of the RES and GPP fluxes. The GPP fluxes are large during the day and negligible during the night. The opposite is true of RES fluxes. This indicates that the observation points where the error occurs are influenced by fluxes over temporal ranges that extend beyond day time hours of the flights. This is also due to the fact that the scaling factors are time invariant so the optimization model is solving for trends in the surface fluxes on the order of the simulation length.

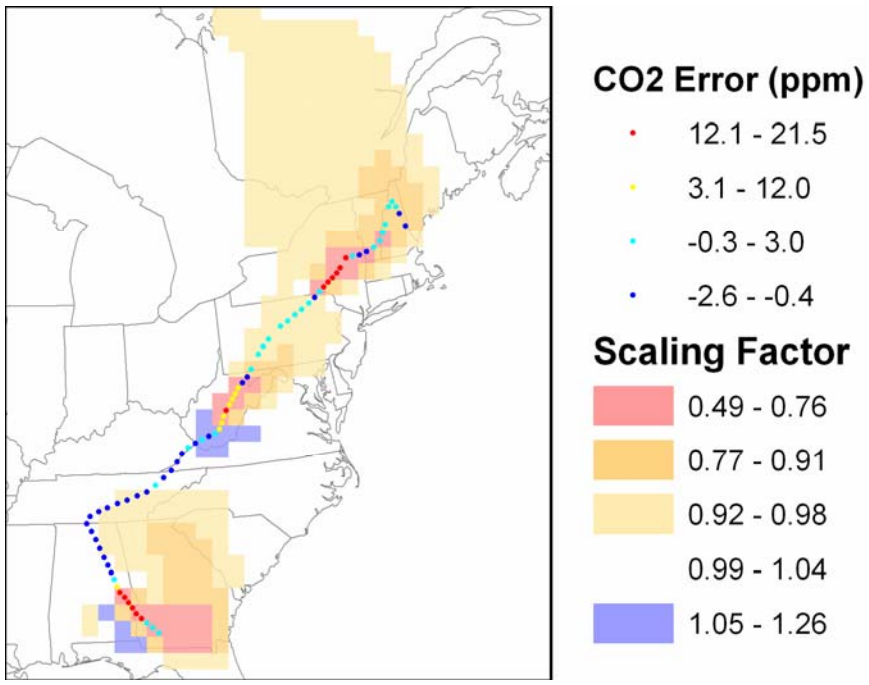

Figure 19. Scaling factors (shaded grid cells) for RES fluxes based on assimilated CO_2 mixing ratios and along the INTEX-NA DC8 flight 12. The CO_2 mixing ratio errors resulting from the prior fluxes (scaling factor = 1) are shown by the colored dots.

The reduction of the mixing ratio part of the cost function is approximately 90% for the RES inversion. This is approximately the same reductions as with the GPP formulation. The mixing ratios from observations, prior model (no scaling factor), and posterior model (optimized scaling factor) are shown for the RES inversion run in Figure 20. The posterior model to observation agreement is improved during the first two low altitude passes. However, at the third low altitude pass there is little improvement. This occurs because the prior RES mixing ratio component (Figure 16) at the third low altitude pass indicates only small RES mixing ratios. Reducing the RES mixing ratio at third low altitude pass can only correct for approximately half of the error. The cost associated with the flux (equation 2) is smaller with the RES inversion than with the GPP inversion.

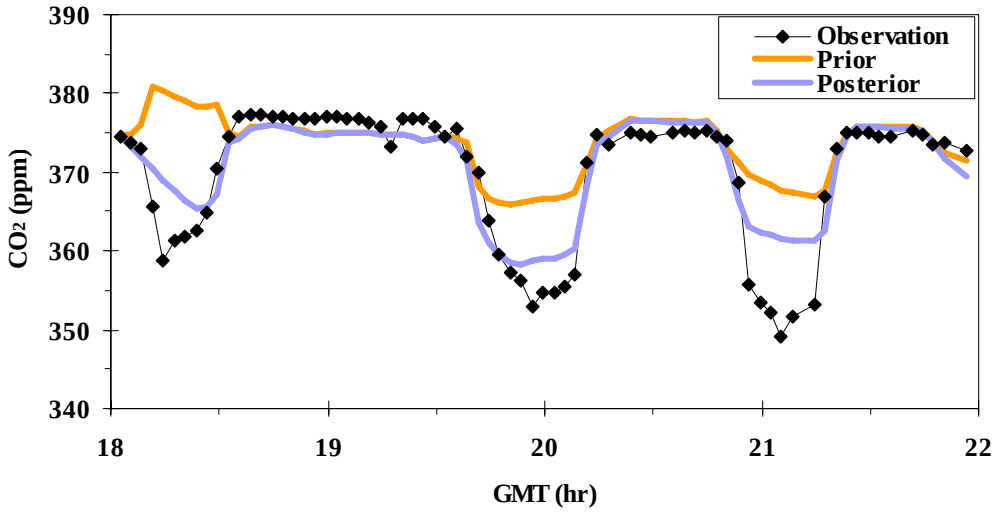

Figure 20. Time series of the observed, prior modeled, and posterior modeled CO_2 mixing ratios along the INTEX-NA DC8 flight 12 for assimilated CO_2 mixing ratios and optimized RES fluxes.

Another possible formulation of the inversion would be to use CO2 observations with scaling factors for RES and another set of scaling factors for GPP. In this approach there are two sets of control variables. However, this new inversion formulation would be unlikely to obtain improved results over the GPP-only and the RES-only cases. The GPP-only and RES-only inversions both obtained similar improvements in the cost function and similar scaling factors. There solution to this inversion problem is non-unique and using two sets of scaling factors will present a highly under constrained problem. In section 3.6 the simultaneous use of COS with CO_2 observations is presented as a means to further constrain the problem so that both RES and GPP scaling factors can be estimated.

3.5 Single Species Inversions with COS Observations

The modeled and observed time series of COS mixing ratios for flight 12 are shown in Figure 21. The contributions from the COS plant uptake sink (GPP), soil sink, ocean source, and anthropogenic source components are in the top plot. The GPP component is an order of magnitude larger than the other components. The COS GPP component has a similar pattern to the CO_2 GPP component. This is because the COS GPP flux is the CO_2 GPP flux times the ambient concentration ratio ($1.1x10^{-6}$) and a fixed relative uptake of 1.5. The soil sink component is approximately -13, -7, and -4 ppt for three consecutive low altitude passes. The anthropogenic and ocean components are always less than 2.5 ppt. Small changes in the GPP fluxes will have a large influence on the modeled COS mixing ratio while changes in the other flux components will have a much smaller influence on the modeled COS mixing ratios.

The observed COS mixing ratios along the flight path shown in Figure 21 (middle plot) indicate large uptake near the surface at each of the low altitude passes. The observed COS decreases below the background levels for each low altitude pass. The magnitude of the uptake grows with each consecutive pass from 67, 97, 124 ppt. This pattern was also the case for the CO_2 observations and results in a very strong correlation between the observed species ($r^2 = 0.95$) shown in Figure 22. The model COS GPP component follows the opposite trend by decreasing in magnitude for each consecutive low altitude pass. This results in an underestimate of the COS mixing ratio at the first low altitude pass and an overestimate at the second two low altitude passes. The magnitude of the errors is shown in the bottom plot of Figure 21 indicating errors of -50 ppt, 40 ppt, and 80 ppt for the consecutive low altitude passes. These errors are much larger than the soil sink component indicating that the GPP term is the likely source of error.

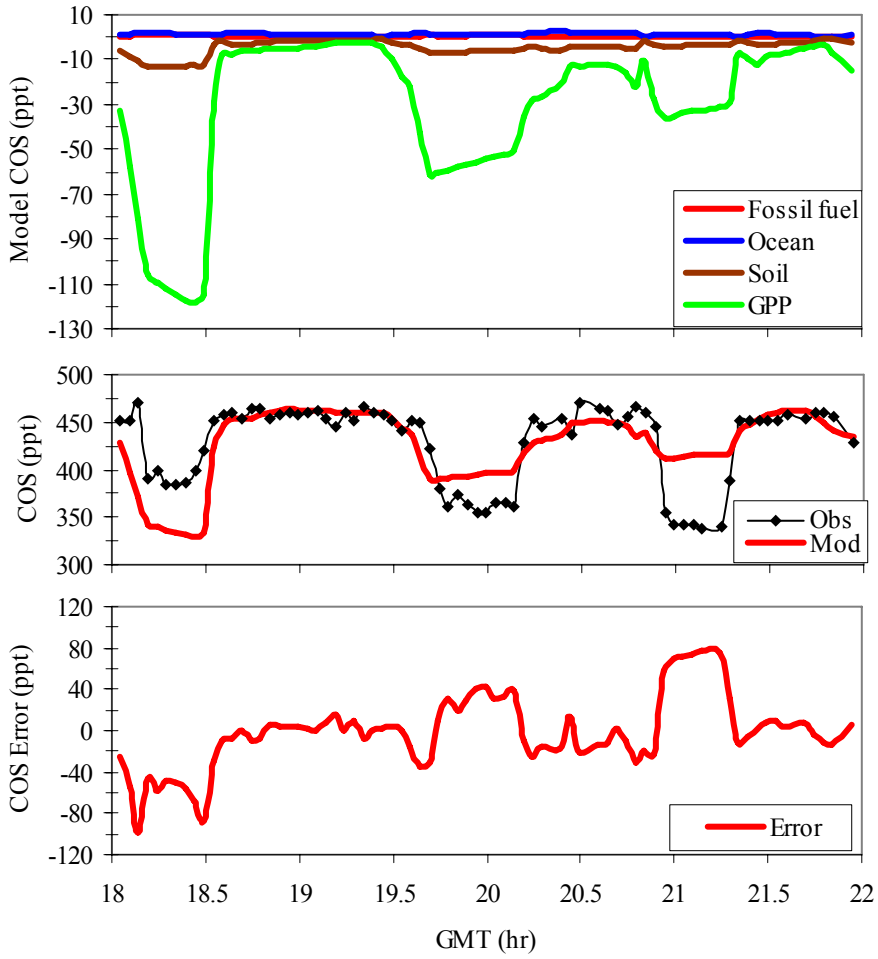

Figure 21. Time series of COS mixing ratios (ppt) along INTEX-NA DC8 flight 12. The top plot includes modeled component concentrations for GPP, soil, ocean, and fossil fuel fluxes. The middle plot compares total modeled COS with observed COS. The bottom plot is the error (modeled – observed).

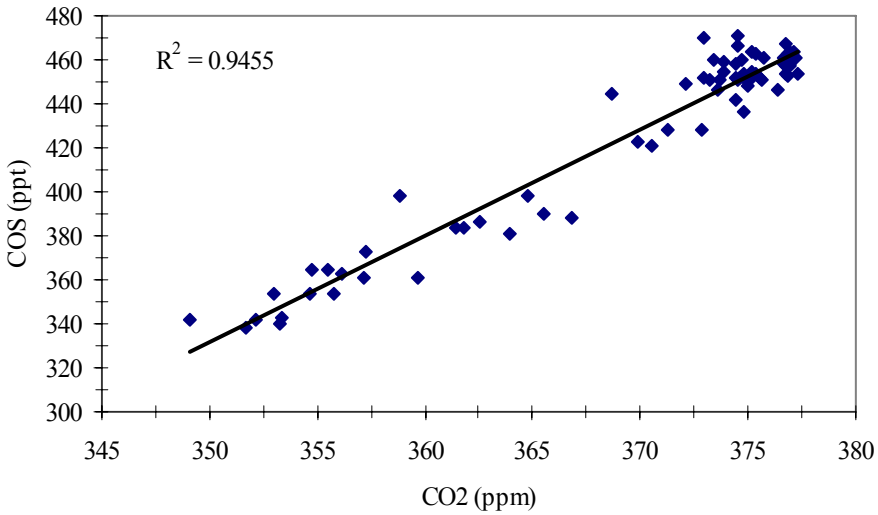

Figure 22. Observed CO_2 to COS along the INTEX-NA DC8 flight 12 over land.

The inversion model is applied with COS observations and GPP scaling factors as the control variable. The map of resulting scaling factors is shown in Figure 23. The GPP scaling factors are less than one upwind of the first low altitude in order to correct for the negative COS mixing ratio error (model < observed). Recall that GPP scaling factors were greater than one for the CO_2–only inversion in the previous section in order to correct for the positive CO_2 mixing ratio error (model > observed). This suggests that the net CO_2 error was due to RES and not GPP. At the next two low altitude passes the COS scaling factors are greater than one to correct for the positive COS mixing ratio error. These two low altitude passes had GPP scaling factors of a similar magnitude for the CO_2-only inversion.

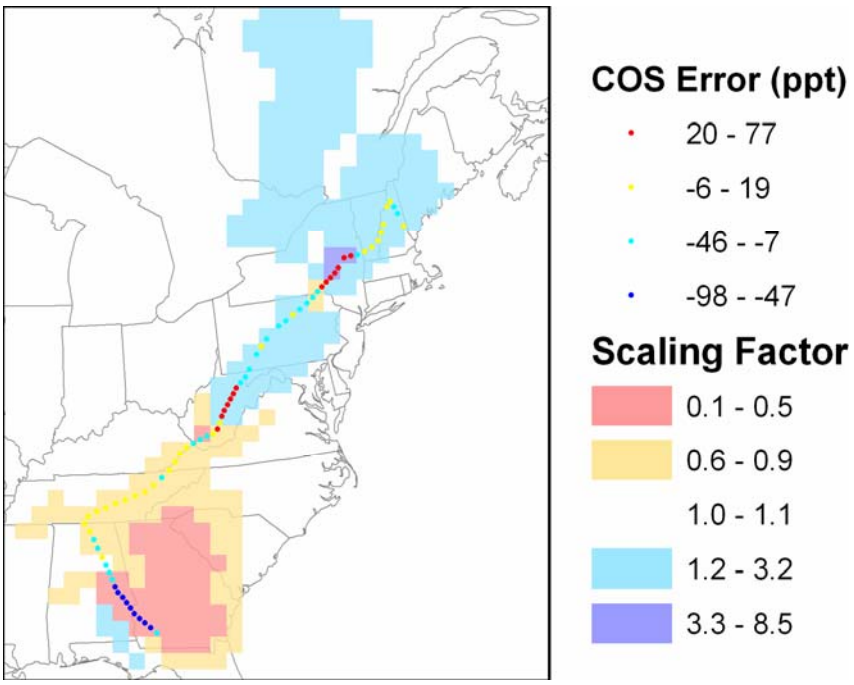

Figure 23. Scaling factors (shaded grid cells) for GPP fluxes based on assimilated COS mixing ratios and along the INTEX-NA DC8 flight 12. The COS mixing ratio errors resulting from the prior fluxes (scaling factor = 1) are shown by the colored dots.

The mixing ratio component of the cost function is reduced by 60% while the total cost is reduced by 45%. The time series of observed, prior, and posterior mixing ratios is shown in Figure 24. Excellent agreement between observations and posterior model results is obtained at the second two altitude passes but not at the first low altitude pass. The scaling factors directly upwind of the first low altitude pass vary from 0.1 to 0.2 which comes at a large cost to the prior part of the cost function. Further improvements at the first low altitude pass might be achieved by relaxing the flux uncertainty parameter in the cost function, increasing the simulation window, or by adding an initial condition constraint.

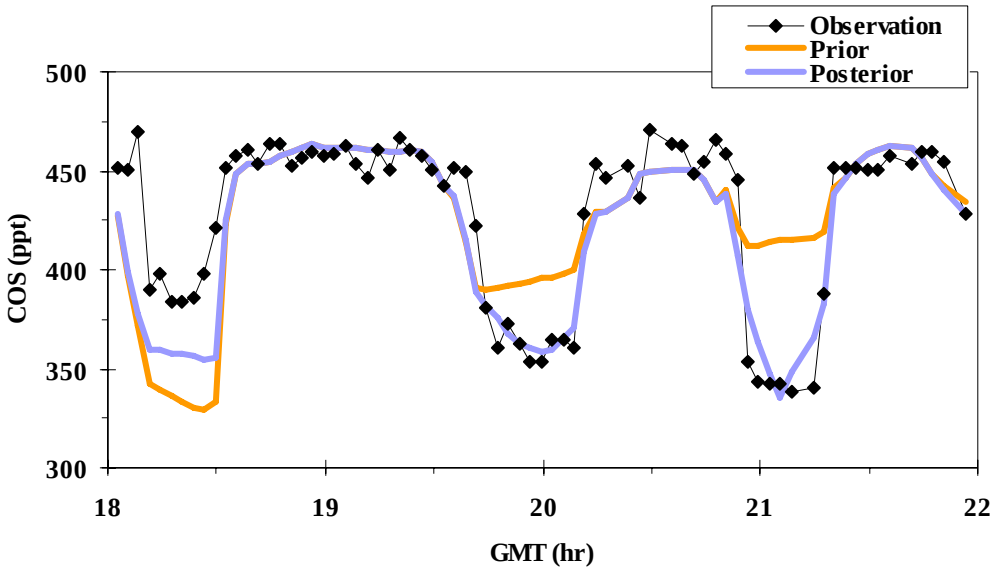

Figure 24. Time series of the observed, prior modeled, and posterior modeled COS mixing ratios along the INTEX-NA DC8 flight 12 for assimilated COS mixing ratios and optimized GPP fluxes.

3.6 Simultaneous Inversion of CO_2 and COS

It has been shown that the CO_2 errors on flight 12 could be corrected by applying scaling factors to GPP or to RES. Coupling the CO_2 and COS inversion may further constrain the inversion problem so that the GPP and RES corrections can be teased apart. In Figure 25, the time series of the COS errors (red) and CO_2 errors (blue) along the flight path are shown. As shown in sections 3.4 and 3.5, the COS errors are dominated by GPP errors while the CO_2 errors could be due to GPP or RES errors. The errors for COS and CO_2 are highly correlated for the second two low altitude passes ($r^2 = 0.8$). This suggests that the error for this segment of the flight path is due to GPP errors. At the first low altitude pass, the errors for COS and CO_2 are not correlated. This indicates that the errors

at this segment of the flight path are due to a mixture of GPP and RES errors. The simultaneous inversion of both species should allow for this error to be partitioned.

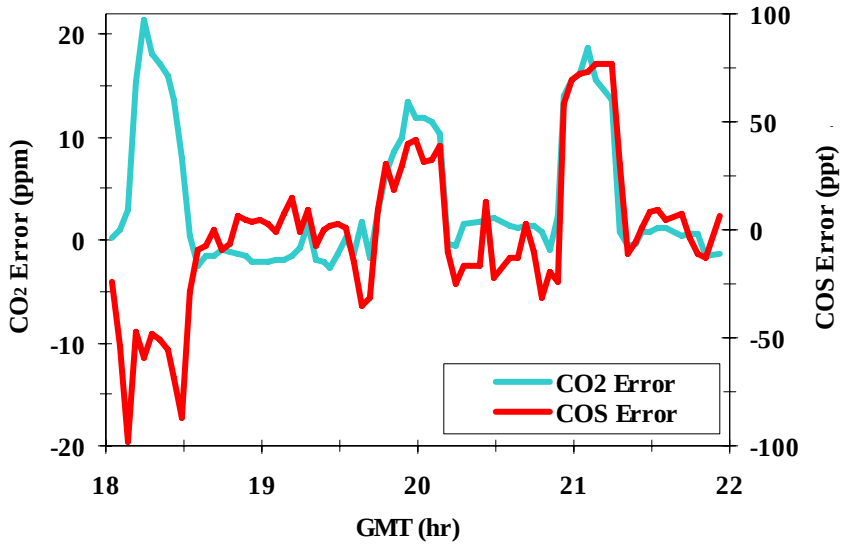

Figure 25. Time series of errors (model – observed) for CO2 (blue) and COS (red) along the INTEX-NA DC8 flight 12.

An inversion formulation that simultaneously assimilates CO_2 and COS observations with scaling factors for GPP is developed (no scaling factors for RES). The optimized GPP scaling factors resulting from this inversion are mapped in Figure 26. The GPP scaling factors resulting from this simultaneous CO_2-COS inversion at the first low altitude pass are approximately 0.7. This value is in between the GPP scaling factors for the CO_2-only inversion of approximately 3 and the COS-only GPP scaling factors of 0.2. The scaling factor of 0.7 represents a compromise between satisfying the positive CO_2 mixing ratio error by increasing the GPP sink and satisfying the negative COS mixing ratio error by decreasing the GPP sink. The GPP scaling factors resulting from the CO_2-COS inversion at the second two low altitude passes are fairly similar to the

CO_2-only and COS-only scaling factors because both the mixing ratio error is positive for CO_2 and COS at these low altitude passes.

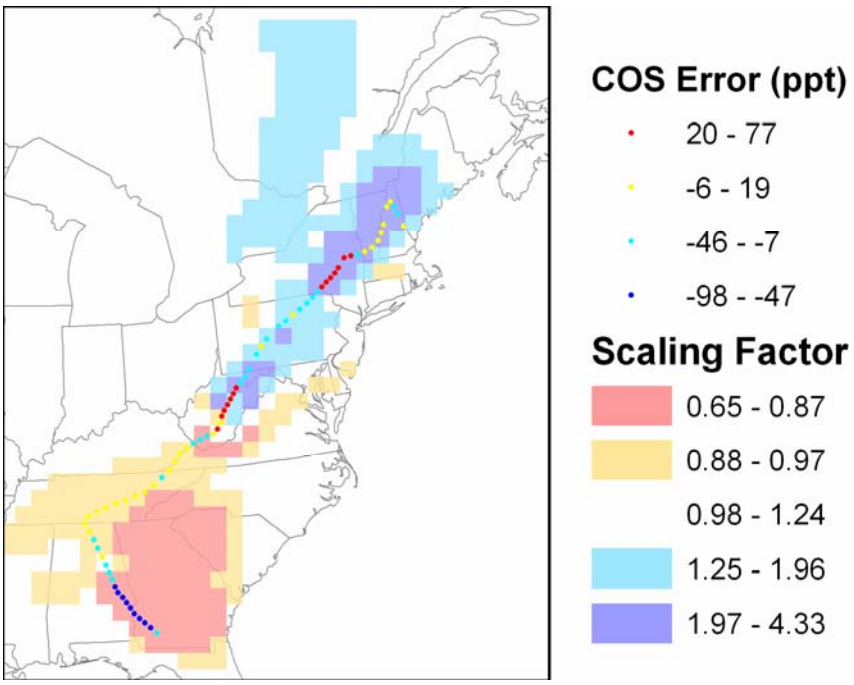

Figure 26. Scaling factors (shaded grid cells) for GPP fluxes based on assimilated CO_2 and COS mixing ratios along the INTEX-NA DC8 flight 12. The CO_2 mixing ratio errors resulting from the prior fluxes (scaling factor = 1) are shown by the colored dots.

The time series of observed, prior, and posterior mixing ratios for the CO_2-COS inversion is shown in Figure 27. The posterior errors increase for the first low altitude pass where the prior errors were opposite in sign for the two species. At the next two low altitude passes the errors are greatly reduced. However there is an over-correction for the CO_2 case and an under-correction for the COS case. The limitation of the CO_2/COS inversion results shown above may be due to the fact that some of the CO_2 mixing ratio error is due to the RES flux. Simultaneously assimilating for both species and both scaling factors could allow for improved results.

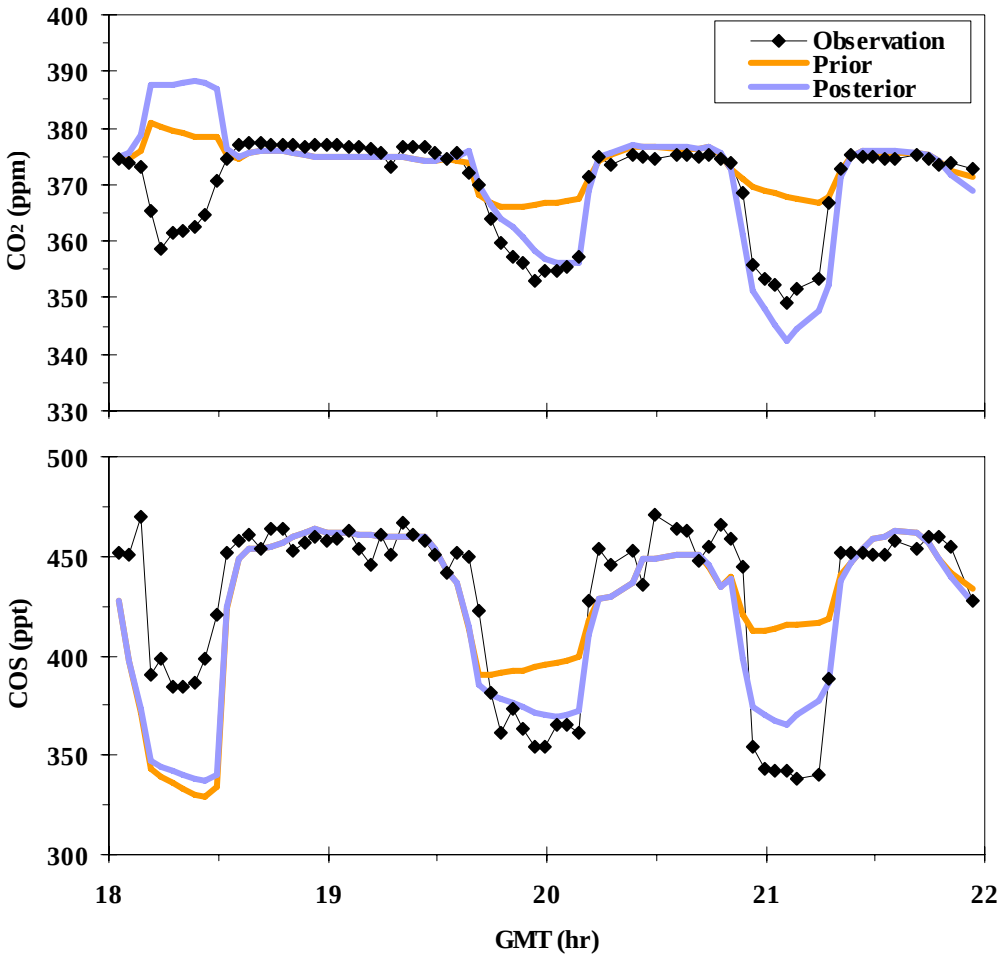

Figure 27. Time series of the observed, prior modeled, and posterior modeled CO_2 (top) and COS (bottom) mixing ratios along the INTEX-NA DC8 flight 12 for assimilated COS mixing ratios and optimized GPP fluxes.

3.7 Conclusions

This chapter developed a novel top-down approach for partitioning GPP and RES components of CO_2 by exploiting the relationship between COS plant uptake and CO2 GPP fluxes. The STEM inversion model was used to show that the inversion with only CO_2 observations could not easily distinguish between errors in the GPP and RES components. When the COS species is added to the inversion the GPP and RES surface fluxes are partitioned.

Further revisions and validation of this approach are needed. The inversion needs to be implemented with simultaneous optimization of RES and GPP scaling terms. The COS plant uptake parameterization is the product of the CO_2 GPP flux, the relative uptake, and the ratio of $[COS]/[CO_2]$. In the inversion framework presented here, the COS mixing ratio error is attributed to error in the CO_2 GPP flux term. However, the relative uptake term was shown in Chapter 2 to have significant uncertainty. Reducing the uncertainty in the relative uptake term will improve the accuracy of the partitioning of the GPP and RES CO_2 fluxes. Improved estimates of the relative uptake are likely to become available with further plant enclosure studies and development of mechanistic models of the relation between COS plant uptake and the CO_2 GPP sink.

Validation of the simultaneous inversion should also be completed using independent data sets. One approach would be to use the aircraft data in a CO_2-only inversion run and a CO_2/COS inversion run. The scaling factor from both approaches could be used to run the forward models for comparison with surface site data from NOAA GMD that is much more sensitive to the diurnal variations of GPP and RES fluxes.

CHAPTER 4 ANTHROPOGENIC CARBON DIOXIDE TRACER MODELS

4.1 Introduction

Top down studies, which infer CO_2 surface fluxes from observations of atmospheric CO_2 mixing ratio, provide strong evidence of a net sink of atmospheric CO_2 in the Northern Hemisphere terrestrial environments [*Bousquet, et al.*, 2000; *Enting, et al.*, 1995; *Fan, et al.*, 1998; *Gurney, et al.*, 2002; *Gurney, et al.*, 2003; *Gurney, et al.*, 2004; *Tans, et al.*, 1990]. An important step in many top down experiments is to apportion each CO_2 observation into source/sink components as follows,

$$^{obs}CO_2 = {}^{ff}CO_2 + {}^{oc}CO_2 + {}^{bio}CO_2 + {}^{bg}CO_2 + {}^{r}CO_2 \qquad (1)$$

here $^{obs}CO_2$ is the observed CO_2 mixing ratio, $^{ff}CO_2$ is the contribution to the observed mixing ratio due to fossil fuel emissions, $^{oc}CO_2$ is the contribution from the ocean surface flux, $^{bio}CO_2$ is the contribution from the seasonally-varying, annually-balanced biosphere flux, $^{bg}CO_2$ is the background contribution, and $^{r}CO_2$ is the residual mixing ratio from less well known sources and sinks such as deforestation, forest fires, biomass energy emissions, and interannual climate variability. The first three terms on the right side of equation 1 are considered to be relatively well known and are determined by running atmospheric transport models that are driven by surface flux estimates. The $^{r}CO_2$ term is the unknown that is inverted to obtain estimates of residual surface fluxes.

Estimates of the fossil fuel component, $^{ff}CO_2$, are typically obtained by driving atmospheric transport models with fossil fuel emission inventories. The widely used fossil fuel emission inventories have an annual, 1° by 1° resolution and are based on

statistics of energy consumption, emission factors, and population density [*Andres, et al.*, 1996; *Brenkert*, 1998; *Olivier, et al.*, 1996].

This CO_2 emissions inventory resolution may be appropriate for inversions of annual fluxes at global scales. However, the emissions resolution could cause large biases for regional scale carbon inversion. Regional scale inversions have spatial resolution of 10^2 to 10^6 km^2 and sub-annual temporal resolution. The seasonal variation of U.S. fossil fuel emissions has an amplitude of 30% [*Blasing, et al.*, 2003] and diurnal variation is likely caused by lighting, heating and industrial energy consumption. Side by side comparisons of monthly inversions driven by an annual scale fossil fuel inventory and a hypothetical seasonal varying inventory resulted in retrieved fluxes that had up to 50% differences [*Gurney, et al.*, 2005]. In addition to the error due to resolution, there are absolute errors in the inventories that must be considered in regional inversions [*Levin, et al.*, 2003].

In order to address the need for improved $^{ff}CO_2$ estimates, the use of observed anthropogenic tracers has been proposed [*Wofsy and Harris*, 2002]. The development of such methods to apply tracers to predict $^{ff}CO_2$ could allow for more accurate top down studies. This approach could also provide a means for validating fossil fuel emission inventories and carbon trading agreements.

Studies of the effectiveness of using observations of anthropogenic tracers to estimate $^{ff}CO_2$ indicate promise as well as concerns. Measurement of radiocarbon ($^{14}CO_2$) provide the most accurate estimates of $^{ff}CO_2$ but are currently sparse due to complexity and cost, and not yet possible at an hourly resolution [*Levin, et al.*, 1989; *Turnbull, et al.*, 2006; *Zondervan and Meijer*, 1996]. Sulfur hexafluoride, SF_6, which is emitted at industrial sources and electric power stations has been shown to yield large errors in $^{ff}CO_2$ [*Turnbull, et al.*, 2006], and thus is a poor choice for this approach.

This paper focuses on the use of carbon monoxide (CO) as an anthropogenic tracer for two reasons: (1) CO is widely measured at high time resolution and (2) the CO

tracer approach has been used to estimate ${}^{ff}CO_2$ in several top down studies. The CO approach has been applied as,

$$ {}^{ff}CO_2 = ({}^{obs}CO - {}^{bg}CO) / R \qquad (2) $$

here ^{obs}CO is the observed CO mixing ratio, ^{bg}CO is the background CO mixing ratio, and R is a ratio relating the CO offset to ${}^{ff}CO_2$.

Previous work applied the CO approach to hourly tower observations at 30 meters, in Harvard Forest [*Potosnak, et al.*, 1999]. A linear model was fit to the data leading to R values of 12.5-14.2 moles CO/ 1000 moles CO_2 in winter and 20-28 mol CO/ 1000 mol CO_2 in the summer, with ${}^{ff}CO_2$ of 4-5 ppm in winter and 2-3 ppm in summer. Other studies have assumed a fixed ratio, R, of 20 mol CO/ 1000 mol CO_2, based on ratios from Potosnak et al. (1999) and ratios from total annual U.S. emissions [*Bakwin, et al.*, 2004; *Bakwin, et al.*, 1998b]. More recently, the CO approach has been applied by estimating R and ^{bg}CO, and reactive chemistry using atmospheric transport models driven by emission inventories of CO and CO_2 [*Gerbig, et al.*, 2003b; *Lin, et al.*, 2004].

The major classes of potential error in the CO tracer method include: (1) errors in R; and (2) neglecting the non-anthropogenic sources and sinks of CO that influence the CO observation such as forest fires, partial oxidation of VOC's, and the reaction of OH and CO. Gerbig et al. (2003) accounted for non-anthropogenic CO for the COBRA campaign with a simple approach based on climatological values of OH and an assumption that forest fire and fossil fuel components were spatially separated. These results indicate that omitting OH oxidation would yield biased results. This analysis was extended by taking advantage of observed tracers and advanced photochemistry models to estimate the non-anthropogenic CO influences for CO observation where the forest fire and chemical influences are collocated. Sensitivity of ${}^{ff}CO_2$ to the ratio R is reported by comparing several different methods for calculating R. It should be noted that this work does not comprehensively consider the uncertainty in R as a result of potentially large

errors in source inventories, transport, chemistry, and the different disaggregation methods for CO and CO_2 inventories. The comprehensive study of the inventory ratios of CO:CO_2 requires either a bottom up study of the errors in the inventories, or a top down method using the $^{14}CO_2$ method [*Turnbull, et al.*, 2006].

The objective of our study is to estimate several of the more significant components of uncertainty in the CO tracer method due to forest fires and photochemistry contributions to the CO observations. These uncertainty components may be used to help explain absolute errors in the CO method found from comparison of CO and $^{14}CO_2$-based estimates of $^{ff}CO_2$. A revised CO method was presented that may better account for these contributions to CO and a limited comparison of our CO method uncertainty estimates with absolute error estimates from a study of $^{14}CO_2$ by the NOAA Global Monitoring Division (GMD) [*Turnbull, et al.*, 2006]. The results of this chapter are published [*Campbell, et al.*, 2007].

Atmospheric trace gas observations were taken from the International Consortium for Atmospheric Research on Transport and Transformation (ICARTT) field experiment conducted in the summer of 2004 over North America. The ICARTT observations are an ideal data set for our application for two reasons: (1) the data set includes tracers of many surface fluxes and (2) the observations cover portions of North America where future CO_2 tower observatories are planned. The STEM-2K3 regional air quality model and its adjoint [*Carmichael, et al.*, 2003b; *Sandu, et al.*, 2005; *Tang, et al.*, 2004] are applied with the SAPRC-99 chemical mechanism (94 species, 235 chemical reactions, 30 photolytic reactions). Much of the observed and modeled data presented in this study are available online (http://www-air.larc.nasa.gov/missions/intexna/dataaccess.htm).

4.2 Regional Air Quality Model and Emissions

The STEM-2K3 regional air quality model and its adjoint are used in this work. The model employs the SAPRC99 chemical mechanism [*Carter*, 2000], the SCAPE II aerosol thermodynamics module, and an on-line photolysis solver [*Tang, et al.*, 2003]. The photolysis reactions are particularly important to CO mixing ratios because photolysis is the main natural source of the OH radical. The OH radical is the primary oxidizing agent for CO and other reduced carbon trace gases (non-methane hydrocarbons) that are oxidized to CO. The contribution to CO_2 from the oxidation of hydrocarbons is currently not accounted for in the analysis.

An adjoint model to STEM-2K3 has been developed for sensitivity studies and optimal estimation of model parameters such as emissions and initial conditions [*Chai, et al.*, 2006b; *Daescu and Carmichael*, 2003; *Hakami, et al.*, 2005; *Sandu, et al.*, 2005]. The adjoint analysis was applied to obtain quantitative estimates of the influence regions for observation points along the ICARTT flight paths. A perturbation of the mixing ratio at the observation location, the receptor, is propagated backward in time to determine the sensitivities of the target with respect to the mixing ratios in each grid cell at previous time steps. The resulting sensitivity value is,

$$\varphi(x,y,z,t) = \frac{\partial CO_2^{\text{receptor}}}{\partial CO_2^{x,y,z,t}} \tag{3}$$

The time-averaged, column maximum values of the adjoint forcing term, φ, are computed to provide a map of the influence region as in Sandu et al. (2005).

The input meteorology fields are from the NCAR/PSU MM5 mesoscale meteorological model, driven by NCEP FNL (Final Global Data Assimilation System) 1°×1° analyzed data. Grid nudging was performed every 6 hours, and re-initialization with FNL data took place every 72 hours. The cloud scheme of Grell et al. (1994) was

chosen for the physical parameterization, and the MRF scheme [*Hong and Pan*, 1996] was employed for PBL parameterization. The MM5 simulation was run on a 60km Lambert Conformal North American domain. The 21 sigma layers extend from the surface to 100 hPa.

The time varying boundary conditions for CO_2 tracers of the biosphere, ocean, and fossil fuel fluxes are provided by the TM5 global chemical transport model [*Peters, et al.*, 2004]. The TM5 runs are on a 6° by 4° grid and are driven by ECMWF meteorological fields and emissions from the TransCom Continuous Experiment [*Law, et al.*, 2005]. Boundary conditions for CO, O_3, and other trace gases are provided by the MOZART-NCAR global transport model with a 2.8° horizontal resolution and MOPITT satellite derived forest fire emissions [*Pfister, et al.*, 2005]. Model results for CO_2 are in units of ppm-molar.

Within the model domain, surface fluxes for CO_2 are from the TransCom Continuous Experiment including 1° hourly biogenic fluxes from the Simple Biosphere Model for 2003 [*Baker, et al.*, 2003], 1° monthly ocean fluxes for 2000 [*Takahashi, et al.*, 1999], and 1° annual fossil fuel emissions for 1995 [*Brenkert*, 1998]. The fossil fuel emission to 2004 were scaled using a least squares fit to U.S. annual emissions data from 1997 to 2003 [*Blasing, et al.*, 2004]. The annual 2004 fossil fuel emissions were scaled to summer emissions based on the U.S. annual cycle with an amplitude of 30% [*Blasing, et al.*, 2003]. The interannual factor (1.15) and seasonal factor (0.86) approximately offset each other.

Anthropogenic emissions of CO, O_3, SO_2, NH_3, NO_x, and reduced carbon species (VOC's) are from the U.S. EPA National Emission Inventory (NEI) for 2001. These gridded, 4 km, hourly emissions include mobile, point, area, and non-road mobile sources. Reporting CO_2 emissions is voluntary in the U.S., and the EPA NEI does not include CO_2. Biogenic emissions of VOC's were estimated by driving the Biogenic Emission Inventory System 2 [*Geron, et al.*, 1994] with the meteorological output from

our MM5 runs. The effects of the different scales for these emissions are minimized by averaging to our 60 km model grid. However the possibility of introducing error in the CO:CO_2 emission ratio exists due to the interpolation of the CO_2 emissions onto the 60 km grid.

Local LPS emissions data were obtained from the U.S. EPA Clean Air Markets program (http://cfpub.epa.gov/gdm/). The emissions data included hourly, facility level emissions for 2004.

4.3 ICARTT Observations

Observations of CO_2, CO, and other trace gases were taken from the NASA DC-8 during the ICARTT field campaign in the summer of 2004. Measurements of atmospheric CO_2 (±0.25 ppm-molar uncertainty) and CO (±2% uncertainty) were obtained with a modified Li-Cor model 6252 nondispersive infrared analyzer and the Differential Absorption of CO Measurement (DACOM) instrument [*Sachse, et al.*, 1987], respectively. In-flight calibrations of CO_2 were performed every 15 minutes with standards traceable to the WMO Central Laboratory at NOAA GMD [*Vay, et al.*, 2003]. Additional grab samples of CO were analyzed at U.C. Irvine using a gas chromatograph (HP 5890) equipped with a flame ionization detector and a 3 m molecular sieve column [*Barletta, et al.*, 2002]. These CO measurements were calibrated using working standards (run every four samples) and using a gravimetrically prepared CO standard from NIST.

A comprehensive set of complementary trace gas measurements was also collected during ICARTT. Acetonitrile observations (CH_3CN, ±20% uncertainty) have been shown to be a tracer of forest fires [*Lobert, et al.*, 1991] and SO_2 an LPS tracer. Acetonitrile observations were taken with a modified gas chromatographic (GC) instrument that had previously been used to measure PAN and oxygenated organics

[*Singh, et al.*, 2003]. SO_2 was measured by chemical ionization mass spectrometry (±9% uncertainty) [*Huey, et al.*, 2004].

The observations of $^{14}CO_2$ (±1.6-2.6% uncertainty), CO_2, and CO were made during the summer of 2004 in New England by NOAA GMD [*Turnbull, et al.*, 2006]. These measurements were taken in the boundary layer and free troposphere at locations in Harvard Forest, Massachusetts (42º32'N, 72º10'W) and Portsmouth, New Hampshire (42º57'N, 72º37'W). Details of the extraction and accelerator mass spectrometry methods are in Turnbull et al. (2006).

4.4 CO Tracer Methodology

In this study, 4 variations of the CO tracer method were applied to estimate $^{ff}CO_2$ at observation points along the ICARTT flight paths. The first two approaches are the static methods [*Bakwin, et al.*, 2004; *Bakwin, et al.*, 1998b] that use a constant R value of 20. The basic static method is formulated as,

$$^{ff}CO_2 = (^{obs}CO - {}^{obs,bg}CO) / 20 \quad (4)$$

where $^{obs,bg}CO$ is the 20th percentile of the observed CO [*Potosnak, et al.*, 1999]. When this leads to negative values of the CO offset, the CO offset value was assumed to be zero to avoid negative contributions to $^{ff}CO_2$. A revised static method was applied to analyze the uncertainty due to non-anthropogenic influences as follows,

$$^{ff}CO_2 = (^{obs}CO - {}^{obs,bg}CO - {}^{chem}CO - {}^{bb}CO) / 20 \quad (5)$$

where ^{chem}CO is the net source of CO from the combined effects of OH oxidation sinks and VOC oxidation source, and ^{bb}CO is the biomass burning source component (described below).

The other two approaches are the model methods [*Gerbig, et al.*, 2003b; *Lin, et al.*, 2004] which estimate the ratio R by transporting emission inventory fluxes with an

atmospheric model. The model CO approaches can also be thought of as scaling the modeled fossil fuel CO_2 by the ratio of the observed to modeled fossil fuel CO. The basic model approach is formulated as

$$ {}^{ff}CO_2 = ({}^{obs}CO - {}^{\mathrm{mod},bg}CO) \Big/ \left(\frac{{}^{ff,\mathrm{mod}}CO}{{}^{ff,\mathrm{mod}}CO_2} \right) \tag{6} $$

where ${}^{ff,\mathrm{mod}}CO_2$ and ${}^{ff,\mathrm{mod}}CO$ are the mixing ratios resulting from driving the tracer model with fossil fuel inventories for CO_2 and CO respectively, and ${}^{\mathrm{mod},bg}CO$ is the mixing ratio resulting from driving the tracer model with only the boundary conditions (no emissions, no forest fire tracer). These model runs have no chemical reactions.

The revised model approach accounts for the non-anthropogenic CO influence as follows,

$$ {}^{ff}CO_2 = \left({}^{obs}CO - {}^{\mathrm{mod},bg}CO - {}^{chem}CO - {}^{bb}CO \right) \Big/ \left(\frac{{}^{ff,\mathrm{mod}}CO}{{}^{ff,\mathrm{mod}}CO_2} \right) \tag{7} $$

Note that the model approaches (equation 6 and 7) do not include any net chemistry effects on ${}^{ff,\mathrm{mod}}CO$.

The different methods in equation 4, 5, 6, and 7 are referred to as the static, revised static, model, and revised model methods, respectively. These CO methods are compared with the inventory method in which the ${}^{ff}CO_2$ is estimated by driving the atmospheric transport model with emissions inventories.

The overall chemistry mixing ratios are calculated as,

$$ {}^{chem}CO = {}^{mod}CO - {}^{tracer}CO \tag{8} $$

where ${}^{\mathrm{mod}}CO$ is the full chemistry model result and ${}^{\mathrm{tracer}}CO$ is the tracer model result (no chemistry). The chemistry values, ${}^{\mathrm{chem}}CO$, are the combination of the OH sink and the VOC source of CO,

$$ {}^{chem}CO = {}^{OH}CO + {}^{VOC}CO \tag{9} $$

where ^{VOC}CO is the VOC source of CO and ^{OH}CO is the OH sink of CO. The ^{VOC}CO source is estimated as the difference between the full chemistry model run and a full chemistry model run without VOC species in the emissions,

$$^{VOC}CO = {}^{mod}CO - {}^{no\ voc}CO \tag{10}$$

where $^{no\ voc}CO$ is the CO prediction from a full chemistry CO model run with anthropogenic and biogenic VOC emissions removed from the surface flux. VOC species mixing ratios have been verified with ICARTT DC-8 and WP-3 measurements.

The biomass burning component is an important contributor to CO during the observation period. Significant forest fire emissions occurred outside of the model domain in Canada and Alaska. These forest fires are the largest on record for Alaska. In contrast to the observed data from Gerbig et al. (2003), the ICARTT data encountered collocated forest fire and fossil fuel CO. In order to use CO as a fossil fuel tracer, the biomass burning CO component must be estimated and subtracted from the CO observation.

Outside of forest fire plumes, the model runs driven by MOZART forest fire CO boundary conditions were used to provide a modeled biomass burning estimate, $^{mod,bb}CO$. For concentrated forest fire plumes (acetonitrile > 0.28 ppbv), the modeled forest fire CO greatly underestimates biomass burning CO. Therefore, the modeled forest fire CO is used when acetonitrile is less than 0.28 ppbv and a regression-based CO estimate is used when acetonitrile is greater than 0.28 ppbv,

$$^{bb}CO = {}^{mod,bb}CO, \qquad \text{acetonitrile} < 0.28 \text{ ppbv} \tag{11}$$

$$^{bb}CO = \alpha \cdot acetonitrile + \beta, \qquad \text{acetonitrile} \geq 0.28 \text{ ppbv} \tag{12}$$

where $^{mod,bb}CO$ is the modeled forest fire CO, α and β are the slope and intercept terms from the linear regression. The linear regression parameters are obtained by relating observed acetonitrile to estimated biomass burning CO, $^{obs,bb}CO$, where

$$^{obs,bb}CO = {}^{obs}CO - ({}^{mod}CO - {}^{mod,bb}CO) \tag{13}$$

The observed acetonitrile peaks were verified to be forest fire influenced and not anthropogenic by inspecting values of observed CH_4, NO_2, and SO_2.

During one interception of a power plant plume (large point source, or LPS), the SO_2 observations are tested as an alternative tracer to CO. For LPS plumes, the CO approach may underestimate $^{ff}CO_2$ when the true ratio of anthropogenic CO to CO_2 is less than the fixed (R = 20) or modeled (R = $^{ff,mod}CO$ / $^{ff,mod}CO_2$) ratios. The SO_2 based $^{ff}CO_2$ estimates are obtained by dividing observed SO_2 by the ratio of anthropogenic emissions of SO_2 to CO_2 for power plants within the influence region of the observation. The LPS emissions ratios are estimated with emissions data from the U.S. EPA's Clean Air Markets [*EPA*, 2006].

4.5 Overview of Observed and Model Results

Observations and model performance were analyzed with a case study of the DC-8 flight during the day on July 20, 2004. This flight encountered a variety of important features for testing the CO method including urban pollution, LPS's, and regional forest fire plumes. In Figure 28, the exaggerated altitude of the flight (height of bars) is shown along with the 3 minute averaged (~30 km) CO_2 mixing ratios (color of bars). The low altitude segments of the flight pass over land cover that is primarily cropland in the Midwestern U.S. and forest in the Southeast. The low CO_2 mixing ratios near the surface result from the active summer biosphere in these regions.

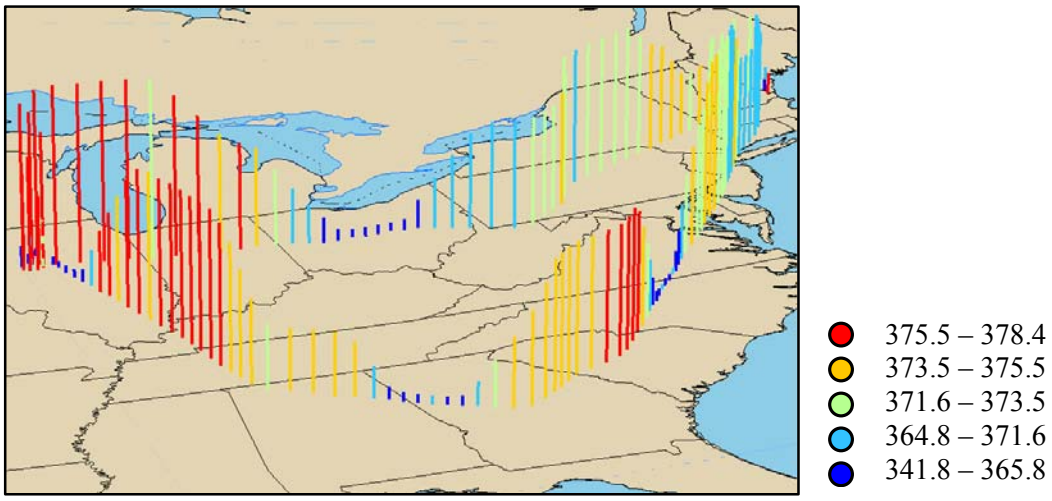

Figure 28. NASA DC-8 flight on July 20, 2004. Heights of the bars are exaggerated altitude of flight path. Color is observed CO_2 (ppm) with color scheme by natural break (Jenks) method.

Observation and model results from the July 20th flight are shown in the time series in Figure 29. In **Error! Reference source not found.**a, the CO_2 measurements are plotted along with the model results interpolated from the 60 km model domain. The model captures the general trend in CO_2 variation but misses the depth of the biosphere sink and the low altitude CO_2 enhancements. The low altitude CO_2 spikes consistently occur at the same times as elevated mixing ratios of observed anthropogenic tracers including CO in Figure 29c and SO_2 in Figure 29d. These low altitude CO_2 enhancements are likely due to anthropogenic area sources and LPS's. Figure 29b provides the time series of the inventory driven fossil fuel CO_2 component along the flight path in comparison with the modeled ocean and biosphere contributions. The modeled fossil fuel CO_2 (inventory approach) is 1 to 5 ppm at low altitudes and is near zero in the free troposphere. From visual inspection of the observed CO_2 in Figure 29a, the anthropogenic CO_2 spikes have approximate enhancements of 4 to 10 ppm, with one very large plume of approximately 26 ppm at 17.1 hours.

The simultaneous peaks of CO and acetonitrile in Figure 29c indicate very distinct forest fire plumes. The spikes of acetonitrile, the forest fire tracer, correspond with spikes in the CO mixing ratios at mid altitudes near 17.4 hr and 21.6 hr. There are no corresponding spikes of SO_2 or other anthropogenic tracers that would indicate that this acetonitrile signal has an anthropogenic source. For other ICARTT flights, the mid-altitude band has an average CO level of 110 ppbv. For these mid-altitude forest fire plumes, the CO levels reach 362 and 370 ppbv respectively. The forest fire source is likely to be from Alaskan or Canadian forest fires as indicated by the adjoint derived influence region in Figure 30.

The maximum model derived forest fire CO along the flight is 60 ppbv. The model results do not reflect the influence of the concentrated forest fire plumes because the forest fire influence is modeled in the boundary conditions using a global transport model with relatively coarse resolution.

4.6 CO Method Uncertainty

The oxidation of reduced carbon species to CO is a potential source of uncertainty for the CO method. During the summer, emissions of anthropogenic and biogenic VOC's result in significant secondary sources of CO. The model ^{voc}CO during the ICARTT period is typically low, with an average of 7 ppbv. However, high values of ^{voc}CO as large as 85 ppbv occur at hot spots across the model domain, particularly over the southeast where biogenic emissions are high. In Figure 31, a snapshot of the surface level ^{voc}CO on July 20th indicates up to 50 ppbv mixing ratios in the Midwest and the Southeast. A photochemical CO source of 50 ppbv results in an enhancement in $^{ff}CO_2$ of 2.5 ppm by the static CO method (equation 4).

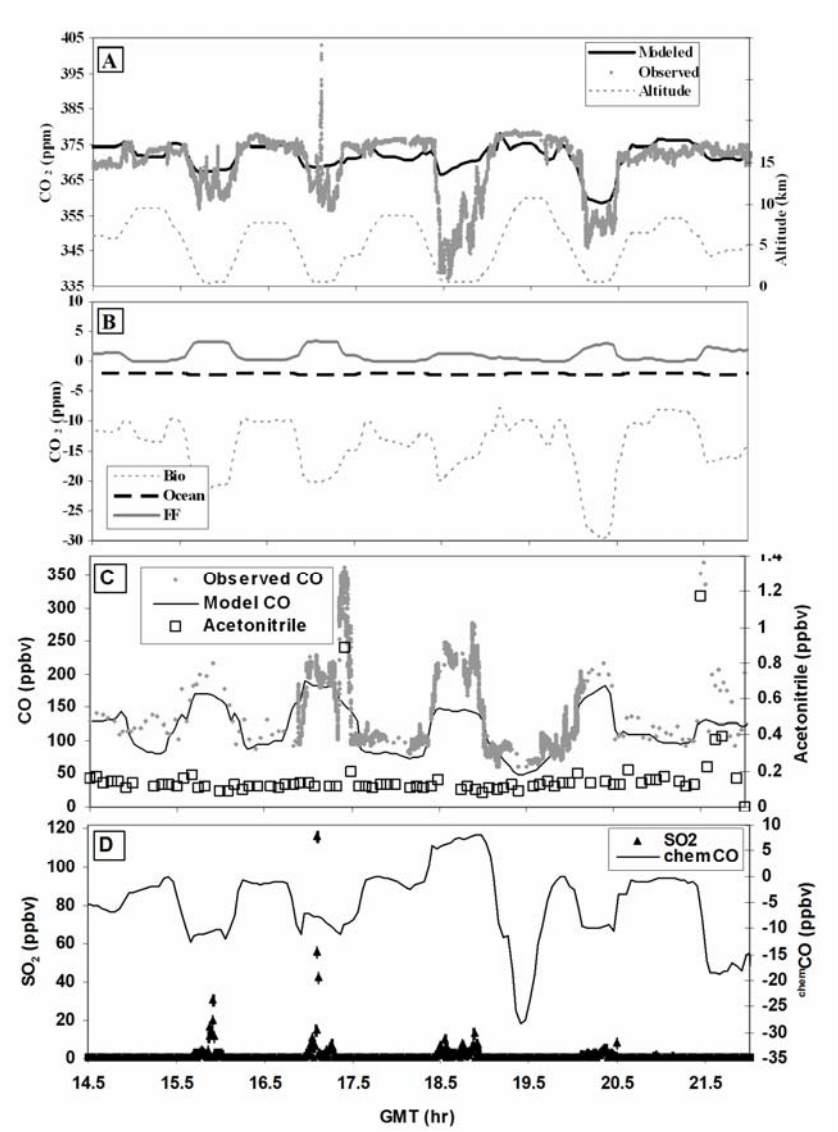

Figure 29. Time series along ICARTT DC-8 flight path on July, 20, 2004, of observed (1 Hz) and modeled CO_2 (A), modeled contributions of biosphere, ocean, and fossil fuel fluxes (B), model and observed CO with acetonitrile as a biomass burning tracer (C), and observed SO_2 and the modeled chemistry contribution to the CO mixing ratio (D). The model fossil fuel results shown here are driven by inventory emissions.

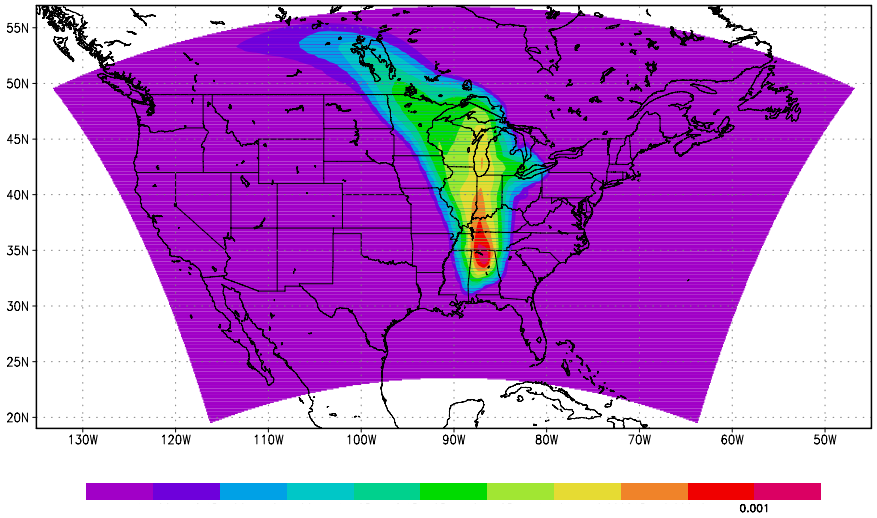

Figure 30. 3-day cone of influence for observation point on the July 20,2004 flight path that intersected a forest fire plume (latitude 34°, longitude 274°, altitude 3.6 km). The values shown are normalized adjoint-derived sensitivities.

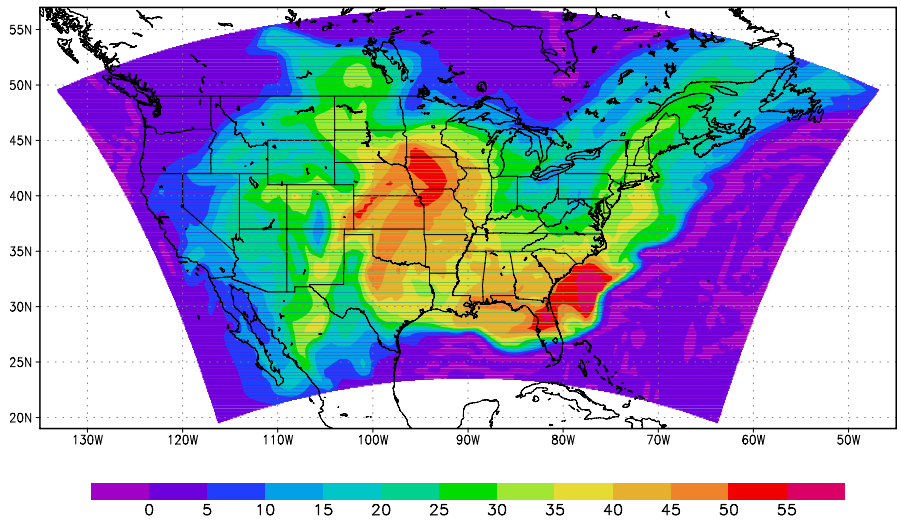

Figure 31. Modeled CO mixing ratios from VOC oxidation (ppbv) at 21 hr (GMT), July 20th at surface model layer.

The net CO production from chemical reactions, ^{chem}CO, is relatively small because the effect of the OH sink and VOC source tend to offset each other. The average ^{chem}CO value along the ICARTT flight paths is -5.3 ppbv indicating a slight net sink. However, there are hot spots across the model domain with net chemical sources in the southeast U.S. up to 83 ppbv and net chemical sinks in the Rocky Mountains as low as -75 ppbv. A net chemical CO mixing ratio of 80 ppbv results in an adjustment in $^{ff}CO_2$ of 4 ppm by the static CO method. The net chemical contribution along the July 20th flight path is shown in d. The net chemical effect during this flight is primarily a sink, except near 18.5 hr where anthropogenic VOC emissions result in a net chemical source.

Forest fire sources are also a significant component of CO mixing ratios over North America. The effect of forest fires in Alaska and Canada during the ICARTT period on CO mixing ratios was estimated using model results and acetonitrile observations, a biomass burning tracer. In Figure 32, the observed CO is plotted versus observed CO_2 along with shape coding for elevated acetonitrile. The general trend is a negative correlation of CO and CO_2 due to the co-location of the CO source and biogenic CO_2 sink at the surface. The forest fire influenced observations (circles) break from this trend with CO enhanced by up to 240 ppbv. A 240 ppbv increment in CO results in an increment of $^{ff}CO_2$ by the static CO method of 12 ppm.

The model estimates of forest fires CO result in an average contribution along all flight paths of 9.5 ppbv. The model estimates of ^{bb}CO along the ICARTT flight path greatly underestimate CO in the more concentrated plumes. In order to obtain a better estimate of biomass burning CO, the observed and model results are applied in a linear regression (see section 2.3). Elevated acetonitrile values greater than 0.28 ppbv were used to separate background acetonitrile from forest fire influenced acetonitrile. The linear regression has an R^2 of 0.92, indicating a strong relationship between the ^{bb}CO and acetonitrile in biomass burning plumes.

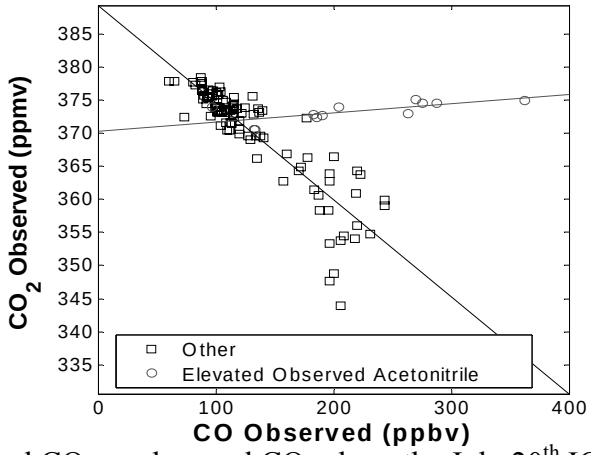

Figure 32. Observed CO vs. observed CO_2 along the July 20th ICARTT flight with circles indicating enhanced acetonitrile.

Preliminary comparison of model and measured CO_2 indicated that, in some cases, the ratio R was in error during interception of LPS plumes. An alternative tracer (SO_2) method was developed to provide a better $^{ff}CO_2$ estimate, and calculate an alternative R in the LPS plume. One of the largest fossil fuel CO_2 plumes encountered in the ICARTT period occurs on July 20th at 17.1 hr (Figure 29a). The CO peak at this time is not enhanced to the extent that the CO_2 peak is enhanced (Figure 29c). However, the SO_2 measurements near this peak reflect the high intensity of the fossil fuel plume (Figure 29d). The moderate enhancement of the CO collocated with the extreme enhancements of CO_2 and SO_2 are indicators of efficient LPS combustion.

The LPS emissions within the footprint of the observation are show in Figure 33. The observation point at 17.1 hr (marked X) is downstream of several large anthropogenic sources. The closest source in the influence region is the Wansley Electric Utility which burns coal and natural gas. The hourly emissions for Wansley indicate that the emitted ratio of SO_2 to CO_2 is significantly variable in time with a value of 0.0045 mol SO_2/mol CO_2 around the time of the large LPS observation.

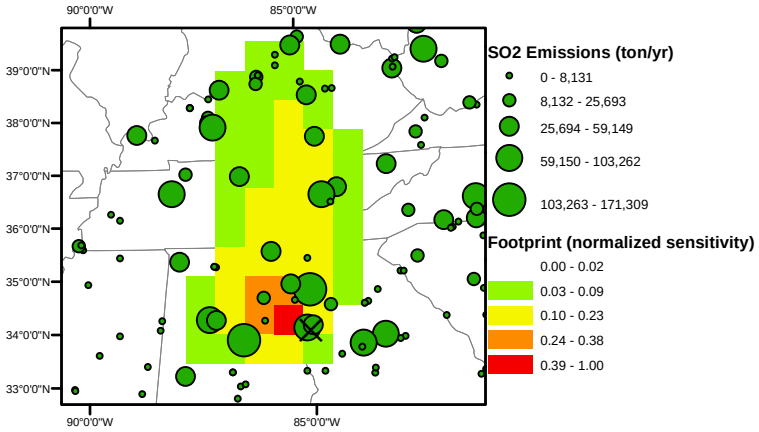

Figure 33. Emissions sources for large anthropogenic spike observed during ICARTT at 17.1 hr GMT on July 20, 2004. The X marks the location of the observation. Shaded grid cells are the adjoint derived footprint for the observation. Green circles are 2004 annual emissions of SO_2 from EPA Clean Sky Clean Air Markets inventory.

In Figure 34, the SO_2 and CO_2 observations in the plume are shown. The SO_2 observation point centered on the plume at 17.104 hr has a value of 116 ppbv. A rough estimate of the fossil fuel CO_2 in this plume is estimated as 26 ppm based on the difference between the average CO_2 values for the SO_2 sample period centered on 17.104 and the average of the CO_2 values just before and after the plume. By dividing the observed SO_2 by the ratio of SO_2/CO_2, the $^{ff}CO_2$ is estimated as 26 ppm. Back calculating the CO:CO_2 ratio R with the enhanced CO of 115 ppbv and estimated $^{ff}CO_2$ of 26 ppm gives an effective CO:CO_2 ratio R' = 5. Using the model CO method (equation 6), a much higher R value of 24.5 is estimated. The difference between $^{ff}CO_2$ estimates for enhanced CO of 115 ppbv using the static R of 20 and revised R' of 5 is 20 ppm.

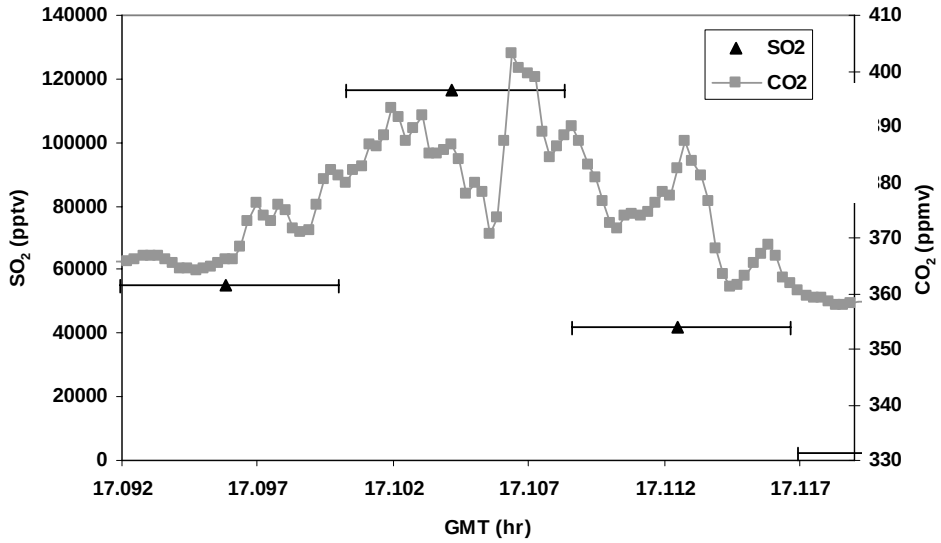

Figure 34. Large anthropogenic spike of SO_2 and CO_2 around 17.1 hr on the July 20, 2004 ICARTT flight. Horizontal bars indicate sample intake period for SO_2.

4.7 Estimates of $^{ff}CO_2$

By comparing the differences in $^{ff}CO_2$ calculated by the various methods, the uncertainty related to several of the assumptions of the CO methods can be quantified. Of all the possible comparisons that can be made, a few are most instructive. First, a comparison of the basic and revised CO methods (either using static R, or model-predicted R ratios) can inform us of the uncertainty expected due to the combined effect of the net chemical component and the forest fire component. Second, a comparison of the static methods (equations 4 and 5) versus the model methods (equations 6 and 7) quantifies the effect of assuming a spatially and temporally averaged R ratio versus one that reflects the spatial variation of the emission inventory.

For the July 20th flight, the revised static results are on average 0.8 ppm less than the static method results (Figure 35a). The difference between the revised static and

static methods is primarily due to forest fires and not the chemical component. The average forest fire CO source is 24 ppbv on this flight while the net chemical component is relatively small at -6 ppbv. However, near 19.5 hr the net chemical component is a strong sink (-28 ppbv) and the forest fire contribution is small, resulting in estimates of $^{ff}CO_2$ that are 1 ppm larger for the revised static method than the static method. Inside the forest fire plumes (near 17.4 hr and 21.5 hr), the static method is on average 8.2 ppm greater than the revised static method.

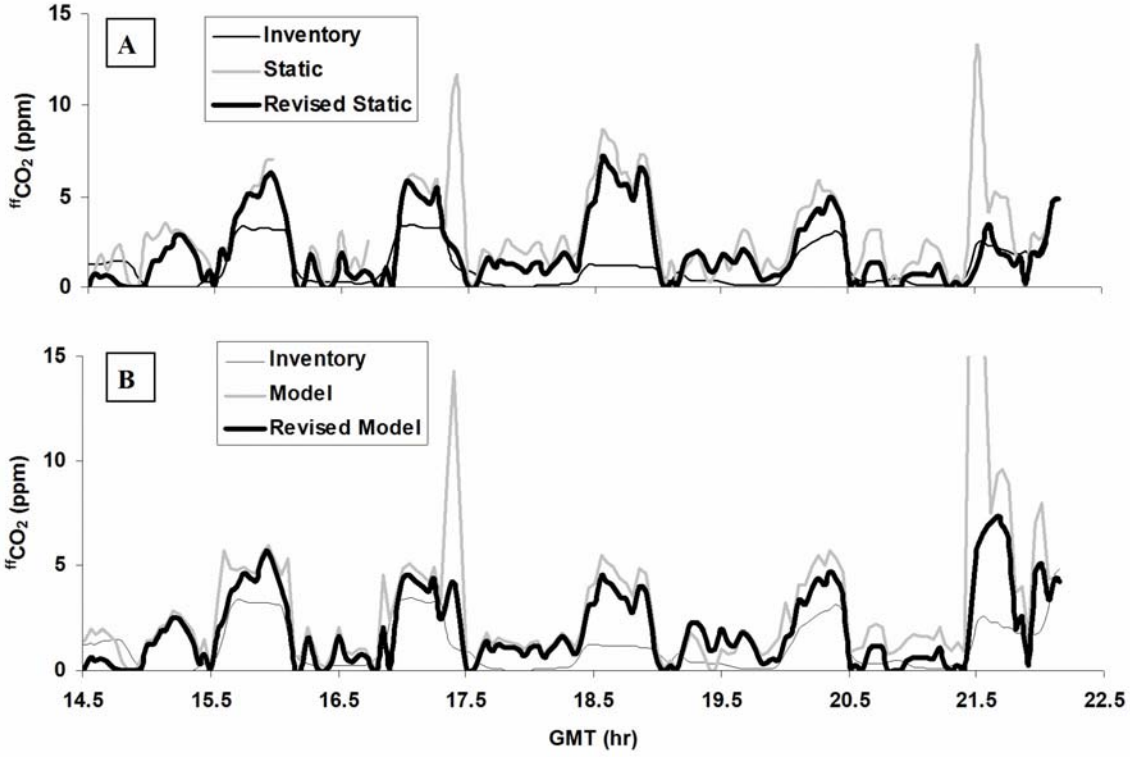

Figure 35. Time series of $^{ff}CO_2$ from inventory method (thin black line), CO methods that do not account for non-fossil fuel CO (grey line), and revised CO methods accounting for forest fires and photochemistry (thick black line). The static CO methods (equations 4 and 5 with R = 20) are shown in A and the model CO methods (equations 6 and 7 with estimated by the transport model) are shown in B.

Estimates of $^{ff}CO_2$ based on the model CO approach and the revised model CO approach are shown in Figure 35b. When the fossil fuel components are low, the modeled R ratio becomes very sensitive to errors in $^{mod,ff}CO$. To prevent unrealistic variability in R, the average model value of 23 was used when $^{mod,ff}CO$ is less than 4 ppbv. This accounts for 44% of values along the flight paths. The average difference between the revised model and model approach results is 0.7 ppm due to the forest fire contributions. Inside the forest fire plumes (near 17.4 hr and 21.5 hr), the static method is on average 7.2 ppm greater than the revised static method.

For all flights, the revised methods tend to result in slightly lower values than the base case methods because the biomass burning CO is typically larger than the net chemical CO. The average difference in $^{ff}CO_2$ between the model and revised model methods is 0.1 ppm. This difference is plotted for all flight paths in Figure 36. Over half of the observation points have absolute differences of less than 0.5 ppm. The largest negative differences, ranging from -5 to -24 ppm, occur due to forest fire influences during the July 20th and July 31^{rst} flights. The most prominent positive differences, 1.4 to 2.6 ppm, occur offshore of the northeast and southeast where the VOC oxidation makes a large contribution to the CO mixing ratio.

A comparison of the static methods (equations 4 and 5) with the model methods (equations 6 and 7) can be used to provide a preliminary estimate of the CO method uncertainty due to the assumption of a spatially uniform ratio R. For all ICARTT observations, the average difference between the revised model and the revised static approaches is 0.02 ppm due to the fact that the average model R value is similar to the static value. However, the difference between the revised model and model method estimates can be as high as 9.8 ppm in plumes where the model predicts efficient combustion (R<20) and as small as -3.6 where the model predict inefficient combustion (R>20).

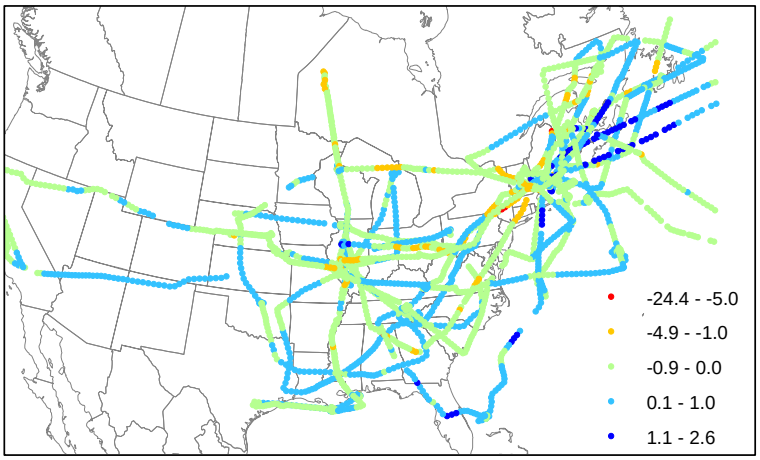

Figure 36. Difference between $^{ff}CO_2$ estimates from the revised model CO approach and the model CO approach (ppm CO_2) for all ICARTT DC8 flights.

For CO_2 inversion applications, the uncertainty in $^{ff}CO_2$ propagates to the uncertainty in the residual mixing ratios, $^{r}CO_2$, by equation 1. For example, if unaccounted VOC sources resulted in an overestimate of $^{ff}CO_2$ by the static CO method, then $^{r}CO_2$ could be underestimated. The inversion model would then retrieve a decreased surface flux value which could be mistakenly interpreted as an increase in photosynthesis. To determine if the uncertainty in the CO method is significant relative to $^{r}CO_2$, the $^{r}CO_2$ was estimated along the ICARTT flight path. The residual CO_2 is obtained by driving the transport model with the fluxes described in section 2.1, including the inventory estimates of $^{ff}CO_2$. The fraction of the CO uncertainty over the residual mixing ratio is calculated to determine the significance of uncertainty for inversion applications. The average of the absolute value of this relative difference is 0.3 indicating that the uncertainty is significant relative to the residual mixing ratio.

4.8 Comparison of CO Method Uncertainty with $^{14}CO_2$ Data

The CO method uncertainty estimates are compared with absolute error estimates from a study of $^{14}CO_2$ by the NOAA Global Monitoring Division (GMD) [*Turnbull, et al.*, 2006]. Turnbull et al. (2006) measured boundary layer and background values for CO and $^{14}CO_2$ on August 2nd during an aircraft flight over a sampling site in the northeast (42º 57' N, 72º 37' W). Their results indicate that both the static CO method and the $^{14}CO_2$ method yielded an $^{ff}CO_2$ estimate of 4.2 ppm. Our model results also indicate that the static CO method should be accurate at this place and time. The model R value is 19 which is very similar to the static R value of 20. The modeled chemical sources and sinks are nearly balanced at the sampling time and location, with a ^{chem}CO value of -6 ppbv.

While the net chemical influence at this sampling site is small at the observation time, there are other times during August 2004 when the modeled net chemical sink is as extreme as -27 ppbv. There are also times during August at the sampling site when the static R value may be incorrect as indicated by model R values that range from 16 to 36. Unfortunately, the additional observations from Turnbull et al. (2006) are outside of the model simulation period. Future model runs that cover these other observations may be useful for interpreting the differences between CO and $^{14}CO_2$ method results as well as validating the revised CO method.

4.9 Summary

Analysis of uncertainty in the revised CO method leads to several conclusions related to estimating the fossil fuel component in observed CO_2:

1) If photochemical, biomass burning and LPS contributions are not considered, then these influences may cause uncertainty in the CO-based $^{ff}CO_2$ by as much as 4, 12, and 24 ppm, respectively.
2) Combining acetonitrile and SO_2 observations with model results provides an alternative approach to estimating $^{ff}CO_2$ in concentrated biomass burning and LPS plumes.
3) The CO method uncertainty due is on average 30% of the residual CO_2 mixing ratio along the ICARTT flight paths.

The analysis of model and observed tracers presented here, provided estimates of several aspects of uncertainty in the CO method due to non-anthropogenic components of the CO observation. Future studies of the CO method uncertainty should provide a more comprehensive analysis of errors in R. A complimentary approach to determining CO method uncertainty can be achieved with observations of CO and $^{14}CO_2$ that provide estimates of the absolute error in the CO method. For example, Turnbull et al. (2006) found underestimates of $^{ff}CO_2$ by the CO method of 1 to 5 ppm during winter and spring, with improved agreement during the summer. Combining the approach in the present study with the approach in Turnbull et al. (2006) would allow for the identification of the components of the absolute error, which could lead to improvements in the design of the CO method. Furthermore, the STEM-2K3 model could be used in forecast mode to identify observation times and locations in which uncertainty components such as the net chemical sinks would be most pronounced.

The revised CO method presented here was designed to extract the quantity of $^{ff}CO_2$ from an observation of CO while drawing on model and observed tracers to resolve uncertainties. The revised method could be further developed to incorporate SO_2 observations for reducing uncertainty due to LPS's. The usefulness of observed acetonitrile and SO_2 indicates that long term measurements of these species at carbon observatories would be helpful for improving the CO method in future inversion studies.

CHAPTER 5 ANTHROPOGENIC TRACER RATIOS FROM INTEX-B OBSERVATIONS AND A CHEMICAL TRANSPORT MODEL

5.1 Introduction

In the previous chapter, assumed and modeled ratios of fossil fuel CO:CO_2 were applied for estimating the fossil fuel component of CO_2. The average ratio for the U.S. was assumed to be 20 (ppb CO / ppm CO_2) based on national emissions inventories while ratios as low as 5 were calculated for observations that were influenced by large point sources (LPS). The range of ratios will depend on the efficiency of combustion. For example, high efficiency and low ratios are associated with LPS while low efficiency and high ratios are typical of biofuels.

The anthropogenic CO:CO_2 ratio has been estimated for different source types and countries using economic and energy use data. Gridded anthropogenic emissions inventories for Asia were created as a part of the Transport and Chemical Evolution over the Pacific (TRACE-P) experiment [*Streets, et al.*, 2003]. These emissions were used to calculate the range of anthropogenic CO:CO_2 ratios presented in Table 7 [*Suntharalingam, et al.*, 2004]. The ratios for fossil fuel emissions from China, India, and Southeast Asia are much higher than the ratios for Japan and Korea, reflecting the higher CO emissions from fossil fuel combustion. The U.S. value of 20 falls in between these Asian source ratios. The combustion ratios for biofuels and biomass burning are much higher than for fossil fuel.

During the INTEX-NA experiment (Summer 2004, North America), the variation of the CO_2 observations was dominated by the biosphere influence, masking the contributions of fossil fuel component and preventing a direct estimate of the combustion ratio of CO:CO_2 from observations. Had the experiment been conducted outside of the

growing season, the influence of the biosphere would have been much smaller, allowing for an analysis of the combustion ratios from the observations.

Table 7. Ratios of CO to CO_2 observed during the TRACE-P experiment by sector and region.

Sector	China	Japan	Korea	India	Southeast Asia
FF	38	9	15	42	28
Biofuel	83	110	152	67	143
Biomass Burning	83	83	83	83	83
Biosphere	1	1	1	10	94
Regional average	18	8	19	42	77

Source: Suntharalingam, P., et al. (2004), Improved quantification of Chinese carbon fluxes using CO2/CO correlations in Asian outflow, J. Geophys. Res., 109.

The NASA Intercontinental Transport Experiment B (INTEX-B) provides a data set outside of the growing season in which combustion emissions of CO and CO_2 dominate the variance of the observations. This experiment includes similar measurements from the DC8 aircraft as during INTEX-NA, but covers a different domain and season. The flights occurred during the daytime between March 4 and March 22, 2006 with flight paths over Mexico, the Gulf of Mexico and the southern U.S. as shown in Figure 37. The INTEX-B campaign was part of the MILAGRO field campaign (Megacity Initiative: Local and Global Research Observations) which included participants from many universities and research agencies.

The objective of this chapter is to provide a top-down analysis of the anthropogenic CO:CO_2 ratios using the INTEX-B observations and the STEM regional transport model. The influence of the chemical sources and sinks of CO and biosphere fluxes on CO_2 are accounted for with the model. The STEM adjoint is applied to estimate influence regions for sources.

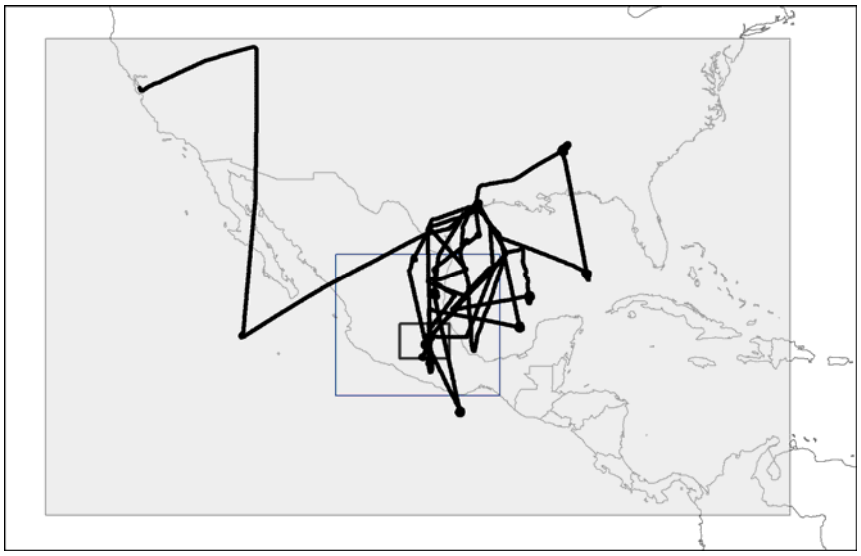

Figure 37. Flight paths (thick black line) of the DC8 during INTEX-B with STEM model domains indicated by three shaded boxes for 60 km, 12 km, and 4 km model grid resolutions.

5.2 INTEX-B Observations of CO_2 and CO

The INTEX-B flight paths sampled air masses with elevated fossil fuel sources over Mexico, the southern U.S., and the Gulf of Mexico. The vertical profiles of CO_2 observations from INTEX-NA and INTEX-B are plotted in Figure 38. The measurement methodology is the same as described in previous chapters. During INTEX-B, the near-surface mixing ratios increased by 1% (3 ppm) above the background mixing ratios while during INTEX-NA there is a 3% decrease (15 ppm). The near-surface decrease observed during INTEX-NA was shown in Chapter 2 to be due to the dominating biosphere

influence. The near-surface increase during the INTEX-B flights is associated with combustion sources as indicated by strong correlations with CO shown in Figure 40.

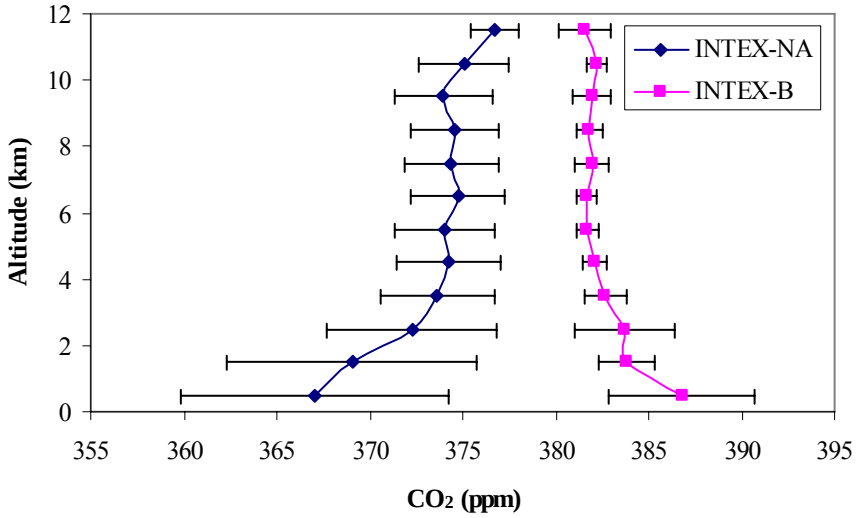

Figure 38. Mean CO_2 (ppm) vertical profiles from the INTEX-NA (blue) and INTEX-NB (pink) observations with standard deviation as error bars.

The upper-troposphere CO_2 concentrations in Figure 38 are on average 375 ppm and 382 ppm for INTEX-NA and INTEX-B respectively. This CO_2 background difference is due to the interannual difference caused by the average annual increase of approximately 1.5 ppm from fossil fuel emissions, the seasonal difference due to high uptake in July and low uptake in March, and the latitudinal gradient due to the latitudinal gradients in biosphere and fossil fuel fluxes. The larger standard deviations (error bars) for INTEX-NA than INTEX-B are due to the fact that the diurnal variation of the biosphere fluxes has an amplitude on the order of 100% while the fossil fuel emissions have an amplitude of 30%.

The CO vertical profiles for INTEX-B and INTEX-NA are shown in Figure 39. The near-surface CO mixing ratios are higher for INTEX-B than INTEX-NA which may be due to less efficient fuel combustion in Mexico sources than U.S. sources. The high variability of the INTEX-B CO at 2.5 km is the Mexico City source which is located at 2.2 km above sea level. The upper-troposphere mixing ratios for INTEX-NA are higher than INTEX-B which was shown in Chapter 4 to be due to the INTEX-NA sampling of forest fire CO at high altitudes that had undergone long range transport from Alaska and Canada.

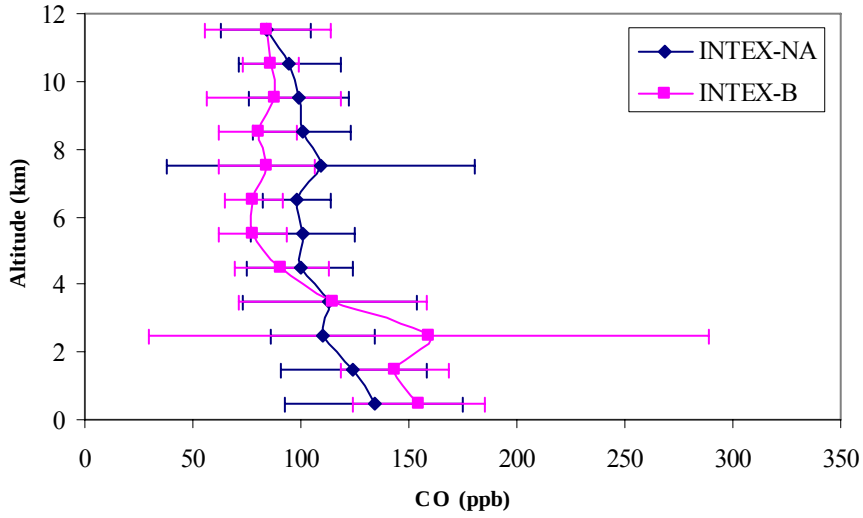

Figure 39. Mean CO (ppb) vertical profiles (km above sea level) from the INTEX-NA (blue) and INTEX-NB (pink) observations with standard deviation as error bars.

The plot of INTEX-B observations of CO_2 to CO in Figure 40 shows two distinct trends for enhanced levels of CO_2 and CO. The steeper trend should be associated with higher combustion efficiencies and the flatter trend should be associated with less efficient combustion sources. The same plot is shown in Figure 41 with the observations

near the Mexico City region in red (within 200 km), the observations near the U.S in green (>26.5 degrees latitude). The Mexico City observations account for all of the low efficiency observations. The U.S. observations of CO and CO_2 are on the low end of the high efficiency trend and are highly correlated ($r^2 = 0.7$). The rest of the elevated mixing ratios (black dots) are observed over Mexico and the Gulf of Mexico. The U.S. observations are not the highest efficiency observed which may indicate low efficiency sources in the U.S and/or long range transport from Mexico.

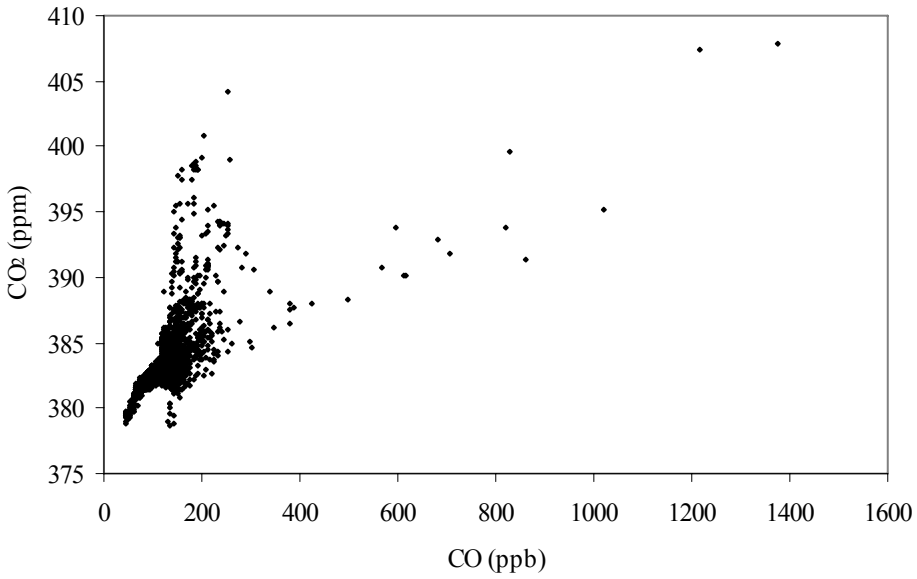

Figure 40. Observed mixing ratios of CO vs. CO_2 along the INTEX-B DC8 flight paths.

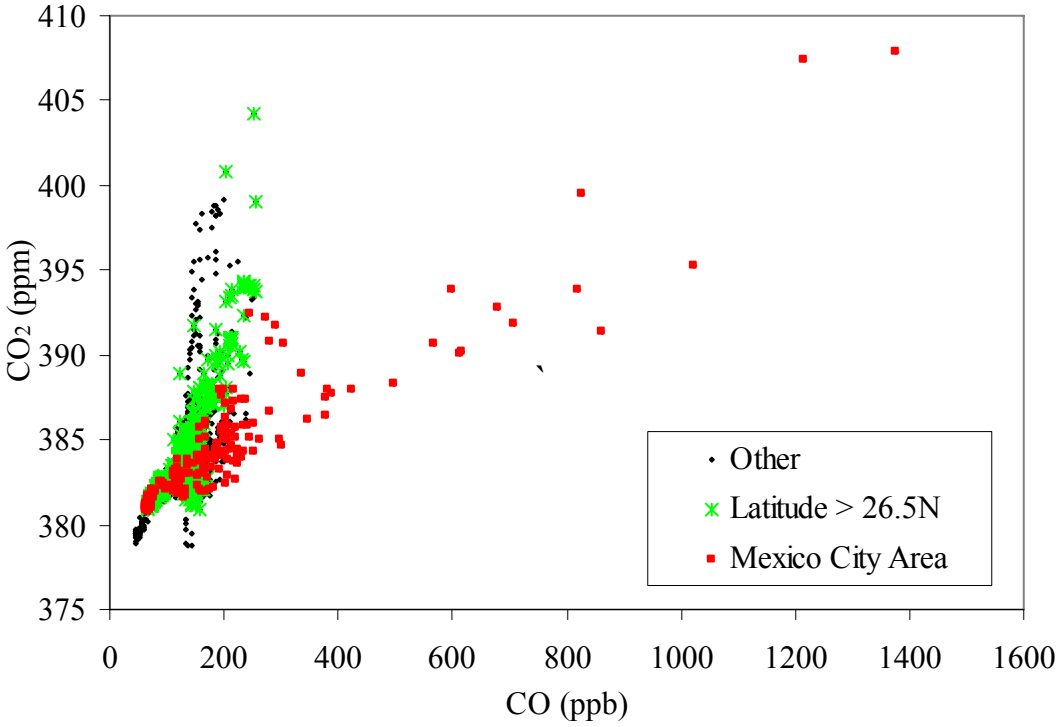

Figure 41. Observed mixing ratios of CO vs. CO_2 along the INTEX-B DC8 flight paths with observations within 200 km of Mexico City in red, observations above 26.5 degrees north in green (over U.S. and northern Gulf of Mexico), and all other observations in black.

5.3 Ratios of Combustion CO:CO_2

The ratio of combustion CO to CO_2 is approximated directly from the INTEX-B observations using fixed background values. The mixing ratios observed at the NOAA GMD Mauna Loa observatory vary from 382 to 383.5 ppm for CO_2 and 70 to 110 ppb for CO during March of 2006. These mixing ratios are used to estimate fixed background values as 90 and 382.5 for CO and CO_2 respectively. The combustion ratio is calculated as,

$$\alpha = ([CO] - 90) / ([CO_2] - 382.5) \quad (1)$$

where α is the combustion ratio (ppb CO / ppm CO_2), [CO] is the observed CO mixing ratio, and [CO_2] is the observed CO_2 mixing ratio. The combustion ratio is calculated for sampling points where the CO_2 mixing ratio is over 385 ppm to reduce sensitivity of the calculated ratio to errors in the approximated CO_2 background.

The combustion CO:CO_2 ratio has a mean of 18±14 ppb CO/ppm CO_2 (log-normal distribution) with the spatial distribution mapped in Figure 42. The ratios over Mexico City vary from 32 to 87. These values are comparable with the combustion of fossil fuel in China and India, biomass burning, and biofuels as indicated by the Asian emissions summarized in Table 7. The enhanced ratios over the rest of Mexico are primarily in the range of 20 to 31. The ratios over the U.S. are lower than Mexico with a mean of 15. The U.S. mean ratio is lower than the ratio of 20 that has been assumed in past studies. The ratios over the region of the Gulf of Mexico just offshore of Mexico are consistently the lowest with typical values ranging from 4 to 12.

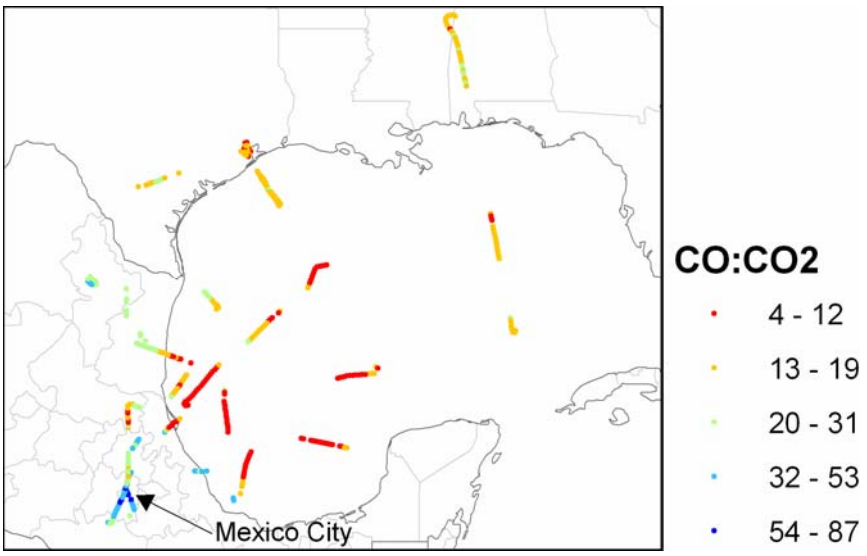

Figure 42. Observed ratios of enhanced CO:CO_2 along the INTEX-B DC8 flight paths where observed CO_2 is greater than 385 ppm.

It is surprising that the ratios offshore of Mexico are the lowest during INTEX-B because these are likely to be downwind of the high ratio region over Mexico. The CO_2 mixing ratios over this region of the Gulf are the highest observed during INTEX-B besides over Mexico City as shown in Figure 43. The closest source region is Mexico City. It would be expected that if Mexico City were the source for theses high CO2 observations, then these observations should also have a similar combustion ratio as over Mexico City. Errors in the combustion ratio calculation due to the fixed background assumption will not increase the Gulf ratios to levels more typical of Mexico combustion sources.

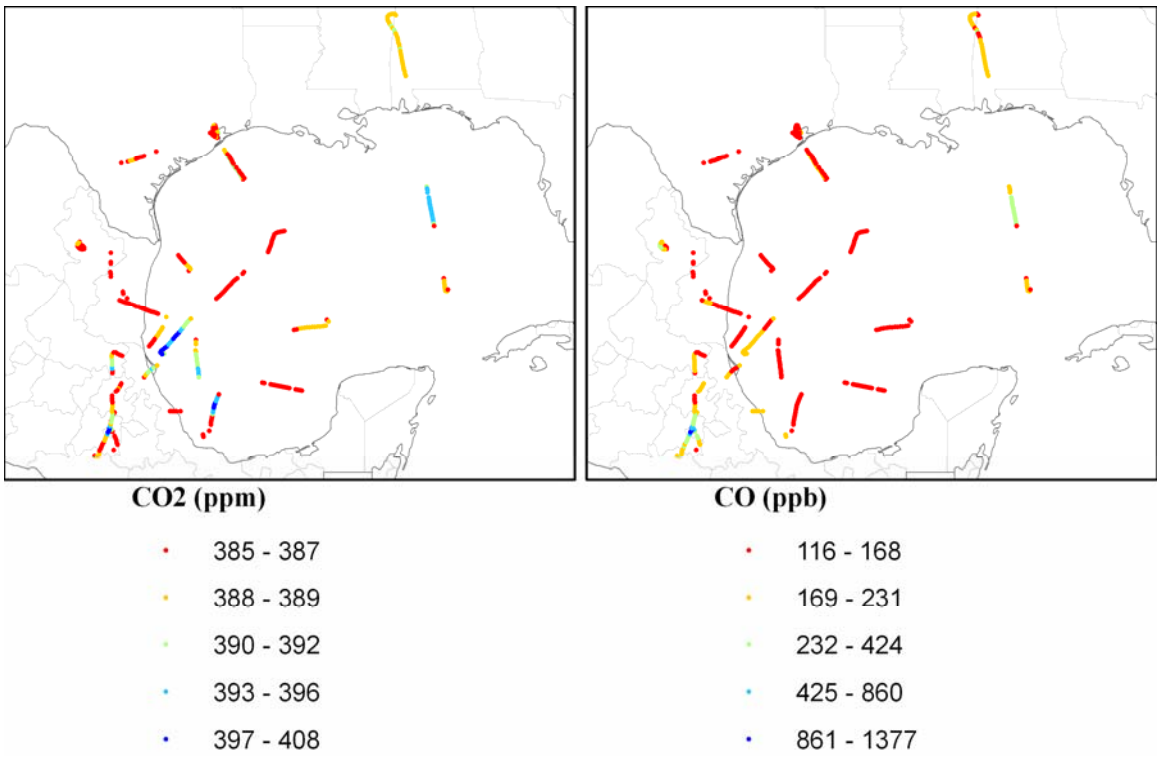

Figure 43. Observed CO2 (left) and CO (right) mixing ratios along the INTEX-B DC8 flight paths.

The explanations for these small ratios include the following. First there could be non-combustion influences on the observations such as biosphere CO_2 fluxes or chemical production and consumption of CO. Transport from regions other than central Mexico would also explain this anomaly. Finally, local sources over the Gulf such as offshore oil rigs may provide an explanation. These alternatives are explored in the following sections.

5.4 Biosphere Influence on INTEX-B CO_2 Observations

Unaccounted for biosphere respiration sources would results in overestimates of the elevated combustion CO2 source (denominator of equation 1) and underestimates of the combustion source CO:CO_2 ratio. The biosphere fluxes are not expected to be large during INTEX-B due to the fact that the flights are in early March before the growing season has begun.

The SiB NEE biosphere fluxes for March 2003 are used to drive the STEM model on the 60 km by 60 km domain for approximating the biosphere contributions along the DC8 flight paths. In Figure 44, the biogenic mixing ratios are mapped along the portions of the flight path were the elevated combustion mixing ratios are observed. Net sink contributions are found over the U.S. and net source contributions are found over Mexico. The biosphere contributions over the Gulf of Mexico are very small and unlikely to influence the calculations of the combustion ratio.

There is some observational evidence that the variability of the biosphere component may be larger than indicated by model results. At several segments of the INTEX-B flight paths there were reported CO_2 measurements below the background levels. The vertical profile in Figure 45, indicates the altitudes of these observations. The low CO_2 mixing ratios observed at low altitude are very likely to be caused by the

biosphere sink. These values are 3 ppm below background while the modeled biosphere predicts a depression of 0.06 ppm.

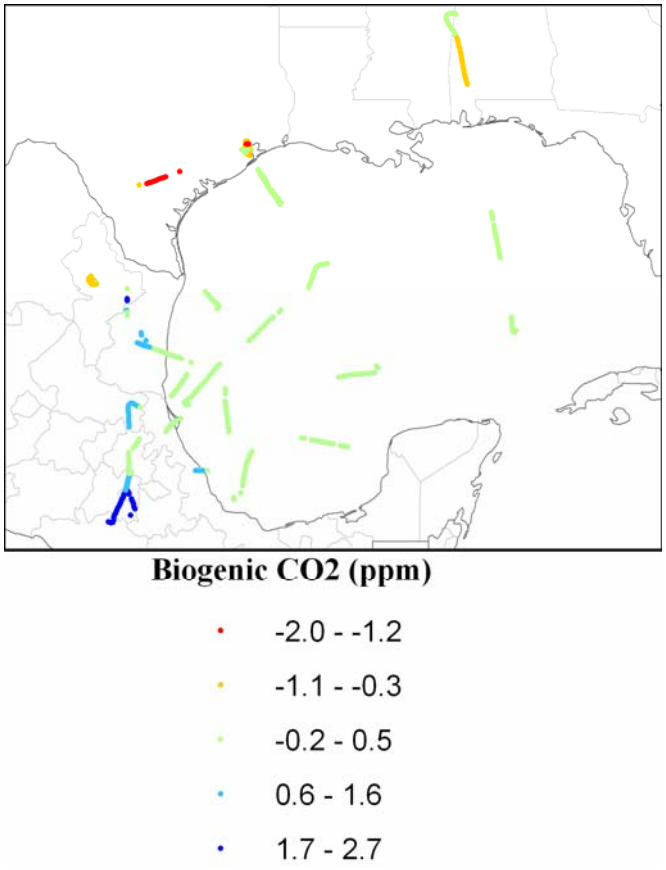

Figure 44. Model CO_2 from SiB NEE fluxes along the INTEX-B DC8 flight paths.

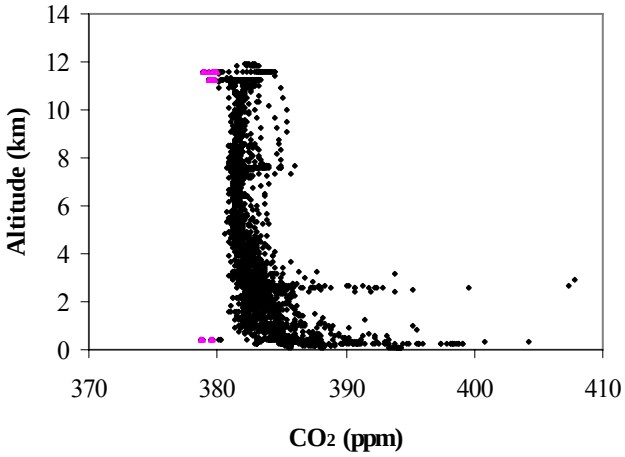

Figure 45. Vertical profile of observed CO_2 mixing ratios with values below 380 ppm highlighted in pink.

The lows observed at high altitude cannot be associated with the biosphere influence due to their distance from the surface. These observations are likely due to stratospheric intrusion because this CO_2 depression is strongly correlated with an ozone enhancement.

5.5 Chemical CO Sources and Sinks

Chemical sinks of CO from oxidation with OH could also be responsible for the surprisingly small values of combustion CO:CO_2 calculated over the Gulf. The net chemical contribution to CO was calculated as in Chapter 4, by taking the difference of the full chemistry STEM run and a STEM run with no chemical reactions. A positive chemical contribution indicates a net source of CO from chemical reactions while a negative chemical contribution indicates a net sink of CO from chemical reactions. The mean chemical contribution along the INTEX-B flight paths is 14 ± 43ppb, indicating an

overall stronger influence from VOC sources of CO than OH oxidation consumption of CO.

There are three segments of the INTEX-B flights where the magnitude of the net chemical component of CO is over 300 ppb. These three cases occurred during sampling directly over Mexico City on March 11th, 12th, and 19th. The time series for the CO mixing ratios during these events is shown in Figure 46. During the March 11th and 12th, the model results with no chemical reactions (blue) shows much greater similarity to the observations (green) indicating a possible overestimate by the model of chemical sinks. These two passes over Mexico City correspond to two of the four largest pollution events sampled by the DC8. On the March 19th flight segment, the model with no chemical reactions greatly overestimates the observations while the full chemistry model shows better agreement. In this case the chemical sinks of CO improved the modeling capability.

The chemical contribution to modeled CO is plotted in Figure 47 along the flight paths that showed enhanced CO_2. The net chemical CO mixing ratios in the Gulf close to the shore of Mexico, are positive indicating a net chemical source of CO. The ratios of combustion CO:CO_2 calculated in this region by equation 1 were unexpectedly small. If the net chemical component for CO is a net source as indicated by the model, then the chemical source of CO should also be subtracted from the numerator of equation 1, making the CO:CO_2 ratio even smaller. The chemical influence on CO cannot help explain the unexpectedly small combustion ratio.

5.6 Influence Regions for Gulf of Mexico Observations

The low ratios over the Gulf offshore of Mexico are surprising because there are considerable enhancements of CO_2 in these observations and the closest CO_2 source is Mexico where the combustion ratios are very high. Another potential explanation of the

small ratios is transport from a different source region than Mexico City. To analyze the source regions for these observations, the adjoint sensitivity approach presented in Chapter 4 is applied to the INTEX-B observations. The 60km by 60km STEM domain is used to generate influence regions for two low ratio observation locations (L1 and L3) and one high ratio locations (Figure 48).

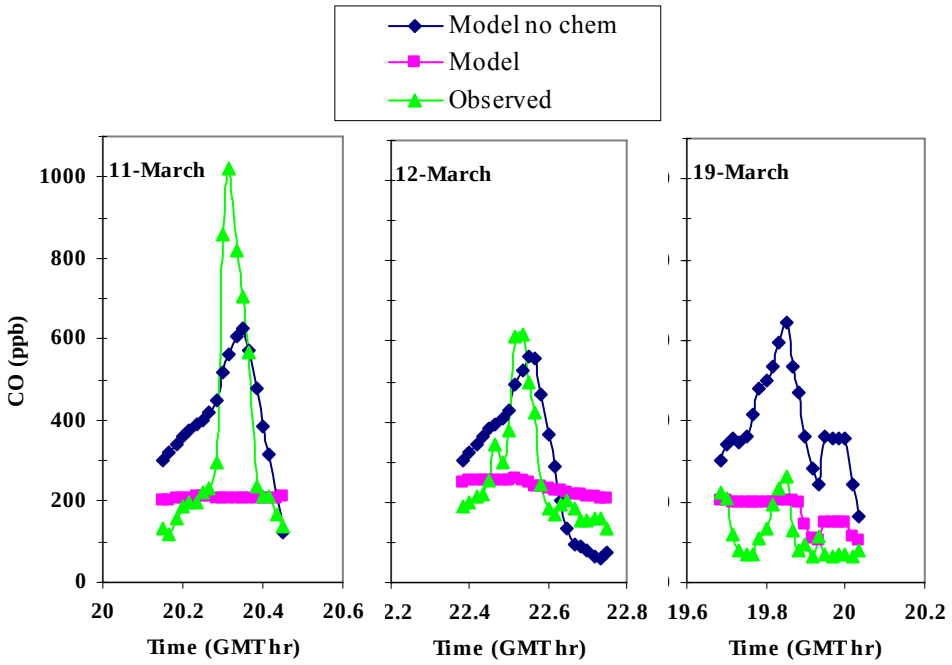

Figure 46. The CO concentrations during the three large pollution events observed from the DC8 including observed CO (green), modeled CO (pink), and modeled CO with no chemical reactions (blue). All three events were sampled over Mexico City.

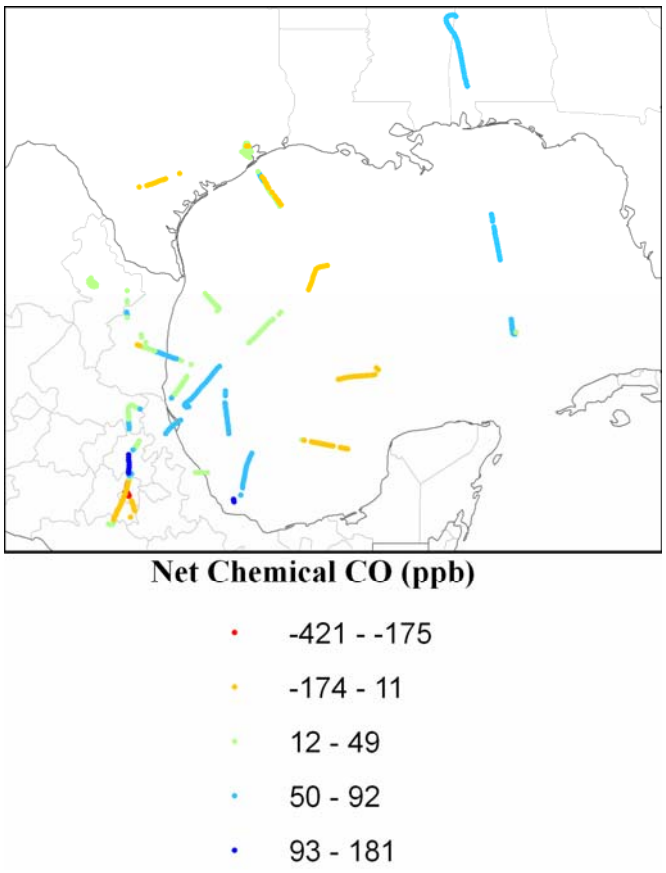

Figure 47. The net chemical contribution to the modeled CO component along the flight paths. Flight paths are limited to those having observed CO_2 mixing ratios above 385 ppm.

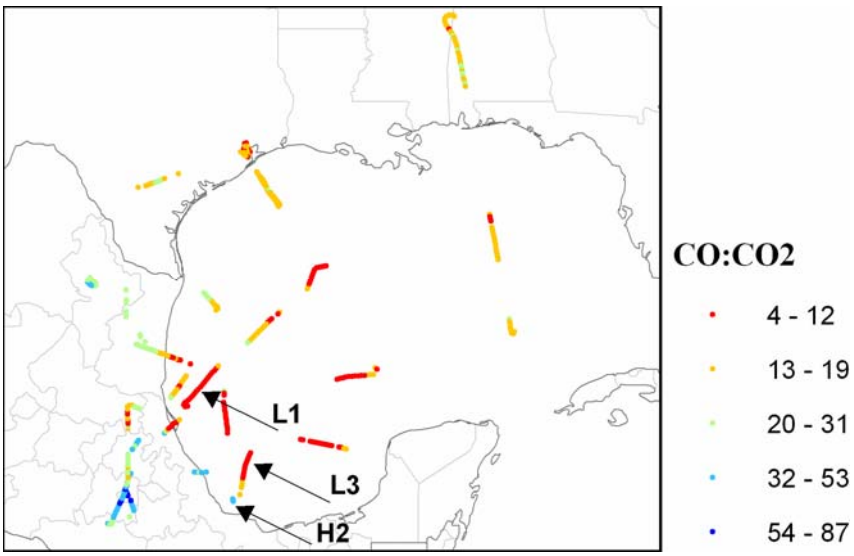

Figure 48. Influence regions for measurement locations over the gulf where the combustion $CO:CO_2$ ratio was low (L1 and L3) and where the combustion $CO:CO_2$ ratio was high (H2). The warm colors indicate regions of strong influence and the cool colors indicate regions of less influence.

In Figure 49 the influence regions are shown with the low ratio influence regions in the top row and the high ratio influence region in the bottom row. The influence region for the high combustion ratio observation (H2, bottom) passes directly over Mexico City. The Mexico City source region has the high emissions of CO which explains the high combustion $CO:CO_2$ ratio. The influence regions for the low combustion ratios (L1 and L3, top row), are concentrated over coastal and southern Mexico which have relatively small emissions of CO and CO_2. This explains why the low ratios observed offshore of Mexico are not similar to the typical high ratios for Mexico emissions sources. However it is still unclear what source supplied the very high levels of CO_2 and modest elevations of CO at the L1 and L3 observation locations.

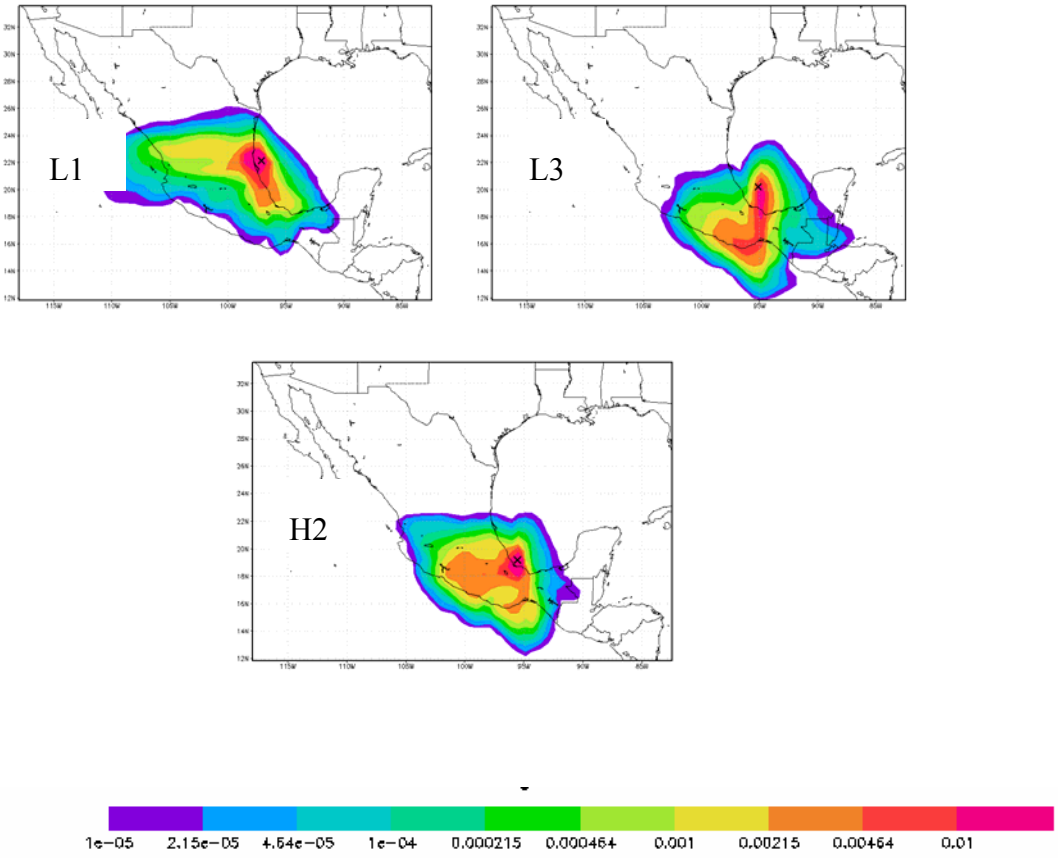

Figure 49. Influence regions (normalized) for measurement locations over the gulf where the combustion CO:CO_2 ratio was low (L1 and L3) and where the combustion CO:CO_2 ratio was high (H2). The warm colors indicate regions of strong influence and the cool colors indicate regions of less influence.

5.7 Offshore oil rig sources of CO and CO_2 over the Gulf

The influence regions shown above suggest that the observations offshore of Mexico are not connected by transport to the large Mexico combustion sources. This explains why the combustion ratios offshore of Mexico are much smaller than over Mexico. The very large CO_2 enhancements and average CO enhancements observed offshore of Mexico must have a different source.

One possible source for the enhanced CO_2 is offshore oil rigs which have large emissions of CO_2 and CH_4 from gas flaring [*Christensen*, 1994; *Countess and Browne*, 1993]. The CH_4 emissions from offshore oil rigs are very large due to gas flaring which makes CH_4 a good tracer of this source type tracer. A recent study analyzed the emissions of the Sonda de Campeche offshore oil rig in this region of the Gulf of Mexico in comparison with offshore oil rig emissions reported by BP and Shell [*Schifter, et al.*, 2005]. The CH_4 and CO_2 emissions and the calculated combustion ratio for CH_4:CO_2 are shown in Table 8. The combustion ratios for CH_4:CO_2 range from 6 to 12 ppb CH_4 / ppm CO_2. Typical emission ratios are also calculated from emissions reported for United Kingdom offshore oil rigs [*UKOOA*, 1998], resulting in a CH_4:CO_2 ratio of 3 ppb/ppm and a CO:CO_2 ratio of 9 ppb/ppm. Alternatively, the ratio for continental Asia emissions calculated from the Streets et al. [2003] inventory is 33 ± 21 ppb CH_4 / ppm CO_2.

Table 8. Offshore oil rig emissions of CO_2 and CH_4 for BP, Shell, and Pemex platforms.

Source	CO_2 (tons/yr)	CH_4 (tons/yr)	CH_4/CO_2 (molar)	CH_4/CO_2 (ppb/ppm)
BP	76.6	0.33	0.0118	11.8
Shell	92	0.398	0.0119	11.9
Pemex Sonda Campeche	19.08	0.0397	0.0057	5.7

Source: Schifter, I., et al. (2005), Air emissions assessment from offshore oil activities in Sonda de Campeche, Mexico, Environmental Monitoring and Assessment, 109, 135-145.

The vertical profile of the mean CH_4 observations from INTEX-B DC8 flights is shown in Figure 50. The observations are enhanced near the surface sources above the background concentrations. The elevated values around 2 km are due to the altitude of Mexico City at approximately 2 km. The CH_4 vertical profile is similar to the patterns in the CO and CO_2 vertical profiles.

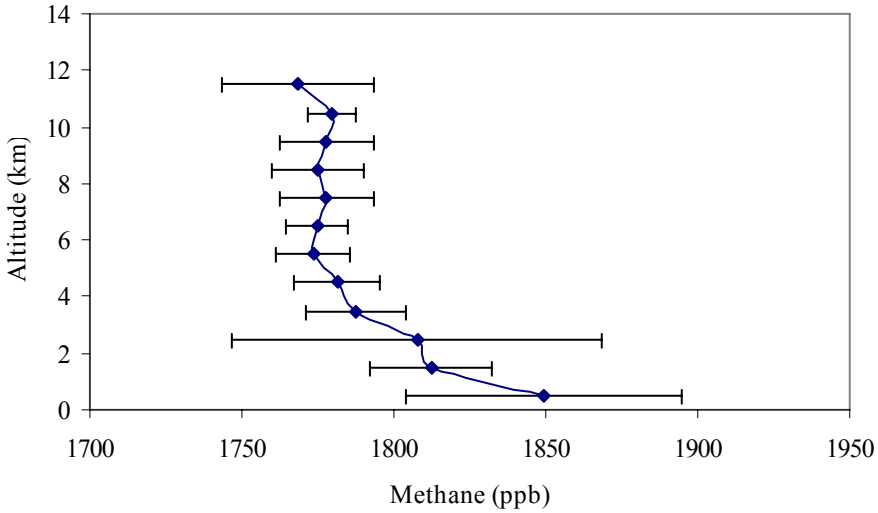

Figure 50. Vertical profile (km above sea level) of mean methane (ppb) observations along INTEX-B DC8 flights with standard deviations as error bars.

The ratio for CH_4:CO2 is calculated for the INTEX-B flights as follows,

$$\beta = ([CH_4] - 1775ppb) / ([CO_2] - 382.5ppm) \quad (2)$$

where β is the CH_4:CO_2 ratio (ppb CH_4 / ppm CO_2), $[CH_4]$ is the observed CH_4 mixing ratio, and 1775 ppb is the fixed background value estimated as the average INTEX-B CH_4 observation above 6 km altitude. The ratio is calculated for sampling points where the CO_2 mixing ratio is over 385 ppm to reduce sensitivity of the calculated ratio to errors in the approximated CO_2 background.

The mapped CH_4 observations and CH_4:CO_2 are shown in Figure 51. Large CH_4 mixing ratios are measured directly over Mexico City and the Gulf locations in question. The three large episodes of CH_4 offshore of Mexico (CH_4 > 1900 ppb) have a mean CH_4:CO_2 ratio of 13 ± 2 ppb/ppm which is similar to the offshore oil rig emissions ratios in Table 8. The low CO:CO_2 ratios with a mean of 6 ± 1 ppb/ppm at this same location is also similar in magnitude to the offshore oil rig emission factor of 5 ppb/ppm. The large

CH_4 observations over Mexico City (CH_4 > 1900 ppb) have CH_4:CO_2 ratios of 30 ± 17 ppb/ppm.

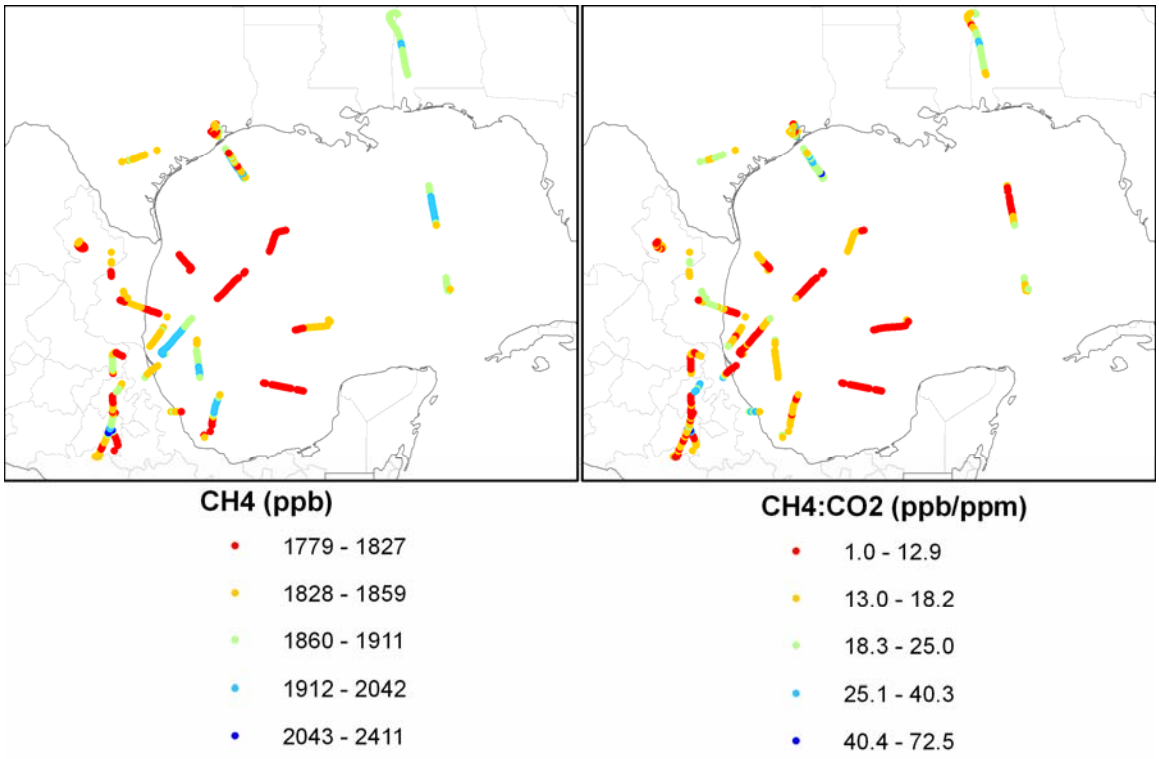

Figure 51. Observed concentrations of methane (top left), CO_2 (top middle), and CO (top right), combustion ratio of CH_4:CO_2 (bottom left), and CO:CO_2 (bottom right) along the INTEX-B DC8 flight segments with CO_2 observations above 385 ppm.

A summary of the CO:CO_2 and CH_4:CO_2 ratios from the INTEX-B observations and emissions inventories is provided in Table 9. The means and standard deviations for the INTEX-B Mexico City values are similar to the land emissions values while the INEX-B nearshore gulf values are similar to the oil rig emissions values.

Table 9. Summary of mean and standar deviations for $CO:CO_2$ and $CH_4:CO_2$ ratios from INTEX-B observations and emissions inventories.

	$CH_4:CO_2$	$CO:CO_2$
INTEX-B Mexico City	30(17)	57(20)
INTEX-B Nearshore Gulf	13(2)	6(1)
Land emissions	33(21)	52(28)
Oil Rig Emissions	10(3)	9(NA)

5.8 Conclusions

The atmospheric observations of CO and CO_2 during INTEX-B were used to estimate the combustion ratio of $CO:CO_2$ for Mexico and U.S. sources. Calculated combustion ratios over the U.S. had a mean of 15 which is lower than the approximated ratio of 20 used in past studies. Combustion ratios observed over Mexico were comparable to combustion ratios calculated for emissions in China and India.

Very low $CO:CO_2$ combustion ratios were observed offshore of Mexico with modest elevations of CO and very high levels of CO_2 and CH_4. A detailed analysis of these flight segments indicates that the source of the offshore pollution may be from offshore oil rigs and not from sources over Mexico City. Given that the INTEX-B campaign is to quantify the Mexico City outflow, future studies should be careful in attributing the offshore pollution events to long range transport from Mexico City without further investigation of the offshore oil rig emissions.

CHAPTER 6 SUMMARY AND RECOMMENDATIONS

6.1 Summary

Atmospheric measurements of process specific tracers can be used to infer information about processes that influence the surface flux of CO_2. In this dissertation, a novel tracer approach has been developed to quantify the biosphere fluxes of respiration and photosynthesis. The dominant flux of COS by plant uptake was quantified by a linear relation to CO_2 photosynthesis fluxes using atmospheric measurements and a transport model (Chapter 2). The STEM 4D-Var data assimilation model was modified for the optimization of CO_2 surface fluxes using only CO_2 measurements and using both CO_2 and COS measurements (Chapter 3). The CO_2-only inversion was only able to improve the net flux and not able to partition the flux improvements to respiration and photosynthesis components. The CO_2/COS inversion could separate the net flux into photosynthesis and respiration. This is the first time, to our knowledge, that observations of COS have been used to infer information about CO_2 surface fluxes.

The CO tracer method for estimating the fossil fuel component of CO_2 was revised to account for photochemistry, forest fires, and different combustion source types (Chapter 4). Tracers of acetonitrile, SO_2, and CH_4 were also used to further partition the source types. The revised CO method was compared with past CO method formulations to show a large uncertainty range that is significant to CO_2 inversion studies. The revised approach was applied to identify combustion sources over the U.S. (Chapter 4) and Mexico (Chapter 5).

6.2 Recommendations

Given the improved results with the use of the COS, CO, acetonitrile, SO_2, and CH_4 tracers it is clear that top-down analysis of CO_2 fluxes will benefit from the inclusion of tracer techniques. The simultaneous measurements of CO_2 with these tracers should be pursued in future carbon cycle studies. The implementation of these methods is straight forward with existing measurement and modeling techniques.

The COS technique for partitioning photosynthesis and respiration fluxes is based on a linear relation between COS plant uptake and CO_2 photosynthesis uptake. This assumption is supported by very strong linear correlations between COS and CO_2 observations over diverse landcover types and sampling times. However, the variability that is not explained by the linear relationship should be pursued and incorporated into the COS/CO_2 inversion approach. Eddy flux observations of COS are under development and should provide many clues about the details of the COS plant uptake mechanism.

Validation of the revised CO method with radiocarbon observations would be highly desirable for determining the accuracy of this method. Although radiocarbon observations are sparse, data could be utilized from several regional field campaigns for this purpose. This validation could also provide the complementary validation of the STEM representation of atmospheric chemical reactions.

REFERENCES

Andreae, M. O., and P. J. Crutzen (1997), Atmospheric aerosols: Biogeochemical sources and role in atmospheric chemistry, *Science*, *276*, 1052-1058.

Andres, R. J., G. Marland, I. Fung, and E. Matthews (1996), A 1 degrees x1 degrees distribution of carbon dioxide emissions from fossil fuel consumption and cement manufacture, 1950-1990, *Global Biogeochem. Cy.*, *10*, 419-429.

Baker, I., A. S. Denning, N. Hanan, L. Prihodko, M. Uliasz, P. L. Vidale, K. Davis, and P. Bakwin (2003), Simulated and observed fluxes of sensible and latent heat and CO_2 at the WLEF-TV tower using SiB2.5, *Global Change Biol.*, *9*, 1262-1277.

Bakwin, P., K. Davis, C. Yi, S. Wofsy, J. W. Munger, L. Haszpra, and Z. Barcza (2004), Regional carbon dioxide fluxes from mixing ratio data, *Tellus*, *56B*, 301-311.

Bakwin, P., P. P. Tans, D. F. Hurst, and C. Zhao (1998a), Measurements of carbon dioxide on very tall towers: results of the NOAA/CMDL program, *Tellus Series B-Chemical and Physical Meteorology*, *50*, 401-415.

Bakwin, P., P. P. Tans, J. W. C. White, and R. J. Andres (1998b), Determination of the isotopic ($^{13}C/^{12}C$) discrimination by terrestrial biology from a global network of observations, *Global Biogeochem. Cy.*, *12*, 555-562.

Baldocchi, D. D., B. B. Hicks, and T. P. Meyers (1988), Measuring Biosphere-Atmosphere Exchanges of Biologically Related Gases with Micrometeorological Methods, *Ecology*, *69*, 1331-1340.

Barletta, B., S. Meinardi, I. J. Simpson, H. A. Khwaja, D. R. Blake, and F. S. Rowland (2002), Mixing ratios of volatile organic compounds (VOCs) in the atmosphere of Karachi, Pakistan, *Atmos. Environ.*, *36*, 3429-3443.

Blake, N. J., J. E. Campbell, S. A. Vay, H. E. Fuelberg, S. Meinardi, F. S. Rowland, and D. R. Blake (Submitted), Carbonyl sulfide (OCS): Large scale distributions over North America during INTEX-NA and relationship with CO2, *J. Geophys. Res.*

Blasing, T. J., C. Broniak, and G. Marland (2004), Estimates of monthly carbon dioxide emissions and associated $\delta^{13}C$ values from fossil-fuel consumption in the U.S.A., Trends: A Compendium of Data on Global Change, Carbon Dioxide Information Analysis Center, Oak Ridge National Laboratory, U.S. Department of Energy, Oak Ridge, TN, U.S.A.

Blasing, T. J., C. Broniak, and G. Marland (2005), The annual cycle of fossil-fuel carbon dioxide emissions in the United States, *Tellus B*, *57*, 107-115.

Blasing, T. J., C. T. Broniak, and G. Marland (2003), Preliminary estimates of the annual cycle of fossil fuel emissions from the USA, Carbon Dioxide Inf. Anal. Cent., Oak Ridge Natl. Lab., Oak Ridge, Tenn.

Bousquet, P., P. Ciais, P. Peylin, M. Ramonet, and P. Monfray (1999), Inverse modeling of annual atmospheric CO2 sources and sinks 1. Method and control inversion, *J. Geophys. Res.*, *104*, 26161-26178.

Bousquet, P., P. Peylin, P. Ciais, C. Le Quere, P. Friedlingstein, and P. P. Tans (2000), Regional changes in carbon dioxide fluxes of land and oceans since 1980, *Science*, *290*, 1342-1346.

Bowling, D. R., P. P. Tans, and R. K. Monson (2001), Partitioning net ecosystem carbon exchange with isotopic fluxes of CO2, *Global Change Biol.*, *7*, 127-145.

Brenkert, A. L. (1998), Carbon dioxide emission estimates from fossil-fuel burning, hydraulic cement production, and gas flaring for 1995 on a one degree grid cell basis, *http://cdiac.esd.ornl.gov/epubs/ndp/ndp058a/ndp058a.html*.

Brown, K. A., S. M. Kluczewski, and J. N. B. Bell (1986), Metabolism of [35S]-carbonyl sulfide in perennial ryegrass (Lolium Perenne L.) and radish (Raphanus Sativus L.), *Environ. and Experimental Botany*, *26*, 355-364.

Campbell, J. E., N. J. Blake, S. A. Vay, C. O. Stanier, G. R. Carmichael, Y. H. Tang, T. Chai, S. Vay, Y. H. Choi, J. H. Woo, and J. L. Schnoor (In Preparation), Simultaneous assimilation of carbon dioxide and carbonyl sulfide observations for regional surface flux optimization.

Campbell, J. E., G. R. Carmichael, Y. H. Tang, T. Chai, S. Vay, Y. H. Choi, G. W. Sachse, H. B. Singh, J. L. Schnoor, J. H. Woo, J. M. Vukovich, D. G. Streets, L. G. Huey, and C. O. Stanier (2007), Analysis of anthropogenic CO2 signal in ICARTT observations using a regional chemical transport model and its adjoint, *Tellus*, *59B*, 199-210.

Campbell, J. E., J. C. Moen, R. A. Ney, and J. L. Schnoor (In review), Comparison of regression coefficient and GIS-based methodologies for regional estimates of forest soil carbon stocks, *Environmental Pollution*.

Campbell, J. E., J. C. Moen, J. L. Schnoor, and R. A. Ney (2004), Quantifying carbon storage in Wisconsin forests, Center for Global and Regional Environmental Research, University of Iowa, Iowa City, IA.

Carmichael, G. R., D. N. Daescu, A. Sandu, and T. F. Chai (2003a), Computational aspects of chemical data assimilation into atmospheric models, in *Computational Science - Iccs 2003, Pt Iv, Proceedings*, edited, pp. 269-278.

Carmichael, G. R., Y. Tang, G. Kurata, I. Uno, D. Streets, J. H. Woo, H. Huang, J. Yienger, B. Lefer, R. Shetter, D. Blake, E. Atlas, A. Fried, E. Apel, F. Eisele, C. Cantrell, M. Avery, J. Barrick, G. Sachse, W. Brune, S. Sandholm, Y. Kondo, H. Singh, R. Talbot, A. Bandy, D. Thorton, A. Clarke, and B. Heikes (2003b), Regional-scale chemical transport modeling in support of the analysis of observations obtained during the TRACE-P experiment, *J. Geophys. Res.*, *108*, 8823, doi:8810.1029/2002JD003100.

Carmichael, G. R., Y. Tang, G. Kurata, I. Uno, D. G. Streets, N. Thongboonchoo, J. H. Woo, S. Guttikunda, A. White, T. Wang, D. R. Blake, E. Atlas, A. Fried, B. Potter, M. A. Avery, G. W. Sachse, S. T. Sandholm, Y. Kondo, R. W. Talbot, A. Bandy, D. Thorton, and A. D. Clarke (2003c), Evaluating regional emission estimates using the TRACE-P observations, *J. Geophys. Res.*, *108*.

Carter, W. (2000), Documentation of the SAPRC-99 chemical mechanism for VOC reactivity assessment, Final Report to California Air Resources Board Contract No. 92-329, University of California-Riverside.

Chai, T., G. R. Carmichael, A. Sandu, and D. N. Daescu (2006a), Chemical data assimilation of TRACE-P aircraft measurements, *J. Geophys. Res.*, *111*, D02301.

Chai, T. F., G. R. Carmichael, A. Sandu, Y. H. Tang, and D. N. Daescu (2006b), Chemical data assimilation of Transport and Chemical Evolution over the Pacific (TRACE-P) aircraft measurements, *J. Geophys. Res.*, *111*, doi:10.1029/2005JD005883.

Chevallier, F., M. Fisher, P. Peylin, S. Serrar, P. Bousquet, F. M. Breon, A. Chedin, and P. Ciais (2005), Inferring CO2 sources and sinks from satellite observations: Method and application to TOVS data, *J. Geophys. Res.*, *110*.

Christensen, R. R. (1994), Fugitive Emissions from Norwegian Oil and Gas-Production, *Marine Pollution Bulletin*, *29*, 300-303.

Ciais, P., M. Reichstein, N. Viovy, A. Granier, J. Ogee, V. Allard, M. Aubinet, N. Buchmann, C. Bernhofer, A. Carrara, F. Chevallier, N. De Noblet, A. D. Friend, P. Friedlingstein, T. Grunwald, B. Heinesch, P. Keronen, A. Knohl, G. Krinner, D. Loustau, G. Manca, G. Matteucci, F. Miglietta, J. M. Ourcival, D. Papale, K. Pilegaard, S. Rambal, G. Seufert, J. F. Soussana, M. J. Sanz, E. D. Schulze, T. Vesala, and R. Valentini (2005), Europe-wide reduction in primary productivity caused by the heat and drought in 2003, *Nature*, *437*, 529-533.

Ciais, P., P. P. Tans, M. Trolier, J. W. C. White, and R. J. Francey (1995), A Large Northern-Hemisphere Terrestrial Co2 Sink Indicated by the C-13/C-12 Ratio of Atmospheric Co2, *Science*, *269*, 1098-1102.

Conway, T. J., P. P. Tans, L. S. Waterman, and K. W. Thoning (1994), Evidence for Interannual Variability of the Carbon-Cycle from the National-Oceanic-and-Atmospheric-Administration Climate-Monitoring-and-Diagnostics-Laboratory Global-Air-Sampling-Network, *J. Geophys. Res.*, *99*, 22831-22855.

Countess, R. J., and D. Browne (1993), Fugitive Hydrocarbon Emissions from Pacific Offshore Oil Platforms - Models, Emission Factors, and Platform Emissions, *Journal of the Air & Waste Management Association*, *43*, 1455-1460.

Crutzen, P. J. (1976), The possible importance of COS for the sulfate layer of the stratosphere, *Geophys. Res. Lett.*, *3* 73–76.

Daescu, D. N., and G. R. Carmichael (2003), An adjoint sensitivity method for the adaptive location of the observations in air quality modeling, *J. Atmos. Sci.*, *60*, 434-449.

Daley, R. (1991), *Atmospheric Data Analysis*, 457 pp., Cambridge University Press, Cambridge.

Davidson, E. A., and I. A. Janssens (2006), Temperature sensitivity of soil carbon decomposition and feedbacks to climate change, *Nature*, *440*, 165-173.

Denning, A. S., G. J. Collatz, C. G. Zhang, D. A. Randall, J. A. Berry, P. J. Sellers, G. D. Colello, and D. A. Dazlich (1996), Simulations of terrestrial carbon metabolism and atmospheric CO2 in a general circulation model .1. Surface carbon fluxes, *Tellus Series B-Chemical and Physical Meteorology*, *48*, 521-542.

Denning, A. S., R. Oren, and M. others (2005), Science Implementation Strategy for the North American Carbon Program, 68 pp, U.S. Carbon Cycle Science Program, Washington DC.

Denning, S. A., and I. Y. Fung (1995), Latitudinal gradient of atmospheric CO2 due to seasonal exchange with land biota., *Nature*, *376*, 240.

Elliot, S., E. Lu, and F. S. Rowland (1989), Rates and mechanisms for the hydrolysis of carbonyl sulfide in natural waters, *Environmental Science & Technology*, *23*, 458-461.

Engel, A., and U. Schmidt (1994), Vertical Profile Measurements of Carbonylsulfide in the Stratosphere, *Geophys. Res. Lett.*, *21*, 2219-2222.

Engelen, R. J., and A. P. McNally (2005), Estimating atmospheric CO2 from advanced infrared satellite radiances within an operational 4D-Var data assimilation system: Results and validation, *J. Geophys. Res.*, *110*, D18305.

Enting, I. G. (2002), *Inverse Problems in Atmospheric Constituent Transport*, Cambridge University Press, Cambridge.

Enting, I. G., C. M. Trudinger, and R. J. Francey (1995), A synthesis inversion of the concentration and del^{13}C of atmospheric CO_2, *Tellus*, *47B*, 35-52.

EPA (2006), US EPA Clean Air Market Database, http://www.epa.gov/airmarkt/, edited.

Falge, E., D. Baldocchi, J. Tenhunen, M. Aubinet, P. Bakwin, P. Berbigier, C. Bernhofer, G. Burba, R. Clement, K. J. Davis, J. A. Elbers, A. H. Goldstein, A. Grelle, A. Granier, J. Guomundsson, D. Hollinger, A. S. Kowalski, G. Katul, B. E. Law, Y. Malhi, T. Meyers, R. K. Monson, J. W. Munger, W. Oechel, K. T. Paw, K. Pilegaard, U. Rannik, C. Rebmann, A. Suyker, R. Valentini, K. Wilson, and S. Wofsy (2002), Seasonality of ecosystem respiration and gross primary production as derived from FLUXNET measurements, *Agricultural and Forest Meteorology*, *113*, 53-74.

Fan, S., M. Gloor, J. Mahlman, S. Pacala, J. Sarmiento, T. Takahashi, and P. Tans (1998), A Large Terrestrial Carbon Sink in North America Implied by Atmospheric and Oceanic Carbon Dioxide Data and Models, *Science*, *282*, 442-446.

Farquhar, G. D., J. Lloyd, J. A. Taylor, L. B. Flanagan, J. P. Syvertsen, K. T. Hubick, S. C. Wong, and J. R. Ehleringer (1993), Vegetation Effects on the Isotope Composition of Oxygen in Atmospheric Co2, *Nature*, *363*, 439-443.

Francey, R. J., and P. P. Tans (1987), Latitudinal Variation in O-18 of Atmospheric Co2, *Nature*, *327*, 495-497.

Friedlingstein, P., J. L. Dufresne, P. M. Cox, and P. Rayner (2003), How positive is the feedback between climate change and the carbon cycle?, *Tellus Series B-Chemical and Physical Meteorology*, *55*, 692-700.

Fung, I. Y., S. C. Doney, K. Lindsay, and J. John (2005), Evolution of carbon sinks in a changing climate, *Proceedings of the National Academy of Sciences of the United States of America*, *102*, 11201-11206.

Fung, I. Y., C. J. Tucker, and K. C. Prentice (1987), Application of Advanced Very High Resolution Radiometer vegetation index to study atmosphere-biosphere exchange of CO2, *J. Geophys. Res.*, *92*, 2999– 3015.

Gerbig, C., J. C. Lin, J. W. Munger, and S. C. Wofsy (2006), What can tracer observations in the continental boundary layer tell us about surface-atmosphere fluxes?, *Atmos. Chem. Phys.*, *6*, 539-554.

Gerbig, C., J. C. Lin, S. C. Wofsy, B. C. Daube, A. E. Andrews, B. B. Stephens, P. S. Bakwin, and C. A. Grainger (2003a), Toward constraining regional-scale fluxes of CO2 with atmospheric observations over a continent: 1. Observed spatial variability from airborne platforms, *J. Geophys. Res.*, *108*.

Gerbig, C., J. C. Lin, S. C. Wofsy, B. C. Daube, A. E. Andrews, B. B. Stephens, P. S. Bakwin, and C. A. Grainger (2003b), Toward constraining regional-scale fluxes of CO_2 with atmospheric observations over a continent: 2. Analysis of COBRA data using a receptor-oriented framework, *J. Geophys. Res.*, *108*, 4757, doi:4710.1029/2003JD003770.

Geron, C. D., A. B. Guenther, and T. E. Pierce (1994), An improved model for estimating emissions of volatile organic-compounds from forests in the eastern united-states, *J. Geophys. Res.*, *99*, 12773-12791.

Gillon, J., and D. Yakir (2001), Influence of carbonic anhydrase activity in terrestrial vegetation on the 18O content of atmospheric CO2, *Science*, *291*, 2584-2587.

GLOBALVIEW-CO2 (2005), Cooperative Atmospheric Data Integration Project - Carbon Dioxide. CD-ROM, NOAA CMDL, Boulder, Colorado [Also available on Internet via anonymous FTP to ftp.cmdl.noaa.gov, Path: ccg/co2/GLOBALVIEW].

Gloor, M., P. Bakwin, and L. L. Hurst D, Draxler R, Tans P (2001), What is the concentration footprint of a tall tower?, *J. Geophys. Res.*, *106 (D16): 17831-17840 AUG 27 2001*.

Goulden, M. L., S. C. Wofsy, J. W. Harden, S. E. Trumbore, P. M. Crill, S. T. Gower, T. Fries, B. C. Daube, S. M. Fan, D. J. Sutton, A. Bazzaz, and J. W. Munger (1998), Sensitivity of boreal forest carbon balance to soil thaw, *Science*, *279*, 214-217.

Gurney, K. R., R. M. Law, A. S. Denning, P. J. Rayner, D. Baker, P. Bousquet, L. Bruhwiler, Y. H. Chen, P. Ciais, S. Fan, I. Y. Fung, M. Gloor, M. Heimann, K. Higuchi, J. John, T. Maki, S. Maksyutov, K. Masarie, P. Peylin, M. Prather, B. C. Pak, J. Randerson, J. Sarmiento, S. Taguchi, T. Takahashi, and C. W. Yuen (2002), Towards robust regional estimates of CO_2 sources and sinks using atmospheric transport models, *Nature*, *415*, 626-630.

Gurney, K. R., R. M. Law, A. S. Denning, P. J. Rayner, D. Baker, P. Bousquet, L. Bruhwiler, Y. H. Chen, P. Ciais, S. M. Fan, I. Y. Fung, M. Gloor, M. Heimann, K. Higuchi, J. John, E. Kowalczyk, T. Maki, S. Maksyutov, P. Peylin, M. Prather, B. C. Pak, J. Sarmiento, S. Taguchi, T. Takahashi, and C. W. Yuen (2003), TransCom 3 CO_2

inversion intercomparison: 1. Annual mean control results and sensitivity to transport and prior flux information, *Tellus*, *55B*, 555-579.

Gurney, K. R., R. M. Law, A. S. Denning, P. J. Rayner, B. C. Pak, D. Baker, P. Bousquet, L. Bruhwiler, Y. H. Chen, P. Ciais, I. Y. Fung, M. Heimann, J. John, T. Maki, S. Maksyutov, P. Peylin, M. Prather, and S. Taguchi (2004), Transcom 3 inversion intercomparison: Model mean results for the estimation of seasonal carbon sources and sinks, *Global Biogeochem. Cy.*, *18*, doi:10.1029/2003GB002111.

Gurney, K. R., C. Yu-Han, T. Maki, S. R. Kawa, A. E. Andrews, and Z. Zhu (2005), Sensitivity of atmospheric CO_2 inversions to seasonal and interannual variations in fossil fuel emissions, *J. Geophys. Res.*, *110*, doi:10.1029/2004JD005373.

Hakami, A., D. K. Henze, J. H. Seinfeld, T. Chai, Y. Tang, G. R. Carmichael, and A. Sandu (2005), Adjoint inverse modeling of black carbon during the Asian Pacific Regional Aerosol Characterization Experiment, *J. Geophys. Res.*, *110*, doi:10.1029/2004JD005671.

Hakami, A., J. H. Seinfeld, T. F. Chai, Y. H. Tang, G. R. Carmichael, and A. Sandu (2006), Adjoint sensitivity analysis of ozone nonattainment over the continental United States, *Environmental Science & Technology*, *40*, 3855-3864.

Heath, L. S., R. A. Birdsey, and D. W. Williams (2002), Methodology for estimating soil carbon for the forest carbon budget model of the United States, 2001, *Environmental Pollution*, *116*, 373-380.

Hollinger, S. E., C. J. Bernacchi, and T. P. Meyers (2005), Carbon budget of mature no-till ecosystem in North Central Region of the United States, *Agricultural and Forest Meteorology*, *130* 59-69.

Hong, S.-Y., and H.-L. Pan (1996), Nonlocal boundary layer vertical diffusion in a medium-range forecast model, *Mon. Weather Rev.*, *124*, 2322-2339.

Houghton, R. A. (1995), Land-Use Change and the Carbon-Cycle, *Global Change Biol.*, *1*, 275-287.

Houweling, S., F. M. Breon, I. Aben, C. Rodenbeck, M. Gloor, M. Heimann, and P. Ciais (2004), Inverse modeling of CO2 sources and sinks using satellite data: a synthetic inter-comparison of measurement techniques and their performance as a function of space and time, *Atmos. Chem. Phys.*, *4*, 523-538.

Huey, L. G., D. J. Tanner, D. L. Slusher, J. E. Dibb, R. Arimoto, G. Chen, D. Davis, M. P. Buhr, J. B. Nowak, R. L. Mauldin III, F. L. Eisele, and E. Kosciuch (2004), CIMS

measurements of HNO_3 and SO_2 at the South Pole during ISCAT 2000, *Atmos. Environ.*, *38*, 5411-5421.

Intergovernmental Panel on Climate Change (2001), *Climate Change 2001: The Scientific Basis*, 944 pp., Cambridge Univ. Press, New York.

Janssens, I. A., A. Freibauer, P. Ciais, P. Smith, G.-J. Nabuurs, G. Folberth, B. Schlamadinger, R. W. A. Hutjes, R. Ceulemans, E.-D. Schulze, R. Valentini, and A. J. Dolman (2003a), Europe's Terrestrial Biosphere Absorbs 7 to 12% of European Anthropogenic CO2 Emissions, *Science*, *300*, 1538-1542.

Janssens, I. A., A. Freibauer, P. Ciais, P. Smith, G. J. Nabuurs, G. Folberth, B. Schlamadinger, R. W. A. Hutjes, R. Ceulemans, E. D. Schulze, R. Valentini, and A. J. Dolman (2003b), Europe's terrestrial biosphere absorbs 7 to 12% of European anthropogenic CO2 emissions, *Science*, *300*, 1538-1542.

Kaminski, T., M. Heimann, and R. Giering (1999), A coarse grid three-dimensional global inverse model of the atmospheric transport - 1. Adjoint model and Jacobian matrix, *J. Geophys. Res.*, *104*, 18535-18553.

Karstens, U., U. Gamnitzer, and I. Levin (2005), Evaluation of CO and SF6 as quantitative tracers for fossil fuel co2: the modeler's view, paper presented at 7th International Carbon Dioxide Conference, Colorado, USA, 25-30 Sept, 2005.

Kesselmeier, J., and L. Merk (1993), Exchange Of Carbonyl Sulfide (Cos) Between Agricultural Plants And The Atmosphere - Studies On The Deposition Of Cos To Peas, Corn And Rapeseed, *Biogeochemistry*, *23*, 47-59.

Kettle, A. J., U. Kuhn, M. von Hobe, J. Kesselmeier, and M. O. Andreae (2002a), Global budget of atmospheric carbonyl sulfide: Temporal and spatial variations of the dominant sources and sinks, *Journal Of Geophysical Research-Atmospheres*, *107*.

Kettle, A. J., U. Kuhn, M. von Hobe, J. Kesselmeier, P. S. Liss, and M. O. Andreae (2002b), Comparing forward and inverse models to estimate the seasonal variation of hemisphere-integrated fluxes of carbonyl sulfide, *Atmos. Chem. Phys.*, *2*, 343-361.

Kjellström, E. (1998), A three-dimensional global model study of carbonyl sulfide in the troposphere and lower stratosphere, *Journal of Atmospheric Chemistry*, *29*, 151-177.

Kluczewski, S. M., K. A. Brown, and J. N. B. Bell (1985), Deposition of [35S]-carbonyl sulphide to vegetable crops, *Radiation Protection Dosimetry*, *11*, 173-177.

Law, R. M., W. Peters, and C. Rodenbeck (2005), Protocol for TransCom continuous data experiment, TransCom.

Levin, I., B. Kromer, M. Schmidt, and H. Sartorius (2003), A novel approach for independent budgeting of fossil fuel CO_2 over Europe by $^{14}CO_2$ observations, *Geophys. Res. Lett.*, *30*, 2194.

Levin, I., J. Schuchard, B. Kromer, and K. O. Munnich (1989), The Continental European Suess Effect, *Radiocarbon*, *31*, 431-440.

Lin, J. C., and C. Gerbig (2005), Accounting for the effect of transport errors on tracer inversions, *Geophys. Res. Lett.*, *32*.

Lin, J. C., C. Gerbig, S. Wofsy, A. E. Andrews, B. C. Daube, K. Davis, and C. A. Grainger (2003), A near-field tool for simulating the upstream influence of atmospheric observations: The Stochastic Time-Inverted Lagrangian Transport (STILT) model, *J. Geophys. Res.*, *108*.

Lin, J. C., C. Gerbig, S. C. Wofsy, A. E. Andrews, B. C. Daube, C. A. Grainger, B. B. Stephens, P. S. Bakwin, and D. Y. Hollinger (2004), Measuring fluxes of trace gases at regional scales by Lagrangian observations: Application to the CO_2 Budget and Rectification Airborne (COBRA) study, *J. Geophys. Res.*, *109*, doi:10.1029/2004JD004754.

Lindroth, A., A. Grelle, and A. S. Moren (1998), Long-term measurements of boreal forest carbon balance reveal large temperature sensitivity, *Global Change Biol.*, *4*, 443-450.

Lobert, J. M., D. H. Scharffe, T. A. Kuhlbusch, R. Seuwen, and P. J. Crutzen (Eds.) (1991), *Experimental evaluation of biomass burning emissions: Nitrogen and carbon containing compounds*, 289–304 pp., MIT Press, Cambridge, Mass., USA.

Matross, D. M., A. Andrews, M. Pathmathevan, C. Gerbig, J. C. Lin, S. C. Wofsy, B. C. Daube, E. W. Gottlieb, V. Y. Chow, J. T. Lee, C. L. Zhao, P. S. Bakwin, J. W. Munger, and D. Y. Hollinger (2006), Estimating regional carbon exchange in New England and Quebec by combining atmospheric, ground-based and satellite data, *Tellus Series B-Chemical and Physical Meteorology*, *58*, 344-358.

Michalak, A. M., L. Bruhwiler, and P. P. Tans (2004), A geostatistical approach to surface flux estimation of atmospheric trace gases, *J. Geophys. Res.*, *109*, D14109.

Michalak, A. M., A. Hirsch, L. Bruhwiler, K. R. Gurney, W. Peters, and P. P. Tans (2005), Maximum likelihood estimation of covariance parameters for Bayesian atmospheric trace gas surface flux inversions, *J. Geophys. Res.*, *110*.

Montzka, S. A., B. Hall, J. W. Elkins, L. Miller, A. Watson, C. Sweeney, and P. P. Tans (In Press), On the global distribution, seasonality, and budget of atmospheric carbonyl sulfide (COS) and some similarities to CO2, *J. Geophys. Res.*

National Academy of Sciences (2001), *Climate Change Science: As Analysis of Some Key Questions*, National Academy Press, Washington, DC.

Olivier, J. G., J. Bouwman, A. F. , C. W. M. Van der Maas, J. J. M. Berdowski, C. Veldt, J. P. J. Bloos, A. J. H. Visschedijk, P. Y. J. Zandyelt, and J. L. Haverlag (1996), Description of EDGAR Version 2.0. A set of global emission inventories of greenhouse gases and ozone-depleting substances for all anthropogenic and most natural sources on a per country basis and on 1 x 1 grid, Natl. Inst. for Public Health and the Environ., Bilthoven, the Netherlands.

Pacala, S. W., G. C. Hurtt, D. Baker, P. Peylin, R. A. Houghton, R. A. Birdsey, L. Heath, E. T. Sundquist, R. F. Stallard, P. Ciais, P. Moorcroft, J. P. Caspersen, E. Shevliakova, B. Moore, G. Kohlmaier, E. Holland, M. Gloor, M. E. Harmon, S.-M. Fan, J. L. Sarmiento, C. L. Goodale, D. Schimel, and C. B. Field (2001), Consistent land- and atmosphere-based U.S. carbon sink estimates, *Science*, *292*, 2316-2320.

Palmer, P. I., P. Suntharalingam, D. B. A. Jones, D. J. Jacob, D. G. Streets, F. Qingyan, S. Vay, and G. W. Sachse (2006), Exploiting CO2:CO correlations to improve inverse analyses of carbon fluxes, *J. Geophys. Res.*

Palmer, P. I., P. Suntharalingam, D. B. A. Jones, D. J. Jacob, D. G. Streets, F. Qingyan, S. Vay, and G. W. Sachse (In review), Exploiting CO2:CO correlations to improve inverse analyses of carbon fluxes.

Peters, W., M. C. Krol, E. J. Dlugokencky, F. J. Dentener, P. Bergamaschi, G. Dutton, P. van Velthoven, J. B. Miller, L. Bruhwiler, and P. P. Tans (2004), Toward regional-scale modeling using the two-way nested global model TM5: Characterization of transport using SF6, *J. Geophys. Res.*, *109*, doi:10.1029/2004JD005020.

Pfister, G., P. G. Hess, L. K. Emmons, J.-F. Lamarque, C. Wiedinmyer, D. P. Edwards, G. Pétron, J. C. Gille, and G. W. Sachse (2005), Quantifying CO emissions from the 2004 Alaskan wildfires using MOPITT CO data, *J. Geophys. Res.*, *32*, doi:10.1029/2005GL022995.

Potosnak, M. J., S. C. Wofsy, S. A. Denning, T. J. Conway, J. W. Munger, and D. H. Barnes (1999), Influence of biotic exchange and combustion sources on atmospheric CO_2 concentrations in New England from observations at a forest flux tower, *J. Geophys. Res.*, *104*, 9561-9569.

Potter, C. S., J. T. Randerson, C. B. Field, P. A. Matson, P. M. Vitousek, H. A. Mooney, and S. A. Klooster (1993), Terrestrial Ecosystem Production - a Process Model-Based on Global Satellite and Surface Data, *Global Biogeochem. Cy.*, *7*, 811-841.

Protoschill-Krebs, G., and J. Kesselmeier (1992), Enzymatic pathways for the metabolization of carbonyl suphide (COS) by higher plants, *Botanica Acta*, *105*, 206-212.

Protoschill-Krebs, G., C. Wilhelm, and J. Kesselmeier (1996), Consumption of carbonyl sulphide (COS) by higher plant carbonic anhydrase (CA), *Atmos. Environ.*, *30*, 3151-3156.

Randerson, J. T., M. V. Thompson, C. M. Malmstrom, C. B. Field, and I. Y. Fung (1996), Substrate limitations for heterotrophs: Implications for models that estimate the seasonal cycle of atmospheric CO2, *Global Biogeochem. Cy.*, *10*, 585-602.

Rodgers, C. D. (2000), *Inverse methods for atmospheric sounding: theory and practice*, 238 pp., World Scientific, Singapore.

Sachse, G. W., G. F. Hill, L. O. Wade, and M. G. Perry (1987), Fast-response, high-precision carbon-monoxide sensor using a tunable diode-laser absorption technique, *J. Geophys. Res.*, *92*, 2071–2081.

Sandoval-Soto, L., M. Stanimirov, M. von Hobe, V. Schmitt, J. Valdes, A. Wild, and J. Kesselmeier (2005), Global uptake of carbonyl sulfide (COS) by terrestrial vegetation: Estimates corrected by deposition velocities normalized to the uptake of carbon dioxide (CO2), *Biogeosciences*, *2*, 125-132.

Sandu, A. (2006), Targeted observations for atmospheric chemistry and transport models, in *Computational Science - Iccs 2006, Pt 1, Proceedings*, edited, pp. 712-719.

Sandu, A., D. N. Daescu, G. R. Carmichael, and T. Chai (2005), Adjoint sensitivity analysis of regional air quality models, *Journal of Computational Physics*, *204*, 222.

Sarmiento, J. L., and S. C. Wofsy (1999), A U.S. Carbon Cycle Science Plan, 69 pp, U.S. Global Change Research Program, Washington, DC.

Schifter, I., C. Gonzalez-Macias, A. Miranda, and E. Lopez-Salinas (2005), Air emissions assessment from offshore oil activities in Sonda de Campeche, Mexico, *Environmental Monitoring and Assessment*, *109*, 135-145.

Sellers, P. J., D. A. Randall, G. J. Collatz, J. A. Berry, C. B. Field, D. A. Dazlich, C. Zhang, D. G. Collelo, and L. Bounoua (1996a), A revised land surface parameterization

(SiB2) for atmospheric GCMs. Part I: Model Formulation, *Journal of Climate*, *275*, 502-509.

Sellers, P. J., D. A. Randall, G. J. Collatz, J. A. Berry, C. B. Field, D. A. Dazlich, C. Zhang, G. D. Collelo, and L. Bounoua (1996b), A revised land surface parameterization (SiB2) for atmospheric GCMs .1. Model formulation, *Journal of Climate*, *9*, 676-705.

Singh, H. B., L. Salas, D. Herlth, R. Kolyer, E. Czech, W. Viezee, Q. Li, D. J. Jacob, D. Blake, G. W. Sachse, C. N. Harward, H. Fuelberg, C. M. Kiley, Y. Zhao, and Y. Kondo (2003), In situ measurements of HCN and CH_3CN over the Pacific Ocean: Sources, sinks, and budgets, *J. Geophys. Res.*, *108*, 8795, doi:8710.1029/2002JD003006.

Streets, D. G., T. C. Bond, G. R. Carmichael, S. D. Fernandes, Q. Fu, D. He, Z. Klimont, S. M. Nelson, N. Y. Tsai, M. Q. Wang, J. H. Woo, and K. F. Yarber (2003), An inventory of gaseous and primary aerosol emissions in Asia in the year 2000, *J. Geophys. Res.*, *108*.

Suntharalingam, P., D. J. Jacob, P. I. Palmer, J. A. Logan, R. M. Yantosca, Y. P. Xiao, M. J. Evans, D. G. Streets, S. L. Vay, and G. W. Sachse (2004), Improved quantification of Chinese carbon fluxes using CO2/CO correlations in Asian outflow, *J. Geophys. Res.*, *109*.

Takahashi, T., R. H. Wanninkhof, R. A. Feely, R. F. Weiss, D. W. Chipman, N. Bates, J. Olafsson, C. Sabine, and S. C. Sutherland (1999), Net sea-air CO_2 flux over the global oceans: An improved estimate based on the sea –air pCO_2 difference, paper presented at 2nd CO_2 in Oceans Symposium, Cent. for Global Environ. Res. Natl. Inst. for Environ. Stud., Tsukuba, Japan.

Tang, Y., G. R. Carmichael, and T. Chai (In Press), The Influence of Lateral and Top Boundary Conditions on Regional Air Quality Prediction: a Multi-Scale Study Coupling Regional and Global Chemical Transport Models, *J. Geophys. Res.*

Tang, Y. H., G. R. Carmichael, L. W. Horowitz, I. Uno, J. H. Woo, G. Kurata, B. Lefer, R. E. Shetter, H. Huang, B. E. Anderson, M. A. Avery, A. D. Clarke, and D. R. Blake (2003), Impacts of aerosols and clouds on photolysis frequencies and photochemistry during TRACE-P: 2. Three dimensional study using a regional chemical transport model, *J. Geophys. Res.*, *108*, 8822.

Tang, Y. H., G. R. Carmichael, J. H. Seinfeld, D. Dabdub, R. J. Weber, B. Huebert, A. D. Clarke, S. A. Guazzotti, D. A. Sodeman, K. A. Prather, I. Uno, J. H. Woo, J. J. Yienger, D. G. Streets, P. K. Quinn, J. E. Johnson, C. H. Song, V. H. Grassian, A. Sandu, R. W. Talbot, and J. E. Dibb (2004), Three-dimensional simulations of inorganic aerosol distributions in east Asia during spring 2001, *J. Geophys. Res.*, *109*, doi:10.1029/2004JD005373.

Tans, P. P., I. Y. Fung, and T. Takahashi (1990), Observational constraints on the global atmospheric CO_2 budget, *Science*, *247*, 1431 - 1439.

Thacker, W. C. (1987), Three lectures on fitting numerical models to observations, 64 pp, GKSS.

Turnbull, J. C., J. B. Miller, S. J. Lehman, P. P. Tans, R. J. Sparks, and J. Southon (2006), Comparison of $^{14}CO_2$, CO, and SF_6 as tracers for recently added fossil fuel CO_2 in the atmosphere and implications for biological CO_2 exchange, *Geophys. Res. Lett.*, *33*, doi:10.1029/2005GL024213.

UKOOA (1998), United Kingdom Offshore Operators Association website, edited.

Valentini, R., G. Matteucci, A. J. Dolman, E. D. Schulze, C. Rebmann, E. J. Moors, A. Granier, P. Gross, N. O. Jensen, K. Pilegaard, A. Lindroth, A. Grelle, C. Bernhofer, T. Grunwald, M. Aubinet, R. Ceulemans, A. S. Kowalski, T. Vesala, U. Rannik, P. Berbigier, D. Loustau, J. Guomundsson, H. Thorgeirsson, A. Ibrom, K. Morgenstern, R. Clement, J. Moncrieff, L. Montagnani, S. Minerbi, and P. G. Jarvis (2000), Respiration as the main determinant of carbon balance in European forests, *Nature*, *404*, 861-865.

Vay, S. A., J.-H. Woo, B. E. Anderson, K. L. Thornhill, D. R. Blake, D. J. Westberg, C. M. Kiley, M. A. Avery, G. W. Saschse, D. G. Streets, Y. Tsutsumi, and S. R. Nolf (2003), Influence of regional-scale anthropogenic emissions on CO_2 distributions over the western North Pacific, *J. Geophys. Res.*, *108*, 8801, doi:8810.1029/2002JD003094.

Vose, J. M., and M. G. Ryan (2002), Seasonal respiration of foliage, fine roots, and woody tissues in relation to growth, tissue N, and photosynthesis, *Global Change Biol.*, *8*, 182-193.

Watts, S. F. (2000), The mass budgets of carbonyl sulfide, dimethyl sulfide, carbon disulfide and hydrogen sulfide, *Atmos. Environ.*, *34*, 761.

Wofsy, S. S., and R. C. Harris (2002), North American Carbon Plan (NACP). Report of the NACP Committee of the U.S. Interagency Carbon Cycle Science Program, US Global Change Research Program, Washington, DC.

WWF (1999), World Wildlife Fund Ecoregions, *ESRI Data & Maps 2000 Edition*.

Xu, X., H. G. Bingemer, and U. Schmidt (2002), The flux of carbonyl sulfide and carbon disulfide between the atmosphere and a spruce forest, *Atmos. Chem. Phys.*, *2*, 171-181.

Zhu, C., R. H. Byrd, and J. Nocedal (1997), L-BFGS-B-fortran routines for large scale bound constrained optimization, *ACM Trans. Math. Software*, *23*, 550-560.

Zondervan, A., and J. A. J. Meijer (1996), Isotopic characterisation of CO_2 sources during regional pollution events using isotopic and radiocarbon analysis, *Tellus*, *48B*, 601-612.

APPENDIX: COMPARISON OF REGRESSION COEFFICIENT AND GIS-BASED METHODOLOGIES FOR REGIONAL ESTIMATES OF FOREST SOIL CARBON STOCKS

J. Elliott Campbell[a], Jeremie C. Moen[a], Richard A. Ney[b], Jerald L. Schnoor[a]

[a]Center for Global and Regional Environmental Research, University of Iowa, Iowa City, IA 52242, USA

[b]Sebesta Blomberg & Associates, Inc., North Liberty, IA 52317 USA

Abstract

Estimates of forest soil organic carbon (SOC) have applications in carbon science, soil quality studies, carbon sequestration technologies, and carbon trading. Forest SOC has been modeled using a regression coefficient methodology that applies mean SOC densities (mass/area) to broad forest regions. A higher resolution model is based on an approach that employs a geographic information system (GIS) with soil databases and satellite-derived landcover images. Despite this advancement, the regression approach remains the basis of current state and federal level greenhouse gas inventories. Both approaches are analyzed in detail for Wisconsin forest soils from 1983 to 2001, applying rigorous error-fixing algorithms to soil databases. Resulting SOC stock estimates are 20 percent larger when determined using the GIS method rather than the regression approach. Average annual rates of increase in SOC stocks are 3.6 and 0.9 million metric tons of carbon per year for the GIS and regression approaches respectively.

1. Introduction

Estimates of the mass of forest soil organic carbon (SOC) are applied to determine long-term carbon fluxes, to manage natural resources and to design carbon sequestration strategies. Several approaches to estimating these forest SOC stocks are currently in use and may provide conflicting results.

One method for estimating forest SOC stocks is a regression approach in which regional SOC densities (mass SOC/area) are a function of temperature, precipitation, age class, and land-use history for different ecosystems (Post et al., 1982; Birdsey, 1992). These densities are estimated for broad regions as shown in Table A1. SOC stocks are then calculated by multiplying the SOC densities by annual forest areas. Annual forest area data is available from field inventory surveys by the U.S. Department of Agriculture (USDA) Forest Service and recorded in the Forest Inventory and Analysis (FIA) database. Further adjustments to the stock estimates can also be made based on assumptions of changes in land cover over time.

Table A1. Estimated soil organic carbon density for regional forests in the U.S. (Post et al., 1982).

Region	**Soil organic carbon (kg/m^2)**
Southeast	7.74
South Central	7.58
Northeast	16.21
Mid-Atlantic	11.56
North Central	13.09
Central	8.33
Rocky Mountain	8.02
Pacific Coast	9.77

This regression methodology has been used to create regional and national forest carbon estimates for the United States (Birdsey and Lewis, 2000, Heath and Birdsey, 1993, Plantinga and Birdsey, 1993, Turner et al., 1995). This method is also currently applied in state (Franco, 2002, Kerr, 2004) and federal (EPA, 2004) greenhouse gas inventories. The regression method is prescribed in the U.S. EPA's Emission Inventory Improvement Program (EIIP) which develops preferred methods for state and territory level emission inventories (EIIP, 2005). This is also the case for U.S. federal emissions inventories which were instructional to the EIIP (EPA, 2004).

An updated methodology for estimating SOC stocks applies a geographic information system (GIS) to calculate SOC densities for each forest type within a region using the USDA soil databases and satellite-derived land cover images (Heath et al., 2002). Regional SOC stocks are estimated by multiplying these densities by forest type areas from the FIA database. The use of soils databases makes the GIS method more data intensive than the regression approach. The stock estimates are then adjusted based on assumptions of rates of change in stocks due to changes in land cover. The GIS-based SOC estimates have been the preferred methodology for recent studies (Amichev B. Y. and Galbraith, 2003, Heath et al., 2003b, Johnson and Kern, 2003, Ney et al., 2002).

A quantitative study of the errors of these two methods has not been performed due to a lack of sufficient validation data at regional scales. In the future, regional measurements of SOC may be available from the USDA Forest Service and could be used to determine the accuracy of the two approaches. Although it is not yet possible to determine which approach is more accurate, there is much to be learned by comparing the results of the two approaches. The disparity between methods provides information about the uncertainty of our understanding of SOC stocks and a caveat to using these methods interchangeably. Furthermore a large difference between these methods would provide a strong motivation for examining the accuracy of these methods with forthcoming regional SOC measurements.

While a comparison of the regression- and GIS-based methods for estimating forest SOC has not previously been completed, related studies indicate the potential for large differences. The results of a study of the northeastern U.S. indicates that the GIS method produced between 8 and 30 percent higher SOC densities than a coarse scale method based on the FAO/UNESCO Soil Map of the World (Davidson and Lefebvre, 1993). A study of soils in the western U.S. found area-weighted average SOC densities of 13.8 kg/m2 (depth of 1 meter) for a related GIS-based method and 12.1 kg/m2 for a Soil Map of the World-based approach (Homann et al., 1998). These differences in densities are important because a small percent error in the densities used to calculate stocks may result in a much larger percent error in the annual change in stocks.

The objective of our study is to compare the GIS and regression methods for estimating forest SOC stocks and annual rates of change in stocks. These results are highly relevant for ongoing application of both approaches and for future regional SOC measurements that can be used to estimate the absolute error of each method. The GIS-based methods are applied for the state of Wisconsin and compared with previously published regression-based SOC estimates. Wisconsin provides an ideal study domain because the Wisconsin forestlands are a major focus of forest carbon cycle studies (e.g. Burrows et al., 2002; Davis et al. 2003). In addition, this paper provides a thorough analysis of recent developments in the GIS approach and detailed SOC results for Wisconsin forestlands.

2. Methods

2.1 Study area

Our study region comprises forestlands in the state of Wisconsin, which account for over 40 percent of the total state area. Forest types of maple-beech-birch, aspen-

birch, and oak-hickory comprise the majority of the forest area. Forest data is available from the USDA Forest Service and Wisconsin Department of Natural Resources for 1983, 1996, and 2001. Wisconsin forest areas have been increasing since the 1970's (Schmidt, 1997), primarily due to a transition from marginal agricultural land use to forestland. Some areas of decreasing forestland were found in the southeast due to urban and suburban development. Field methods for survey data applied in this paper were similar between survey years, making inter-annual comparisons appropriate.

2.2 GIS Method

We developed a model with GIS and Visual Basic scripts to apply the most updated methods for estimating forest SOC stocks within our study domain. The model automates SOC calculations which are based on geospatial data including USDA soil databases, USDA Forest Service data from inventory field measurements, and a land cover map of North American forest types. The model process follows the sequential steps of (i) soil data error fixing; (ii) calculation of statewide baseline SOC density; (iii) calculation of SOC densities by forest type; (iv) calculation of annual carbon stocks based on forest type SOC densities and forest type areas; and (v) area weighted statistical analysis of results (Figure A1).

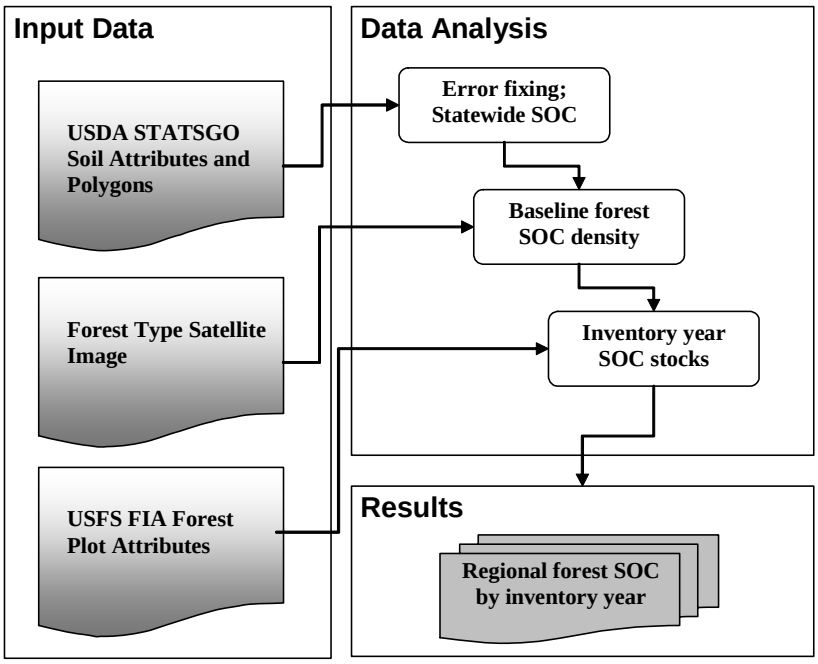

Figure A1. Process diagram for forest SOC estimation with GIS and Visual Basic scripts.

The error fixing and statewide SOC calculations were implemented using the STATSGO (State Soil Geographic) database of geospatial soils data from the USDA Natural Resources Conservation Service (NSSC, 1994). The soil attributes used in calculations of SOC were bulk density, percent organic matter, and percent of rock fragments of different sizes. This data was derived from field surveys completed over the last 50 years and is composed of mapunits with a minimum area of 625 hectares.

The first step in the GIS method is updating invalid STATSGO data. A variety of methods have been demonstrated for error fixing. Minimum values have been required for bulk density and organic matter (Bliss et al., 1995, Davidson and Lefebvre, 1993). Null values have been replaced with estimates that are a function of data in the soil layers above the layers with missing data (Homann et al., 1998). Null values have also been replaced with data from adjacent layers with related soil types (Lacelle et al., 2001). Null and zero values have been updated based on groupings of soil order, Major Land

Resource Area (MLRA), layer number, and texture (Amichev B. Y. and Galbraith, 2003). Our error fixing approach was based on the latter algorithm with the following notable exception.

After the data errors are corrected, the statewide SOC densities were calculated with nested queries at the soil mapunit, component, and layer levels. Our calculations incorporated layer data to 1 meter depth. The 0- to 1-meter layer is thought to include most of the SOC mass in a soil column. The SOC density for each mapunit was calculated as follows (Bliss et al., 1995, Davidson and Lefebvre, 1993)

$$C_S = \sum_j \left\{ COMPPCT_j \cdot \sum_i \left[H_{i,j} \cdot BD_{i,j} \cdot OM_{i,j} \cdot FE_{i,j} \cdot U / 1.724 \right] \right\} \quad (1)$$

where Cs is the SOC density for mapunit S (metric tons/ha), H is the soil layer thickness (cm), BD is the average bulk density (g/cm3), OM is the average organic matter content (percent by weight), FE is the fraction of fine earth material (<2 mm), COMPPCT is the percentage (by area) of a component within a map unit (percent), 1.724 is the fraction of carbon content to organic matter by weight (Nelson and Sommers, 1982), i is the soil layer index, j is the component index, and S is the mapunit index.

We included mineral soils and organic soils (Histosols) in our STATSGO baseline calculations because land that is classified as forestland can contain small areas of wetlands. Some Histosols will be outside of forestland, which can cause results to be larger than the true value.

The statewide SOC densities, described above, were converted into forest type SOC densities by overlaying satellite land use imagery over the map of STATSGO mapunit SOC densities. We used a forest-type map derived from Advanced Very High Resolution Radiometer (AVHRR) composite images at 1 km resolution that portrays 25 classes of forest types, recorded during the 1991 growing season (Zhu and Evans, 1994). While a Landsat land cover data set is also available for Wisconsin (WDNR, 1998), we

use the AVHRR data because the forest type classification in the AVHRR data corresponds with the forest types in the FIA data set. The statewide SOC density map was converted to a gridded map and overlayed on the AVHRR gridded map in order to calculate the area weighted mean SOC density for each forest type.

The forest type SOC densities were then used to calculate annual SOC stocks by multiplying the densities by forest area data at the county level from the FIA database for 1983, 1996, and 2001. Further modification of the SOC stocks can be made using the land cover transition and land management assumptions synthesized in the national level FORCARB model (Heath et al., 2002). This requires additional input on changes in land use and management that can be obtained from the USDA Natural Resources Conservation Service's (NRCS) National Resources Inventory. However, the NRI data for Wisconsin are not statistically reliable at the county scale (Goerg, Personal communication). In addition, a meta-analysis of the assumptions on SOC dynamics from land use and management transitions indicates mixed empirical results (Johnson and Curtis, 2001). The analysis in this Wisconsin forest study reflects changes in areas of forest types, but not assumptions of SOC dynamics from land use and management transitions.

2.3 Regression Method

Regression estimates of SOC stocks for 1987, 1992, and 1997 for Wisconsin were obtained from a national inventory of state forest carbon (Birdsey and Lewis, 2000). A single SOC density is estimated for the entire North Central region as a function of regional temperature, precipitation, age class, and land-use history (Birdsey, 1992). SOC stocks are determined by multiplying the SOC densities by annual forest areas from the FIA. The published stocks were interpolated by Birdsey and Lewis (2000) from FIA

inventory years to the years 1987, 1992, and 1997 in order to compare SOC stocks between states with different inventory years.

These regression based stocks for Wisconsin are the same results presented in the most recent Wisconsin greenhouse gas inventory (Kerr, 2004). The regression method is closely related to the method in the EIIP. The notable exception is that the EIIP guidelines indicate that the annual rates of change in SOC stocks should be estimated by multiplying regression-based SOC densities by FIA forest area data for different years and fitting a line to the data. The results from Birdsey and Lewis (2000) go a step further to estimate changes in SOC between inventory years based on assumptions of SOC changes due to different land use transitions and land management.

3. Results and discussion

3.1 GIS-based results

3.1.1 Data update

Missing and invalid data were found and updated in 32 percent of all mapunits. The missing and invalid data were primarily in attribute variables associated with fraction of fine earth materials including weight percent of rock fragment 3 to 10 inches in size (INCH3), weight percent greater than 10 inches in size (INCH10), and percent of fragments passing a number-10 sieve (NO10) as shown in Table A2. Map units with invalid data were relatively evenly distributed in space across the study domain as shown for the INCH10 data in Figure A2.

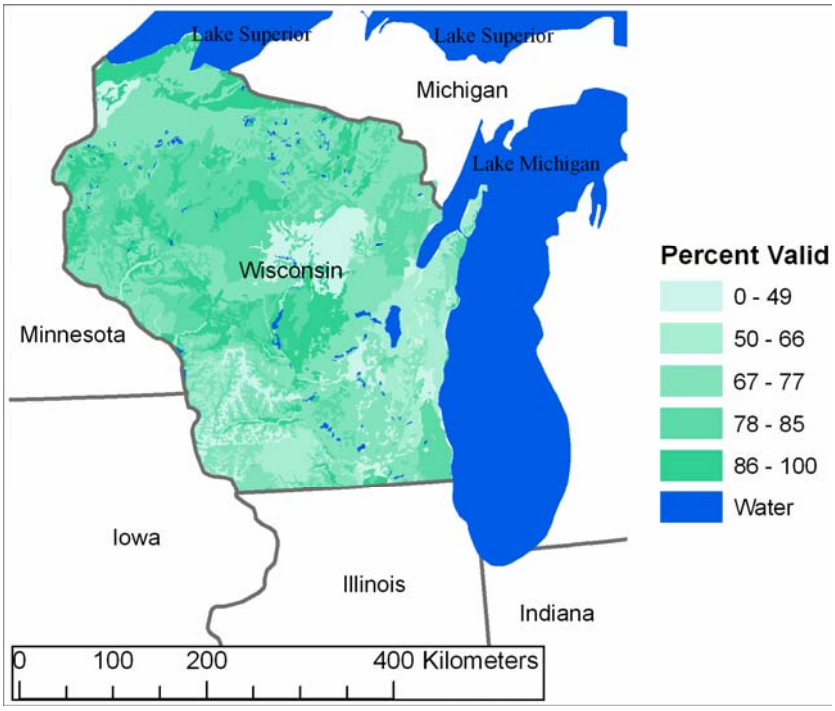

Figure A2. Percent of valid data for each STATSGO map unit for the soil attribute for weight percent of rock fragments greater than 10 inches in size (INCH10).

Table A2. Percent of Wisconsin layer records found to be valid, invalid, and null for STATSGO attributes used in the SOC calculations including weight percent 3 to 10 inches (INCH3), weight percent greater than 10 inches (INCH10), percent passing a number 10 sieve (NO10), organic matter (OM), and bulk density (BD).

	INCH3	INCH10	NO10	OM	BD
Valid	91.00%	73.70%	89.40%	99.90%	99.90%
Invalid	3.60%	9.00%	0.00%	0.10%	0.10%
Null	5.30%	17.30%	10.60%	0.00%	0.00%

3.1.2 Statewide SOC estimates

Statewide SOC density results are shown in Figure A3 by mapunit (Figure A3a) and county (Figure A4b). Densities for depths up to 1 m range from 0.5 kg/m2 in soil components with unweathered bedrock and stony texture to 92.1 kg/m2 in muck and peat soils. The area weighted mean density for all of Wisconsin soils is calculated as 14.2 kg/m2. Using the same GIS methodology for all depths resulted in an area weighted

mean of 17.6 kg/m2. This larger result is comparable to an average Wisconsin SOC value of 17.2 kg/m2 from a previous study in which data was neglected for all layers below layers with missing or null values (Bliss et al., 1995).

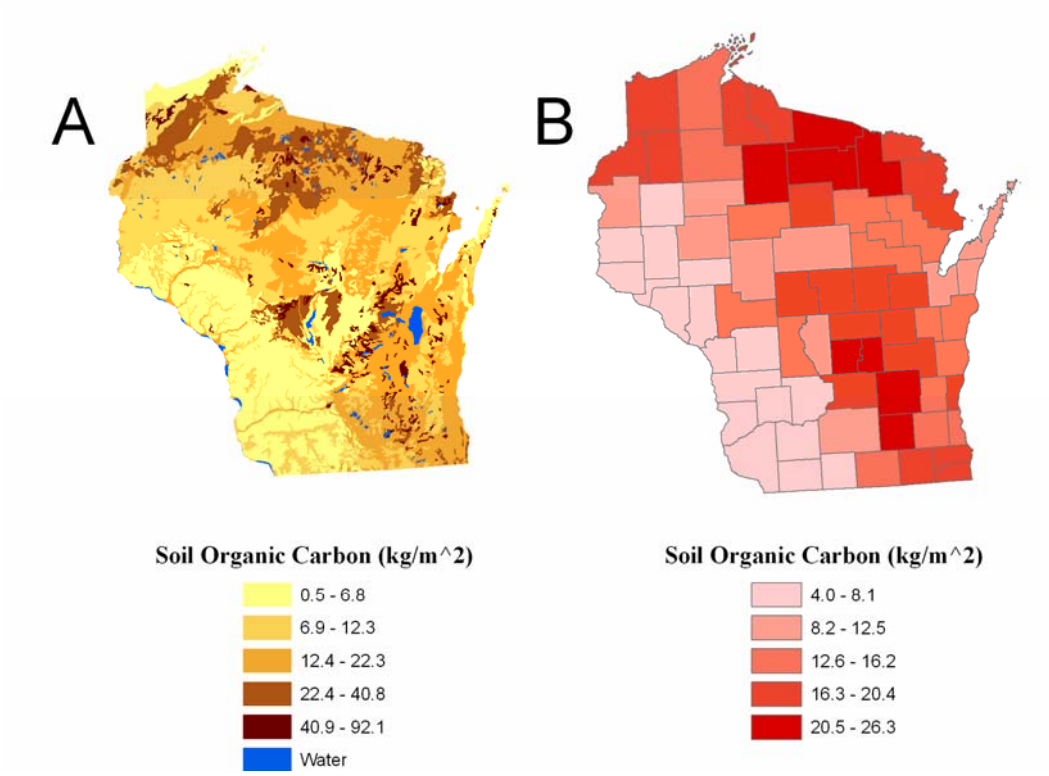

Figure A3. Soil Organic Carbon densities (kg/m2) for depth to 1 meter by map unit (a) and area weighted average densities for counties (b).

3.1.3 Baseline forest type SOC estimates

Baseline forest type SOC densities, obtained from the overlay of forest type and statewide SOC maps, are summarized in Table A3. The ratio of the area weighted mean to the area weighted standard deviations are similar in magnitude to related results for the southeastern U.S. (Heath et al., 2002). A comparison of the Wisconsin mean SOC densities by forest type with the SOC densities from the southeastern U.S. study is also

provided in Table A3. Densities from the Wisconsin and the southeastern U.S. are of the same order of magnitude; however, oak-hickory and maple-beech-birch forests appear to be associated with higher SOC soils in Wisconsin while spruce-fir and aspen-birch are associated with higher SOC soils in the more general region. Overall the forest SOC densities are higher in Wisconsin, with area weighted means of 16.4 kg/m2 and 11.7 kg/m2 for forests in Wisconsin and the southeastern U.S., respectively.

Table A3. Wisconsin forest type SOC density means and standard deviations in comparison with mean SOC densities for the southeastern U.S. region.

Forest Type	Wisconsin SOC (kg/m^2)	Wisconsin Standard Deviation	Southeastern U.S. SOC (kg/m^2)[1]
White-red-jack pine	20.3	14.1	19.6
Spruce-fir	15.6	12.7	19.3
Oak-hickory	14.4	14.7	8.5
Elm-ash-cottonwood	10.2	7.4	11.8
Maple-beech-birch	18.6	13.4	13.9
Aspen-birch	15.7	13.1	23.7

[1]Southeastern U.S. results are from a previous study of SOC using STATSGO and AVHRR satellite imagery (Heath et al., 2002).

The accuracy of the forest type SOC densities depends in part on the classification error in the AVHRR land cover map. Zhu and Evans (1994) reported errors by comparing the AVHRR and FIA based estimates of forest areas for each state. For Wisconsin, the reported difference between the AVHRR and FIA areas was greater than 3%.

3.1.4 Annual forest SOC stocks

Annual forest SOC stocks are calculated for 1983, 1996, and 2001 from baseline forest SOC densities and annual forest type areas. Statewide forest areas and SOC stocks are summarized in Table A4. Total forest area increases by almost 4 percent from 1983 to 2001 while forest SOC stocks increase by over 5 percent. This is due to the large growth of maple-beech-birch forests which have a relatively high SOC density compared to the other forest types. The overall increase in forest soil carbon is consistent with the continental increase in terrestrial carbon stocks inferred from atmospheric inversion and inventory studies (Pacala et al., 2001). It is important to note that a fraction of the increase in forest SOC stocks is due to sequestration of atmospheric carbon dioxide while another fraction is due to the conversion of non-forestlands into forestlands.

Table A4. Statewide areas (1000 hectares) by forest type from FIA database, and calculated soil organic carbon (MMTC).

	Area (1000 ha)			Soil Organic Carbon (MMTC)		
Forest type	1983	1996	2001	1983	1996	2001
White-red-jack pine	519	492	540	106	100	110
Spruce-fir	659	550	522	103	86	82
Oak-hickory	1,175	1,177	1,136	169	170	164
Elm-ash-cottonwood	534	623	548	54	63	56
Maple-beech-birch	1,640	2,167	2,189	304	402	406
Aspen-birch	1,614	1,404	1,437	253	220	225
Total:	6,142	6,412	6,373	989	1,040	1,042

Consideration of the GIS results at the county level demonstrates the spatial heterogeneity in forest SOC stock trends. The changes in stocks (normalized by area), from 1983 to 2001, are shown in Figure A4 by county. Regions of both increasing and decreasing forest SOC stocks exist. The largest decrease in SOC stocks of -29 ton/ha, is in Sheboygan county, where forestland area decreased and developed area increased

during this period. Increases in SOC stocks of over 20 ton/ha are found in the northern counties of Langlade, Manitowoc, Marinette, Vilas, and Iron. These increasing stock trends are consistent with land cover studies showing conversion of marginal agriculture back to forests in northern Wisconsin (e.g. Schmidt, 1997). The reported sampling error for the FIA areas indicates that most counties have less than 25% error, including the counties discussed above.

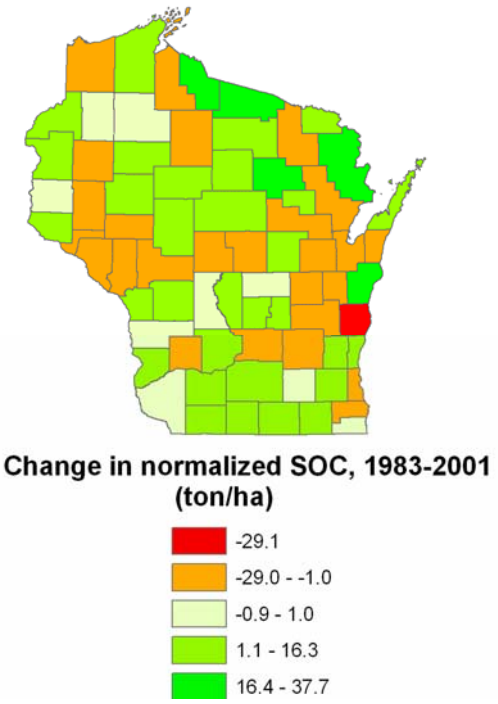

Figure A4. Change in county SOC stocks (metric tons/hectare) over the period 1983 – 2001, normalized by county area.

3.2 Comparison of GIS and Regression Results

Previously published regression-based forest SOC results are compared with the GIS estimates described above. The regression results are based on a single regional SOC density for the North Central region of the U.S. with a value of 13.09 kg/m2 (Table

A1). The GIS method densities range from 10.2 kg/m2 to 20.3 kg/m2 for different forest types (Table A3). The area weighted average density for the GIS method of 16.4 kg/m2 is considerably larger than the regression SOC density.

In Figure A5, the trends for SOC stocks from both methods show increasing forest stocks and relatively small variations in the annual rates of change. The forest SOC stocks are much larger when calculated from the GIS method than the regression approach as expected by the difference in SOC density estimates from both methods. Stocks for the GIS approach are approximately 20 percent larger than stocks derived from the regression approach. The regression approach may underestimate the SOC density and stocks relative to the GIS method due to the fact that the regression-derived SOC density is applied to a multi-state region in which Wisconsin has some of the largest SOC concentrations (Johnson and Kern, 2003).

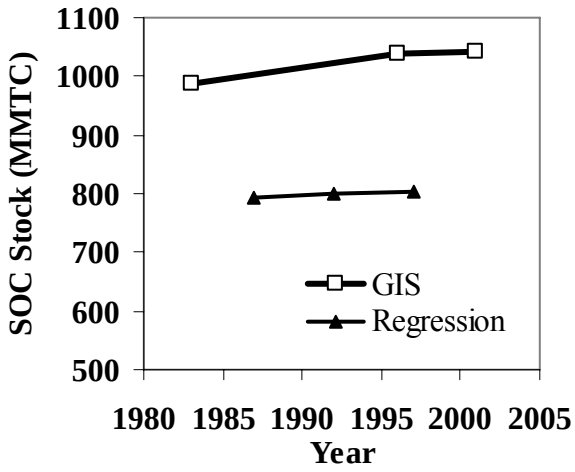

Figure A5. Annual SOC stocks for Wisconsin forestlands based on the GIS method (squares) and the regression method (triangles).

Average annual rates of stock growth are compared by linearly interpolating in time the GIS results to the same years as the published regression stocks. The average

annual growth rates are 3.6 and 0.9 million metric tons of carbon per year for the GIS and regression approaches respectively (Table A5). The large disparity between methods in the calculated annual rates of change is due to the fact that changes in SOC stocks from year to year are small relative to the change in stock. A small error in SOC stocks translates to a very large difference in the annual rates of change. The difference between the methods is much more significant for applications of rates of changes in stocks than applications of the magnitude of the stocks.

Table A5. Forest SOC stocks (million metric tons of carbon) and average annual change by GIS- and regression-based methods[1].

	SOC Stocks (MMTC)			Average annual change (MMTC/yr)		
Year	1987	1992	1997	1987-1992	1992-1997	1987-1997
GIS results	1,005	1,025	1,041	4	3.2	3.6
Regression results	794	799	804	0.9	0.9	0.9

[1]Regression-based results for Wisconsin are from a national study of U.S. forests (Birdsey and Lewis, 2000).

4. Conclusions

The analysis of two SOC models shows large differences in results for stocks and annual rates of change in stocks when applied to recent forestland data for Wisconsin. It is not yet possible to test which approach is more accurate because SOC measurements at the appropriate regional scales are not yet available. However, the results do show large differences in the methods and the important conclusions that follow are: (1) the methodologies should not be used interchangeably; (2) the differences in methodologies provide information about the uncertainty of our current understanding of SOC stocks and annual changes in stocks; and (3) the direct measurements of SOC in future USDA

Forest Service inventories should be used to examine the absolute errors of both approaches.

If the regression approach were found to be more accurate, then the GIS approach could be improved by incorporating more of the independent variables that the regression approach is based on such as precipitation and temperature. On the other hand, if the more current data and finer resolution of the GIS approach provides greater accuracies, then the regression based results that are used in greenhouse gas inventories could be incorporating large errors into greenhouse gas policy. In the most recent Wisconsin greenhouse gas inventory, the reported net anthropogenic greenhouse gas emissions were decreased by 17% when forest soil and biomass sequestration was added to the analysis (Kerr, 2004). Had the larger GIS-based estimates of annual stock growth been applied, then the Wisconsin report would have found a larger decrease in net emissions when forest sequestration was considered.

Acknowledgments

We thank Norman Bliss of the USGS for providing feedback on the STATSGO database analysis as well as Beyhan Amichev from Virginia Polytechnic Institute and State University for details on error updating algorithms. This work was supported by a grant from the Energy Center of Wisconsin.

References

Amichev, B.Y., Galbraith, J.M., 2003. A revised methodology for estimation of forest soil carbon from spatial soils and forest inventory datasets. Environmental Management 33 (Supplement 1), S74-S86.

Birdsey, R.A., 1992. Carbon Storage and accumulation in the United States forest ecosystems. WO-59, USDA Forest Service.

Birdsey, R.A., Lewis, G.M., 2000. Carbon in United States forests and wood products, 1987-1997: state-by-state estimates. IAG DW12938264-01-0, U.S. Forest Service.

Bliss, N.B., 2003. Soil organic carbon on lands of the Department of the Interior. USGS Open File Report 03-304.

Bliss, N.B., Waltman, S.W., Peterson, G.W., 1995. Preparing a soil carbon inventory for the United States using geographic information systems. In: Lal, R.,Kimble, J., Levine, E., Stewart, B. (Eds.), Soils and Global Change. CRC Press Inc, Boca Raton, FL, pp. 275-295.

Brejda, J.J., Moorman, T.B., Smith, J.L., Karlen, D.L., Allan, D.L., Dao, T.H., 2000. Distribution and variability of surface soil properties at a regional scale. Soil Science Society of America Journal 64 (3), 974-982.

Burke, I.C., Yonker, C.M., Parton, W.J., Cole, C.V., Flach, K., Schimel, D.S., 1989. Texture, climate, and cultivation effects on soil organic matter content in U.S. grassland soils. Journal of the Soil Science Society of America 53, 800-805.

Burrows, S.N., S.T. Gower, M.K. Clayton, D.S. Mackay, D.E. Ahl, J.M. Norman, and G. Diak, 2002. Application of geostatistics to characterize leaf area index (LAI) from flux tower to landscape scales using a cyclic sampling design, Ecosystems, 5 (7), 667-679.

Davidson, E.A., Lefebvre, P.A., 1993. Estimating regional carbon stocks and spatially

covarying edaphic factors using soil maps at three scales. Biogeochemistry 22, 107-131.

Davis KJ, Bakwin PS, Yi C, Berger BW, Zhao C, Teclaw RM, Isebrands JG. 2003. The annual cycles of CO_2 and H_2O exchange over a northern mixed forest as observed from a very tall tower. Global Change Biol 9(9):1278-1293.

EIIP, 2005. EIIP Document Series, Volume VIII: Estimating greenhouse gas emissions. Emission Inventory Improvement Program. Prepared by ICF Consulting for State and Local Climate Change Program. In: Program, U.S.E.P.A.E.I.I. (Ed.).

EPA, U.S., 2004. Inventory of U.S. greenhouse gas emissions and sinks: 1990 - 2002. In: Agency, U.S.E.P. (Ed.).

Franco, G., 2002. Inventory of California greenhouse gas emissions and sinks: 1990-1999. 600-02-001F, California Energy Commission, Sacramento, CA.

Goerg, K.C., Personal communication. NRCS National Resources Inventory data for Wisconsin.

Goodale, C.L., Apps, M.J., Birdsey, R.A., Field, C.B., Heath, L.S., Houghton, R.A., Jenkins, J.C., Kohlmaier, G.H., Kurz, W., Liu, S.R., Nabuurs, G.J., Nilsson, S., Shvidenko, A.Z., 2002. Forest carbon sinks in the northern hemisphere. Ecological Applications 12 (3), 891-899.

Heath, L.S., Birdsey, R.A., 1993. Carbon trend of productive temperate forests of the coterminous United States. Water, Air, and Soil Pollution 70, 279-293.

Heath, L.S., Birdsey, R.A., Williams, D.W., 2002. Methodology for estimating soil

carbon for the forest carbon budget model of the United States, 2001. Environmental Pollution 116, 373-380.

Heath, L.S., Kimble, J.M., Birdsey, R.A., Lal, R., 2003a. The potential of U.S. forest soils to sequester carbon. In: Kimble, J., Heath, L.S., Birdsey, R.A., Lal, R. (Eds.), The potential of U.S. forest soils to sequester carbon and mitigate the greenhouse effect. CRC Press Inc, Boca Raton, FL, pp. 385-394.

Heath, L.S., Smith, J.E., Birdsey, R.A., 2003b. Carbon trends in U.S. forestlands. In: Kimble, J., Heath, L.S., Birdsey, R.A., Lal, R. (Eds.), The potential of U.S. forest soils to sequester carbon and mitigate the greenhouse effect. CRC Press Inc, Boca Raton, FL, pp. 35-45.

Homann, P.S., Sollins, P., Fiorella, M., Thorson, T., Kern, J.S., 1998. Regional soil organic carbon storage estimates for western Oregon by multiple approaches. Soil Science Society of America Journal 62 (3), 789-796.

Johnson, M.G., Curtis, P.S., 2001. Effects of forest management on soil carbon and nitrogen storage: a meta-analysis. Forest Ecology and Management 140, 227-238.

Johnson, M.G., Kern, S.K., 2003. Quantifying the organic carbon held in forested soils of the United States and Puerto Rico. In: Kimble, J., Heath, L.S., Birdsey, R.A., Lal, R. (Eds.), The potential of U.S. forest soils to sequester carbon and mitigate the greenhouse effect. CRC Press Inc, Boca Raton, FL, pp. 47-71.

Kerr, S., 2004. Wisconsin's Greenhouse Gas Emissions: Trends from 1990 to 2000. PUB-AM-338 2004, Wisconsin Department of Natural Resources, Madison, Wisconsin.

Lacelle, B., Waltman, S.W., Bliss, N.B., Orozco-Chavez, F., 2001. Methods used to

create the North American soil organic digital database. In: Lal, R., Kimble, J., Follett, R., Stewart, B. (Eds.), Assessment methods for soil carbon. Lewis Publishers, Boca Raton, Florida, pp. 485-494.

Nelson, D.W., Sommers, L.E., 1982. Total carbon, organic carbon and orgainic matter. In: Page, A.L., Miller, R.H., Keeney, D.R. (Eds.), Methods of Soil Analysis. American Soc. of Agronomy, Wisconsin, USA, pp. 539-579.

Ney, R.A., Schnoor, J.L., Mancuso, M.A., 2002. A methodology to estimate carbon storage and flux in forestland using existing forest and soils databases. Environmental Monitoring and Assessment 78, 291-307.

NSSC, 1994. State Soil Geographic (STATSGO) data base, Data use information. In: USDA NRCS National Soil Survey Center, Lincoln, NE (Ed.).

Pacala, S.W., Hurtt, G.C., Baker, D., Peylin, P., Houghton, R.A., Birdsey, R.A., Heath, L., Sundquist, E.T., Stallard, R.F., Ciais, P., Moorcroft, P., Caspersen, J.P., Shevliakova, E., Moore, B., Kohlmaier, G., Holland, E., Gloor, M., Harmon, M.E., Fan, S.-M., Sarmiento, J.L., Goodale, C.L., Schimel, D., Field, C.B., 2001. Consistent land- and atmosphere-based U.S. carbon sink estimates. Science 292 (5525), 2316-2320.

Parton, W.J., Schimel, D.S., Cole, C.V., Ojima, D.S., 1987. Analysis of factors controlling soil organic-matter levels in great-plains grasslands. Soil Science Society of America Journal 51 (5), 1173-1179.

Parton, W.J., Scurlock, J.M.O., Ojima, D.S., Gilmanov, T.G., Scholes, R.J., Schimel, D.S., Kirchner, T., Menaut, J.C., Seastedt, T., Moya, E.G., Kamnalrut, A., Kinyamario, J.I., 1993. Observations and modeling of biomass and soil organic-

matter dynamics for the grassland biome worldwide. Global Biogeochemical Cycles 7 (4), 785-809.

Plantinga, A.J., Birdsey, R.A., 1993. Carbon fluxes resulting from United States private timberland management. Climatic Change 23 (1), 37-53.

Post, W.M., Emanuel, W.R., Zinke, P.J., Stangenberger, A.G., 1982. Soil carbon pools and world life zones. Nature 298, 156-159.

Ruffner, J.A., Blair, F.E. (Eds.), 1987. The weather almanac, 5th ed. Gale Res., Detroit, MI.

Schmidt, T.L., 1997. Wisconsin forest statistics, 1996. In: U.S. Dept. of Agriculture, F.S., North Central Forest Experiment Station (Ed.).

Turner, D.P., Koerper, G.J., Harmon, M.E., Lee, J.J., 1995. A carbon budget for forests of the conterminous united states. Ecological Applications 5 (2), 421-436.

WDNR, 1998. Land cover of Wisconsin: user's guide to WISCLAND land cover data. In: Wisconsin Department of Natural Resources, M.W. (Ed.).

Zhu, Z., Evans, D.L., 1994. U.S. forest types and predicted percent forest cover from AVHRR data. Photogrammetric Engineering and Remote Sensing 60 (5), 525-531.